UNDERSTANDING THE SOURCES AND ATMOSPHERIC PROCESSES OF SOLUBLE IRON IN AEROSOLS USING A SYNERGISTIC MEASUREMENT APPROACH

A Dissertation
Presented to
The Academic Faculty

By

Michelle M. Oakes

In Partial Fulfillment
Of the Requirements for the Degree
Doctorate of Philosophy
In Earth & Atmospheric Sciences

Georgia Institute of Technology

December 2011

UNDERSTANDING THE SOURCES AND ATMOSPHERIC PROCESSES OF SOLUBLE IRON IN AEROSOLS USING A SYNERGISTIC MEASUREMENT APPROACH

Approved by:

Dr. Rodney J. Weber, Advisor
School of Earth and Atmospheric Sciences
Georgia Institute of Technology

Dr. Ellery D. Ingall
School of Earth and Atmospheric Sciences
Georgia Institute of Technology

Dr. Amistead G. Russell
School of Civil and Environmental Engineering
Georgia Institute of Technology

Dr. Michael H. Bergin
School of Civil and Environmental Engineering
Georgia Institute of Technology

Dr. Martin M. Shafer
Department of Environmental Chemistry and Technology
University of Wisconsin-Madison

Date Approved: October 25, 2011

ACKNOWLEDGEMENTS

During my time at Georgia Tech, I was privileged to work alongside several experts inside and outside of my field. I am fortunate to have worked under the instruction of my thesis advisor Dr. Rodney Weber, who supported me not only on the research presented in this thesis, but also on career goals and life in general. I appreciate the time and effort he expended while mentoring me from a junior scientist to an independent researcher. I am also extremely grateful to have collaborated closely with Dr. Ellery Ingall on research using synchrotron-based measurements. By combining his expertise in synchrotron-based measurements and my knowledge on aerosol science and measurements, we were able to answer several questions regarding controls on iron solubility addressed in this thesis. I would also like to thank my committee members, Dr-s. Martin M. Shafer, Armistead Russell, and Michael Bergin for taking the time to review my thesis and provide valuable input on the scientific content. I truly have learned several valuable lessons that facilitated my growth as a scientist by working alongside these experts. I hope I am lucky enough to work with such interesting and resourceful individuals in my future career.

I would also like to thank my current and past group members, Xiaolu Zhang, Jiumeng Liu, Laura King, Eric Parker, Neel Kotra, Dr. Vishal Verma, Dr. Arsineh Hecobian, Dr. Chris Hennigan, Dr. Rick Peltier, and Dr. Neeraj Rastogi, for their participation in fruitful conversations on research and life as well as their laboratory and field support. Without their help, research would have been more difficult. In addition, I am grateful for my fellow students in the Earth and

Atmospheric Sciences and Environmental Engineering department. These people have made my experience at Georgia Tech memorable.

I would also like to thank my family and friends. My mom, dad, and sister have been my guiding light throughout my life. I continue to learn how to be a better person and scientist from them every day. Last, I would like to thank the love of my life, my husband Tyler Jones. No words can ever express my appreciation for the unconditional support, patience, and kindness he has provided me through this experience. His optimism on my research and career goals is such an inspiration to me. I hope one day I can return the favor.

TABLE OF CONTENTS

LIST OF TABLES

LIST OF FIGURES

LIST OF ABBREVIATIONS

Ca: Calcium ion

CCN: Cloud Condensation Nuclei

CF-PILS-LWCC: Continuous-flow integrated system with a PILS and LWCC

DI: De-ionized Water

EC: Elemental Carbon

EXAFS: Extended X-ray Absorption Fine Structure

Fe(II): Ferrous Iron, Reduced Iron

Fe(III): Ferric Iron, Oxidized Iron

HCl: Hydrochloric acid

HNO_3: Nitric acid

K^+: Potassium ion

LST: Local Standard Time

LWCC: Liquid Waveguide Capillary Cell

Na^+: Sodium ion

NH_4^+: Ammonium Ion

NO_3^-: Nitrate ion

OC: Organic carbon

PILS-LWCC: Coupled online PILS and LWCC system

ROS: Reactive Oxygen Species

SO_2: Sulfur dioxide gas

SO_4^{2-}: Sulfate ion

TEOM: Tapered Element Oscillating Micro-balance

UV/Vis: Ultraviolet/Visible

WS_Fe(II): Water-soluble Ferrous Iron

WS_Fe: Total water soluble iron (Fe(II) + Fe(III))

WS_K: Water-soluble Potassium

XANES: X-ray Absorption Near-Edge Structure

SUMMARY

The theme of this thesis is the characterization of soluble iron in atmospheric aerosols through the use of online and offline measurements. Using this synergistic measurement approach, a comprehensive perspective of chemical and physical properties of soluble iron aerosols was acquired. This unique dataset provided valuable insight into the major sources and atmospheric processes contributing to the presence of soluble iron aerosols in the atmosphere.

As a part of this thesis, a new measurement method was developed resulting in the first semi-continuous measurements of water-soluble ferrous iron (WS_Fe(II)) in aerosols. The prototype consisted of an online particle collection device (Particle-Into-Liquid-Sampler (PILS)) [*Orsini et al.*, 2003], coupled to a liquid waveguide capillary cell (LWCC) and a portable spectrophotometer for WS_Fe(II) detection by the ferrozine technique [*Stookey*, 1970]. The combined method, known as the PILS-LWCC, yielded highly time-resolved WS_Fe(II) measurements in atmospheric aerosols (12-minute measurement), with a method limit of detection of 4.6 ng m^{-3} and a measurement uncertainty of 12%. To evaluate the performance of the new technique, a filter sampler was operated alongside the PILS-LWCC during several field studies, allowing for direct comparison of online (PILS-LWCC) and offline (filter-based) techniques. A relatively good comparison was observed between online and offline WS_Fe(II) measurements (r2=0.71, slope: 0.84 ± 0.1), proving the PILS-LWCC a resourceful, and reliable technique for field aerosol measurement. Overall, the PILS-LWCC provided a novel measurement method that

significantly improved time-resolution of WS_Fe(II) in aerosols from conventional techniques.

Following instrument development, the PILS-LWCC was deployed at two urban sites (Dearborn, MI and Atlanta, GA) with contrasting emissions during different seasons, and at a rural site (Southeastern US) during a biomass burning event to characterize WS_Fe(II) sources and temporal variability. During field deployment, no clear diurnal trends in WS_Fe(II) were observed at any urban site studied. The lack of a day-time increase in WS_Fe(II), suggested that photo-reductive processes only play a minor role in WS_Fe(II) variability. High temporal variability, however, was observed at all urban sites, where concentrations often changed from the method limit of detection (4.6 ng m^{-3}) to approximately 300 to 400 ng m^{-3}, lasting only a few hours (e.g. WS_Fe(II) transient events). Several transient events observed in Atlanta, GA and Dearborn, MI predominately occurred during times of low wind speeds and appeared to be from local industrial sources or processes. Other transient events observed exclusively in Atlanta were associated with sulfate plumes. The highest WS_Fe(II) concentrations in these event plumes corresponded to apparent aerosol acidity (based on the concentrations of major inorganic ions). At all locations studied, WS_Fe(II) was poorly correlated ($r^2 < 0.34$) with light-absorbing aerosol, indicating no direct linkage between mobile source emissions and enhanced WS_Fe(II) concentrations. WS_Fe(II) measured within a prescribed forest-burn was strongly correlated with water-soluble potassium ($r^2=0.88$; WS_Fe(II)/WS_K = 15 mg/g), pointing to biomass burning as a source of WS_Fe(II). Overall, temporal trends at these sites

pointed to several important sources and formation mechanisms of WS_Fe(II) including: 1) unique industrial emissions, 2) acid-processing mechanisms, and 3) biomass burning.

To understand how other physical and chemical properties affect iron solubility in ambient aerosols, advanced synchrotron-based methods were used, specifically X-ray Absorption Near Edge Structure (XANES) spectroscopy and micro X-ray fluorescence techniques. These techniques are capable of determining detailed chemical speciation (e.g. oxidation state and chemical composition) and mixing state (e.g. elemental associations) in single particles. The first synchrotron study focused on detailed characterization of chemical speciation in fine iron-containing particles deposited on a variety of ambient urban (Atlanta, GA) and rural (Fort Yargo, GA) Teflon filter samples. This unique data was used in conjunction with iron solubility measurements (soluble iron/total iron) to evaluate the importance of speciation as a control factor of iron solubility. XANES measurements indicated that iron in single particles was present as a mixture of Fe(II) and Fe(III), with Fe(II) content generally between 5 and 35% (mean: ~25%). XANES and micro-X-ray fluorescence analysis indicated that a majority (74%) of Fe particles are best characterized as Al-substituted Fe-oxides, with a Fe/Al molar ratio of 4.9. The next most abundant group of particles (12%) was Fe-aluminosilicates, with Si/Al molar ratio of 1.4. No correlation was found between iron solubility (soluble iron/total iron) and the abundance of Al-substituted Fe-oxides and Fe-aluminosilicates present in single particles or solid-phase Fe(II)

content, suggesting solubility largely depended on factors other than differences in iron speciation.

Similar analyses were performed on single iron-containing particles from source emission fine particles (e.g. biomass burning, coal fly ash, mineral dust, and mobile) to continue investigating the relationship between speciation and iron solubility. Major differences were observed in iron solubility in source emission particles, ranging from very low solubility (<1%, mineral dust, coal fly ash) to 75% (diesel exhaust, gasoline exhaust, biomass burning smoke). Similar to the findings in ambient aerosols, differences in iron solubility did not correspond to changes in oxidation state and/or the abundance of major iron phases (iron oxides vs. iron silicates) based on XANES and micro X-ray fluorescence single particle analysis. Single particle sulfur content, however, corresponded to iron solubility. Similar trends between single particle sulfur content and soluble iron were also observed in a winter and summer sample collected in Atlanta, GA (South Dekalb site). A strong correspondence between bulk iron solubility and sulfate measurements (e.g. decreasing trend between bulk iron solubility and Fe/SO_4^{2-}) observed in archived filter measurements from a year-long study (N of filters=358) in Atlanta, GA further supported this trend. These results strongly suggest that sulfur (as sulfate) associated with iron-containing particles promotes iron solubility. This soluble iron-sulfur relationship is likely due to acid-processing mechanisms by H_2SO_4 that is potentially related to the formation of very soluble iron sulfates.

Overall, the combined results of this thesis show unique findings that suggest iron solubility is primarily driven by aerosol sulfate concentrations, likely

through acid-processing mechanisms involving secondary sulfuric acid. Though other aerosol properties (chemical phase and Fe(II) content) and atmospheric processes (photoreductive mechanisms) may influence iron solubility, their role appears to be negligible. The results of this thesis have significantly contributed to the current state of knowledge regarding soluble iron, which will ultimately help to evaluate it's impact on human health and the environment.

CHAPTER 1

INTRODUCTION

1. 1 Importance of Atmospheric Aerosols

Atmospheric aerosols are solid or liquid particles that are pervasive in the atmosphere. They are primarily emitted by natural (biogenic) and anthropogenic sources or formed in the atmosphere through various processes. After emission or formation, they can remain in the atmosphere up to several weeks, potentially traveling long distances before deposition occurs. During long range-transportation, they may interact with other atmospheric constituents through condensation/evaporation, coagulation, or chemical mechanisms that significantly alter their original chemical and physical state. Their presence in the atmosphere has important implications on climate change and human welfare.

1.1.1 Climate Change

The most significant uncertainty in predicting future climate change is the interaction between solar radiation and atmospheric aerosols [*IPCC*, 2007]. In the direct effect, aerosols scatter or absorb solar radiation depending on size and chemical composition, effectively altering the Earth's radiative budget. Though the direct effect impacts regions differently, it is expected to cool the climate on a global scale, having an overall impact on radiative forcing [*IPCC,* 2007]. Aerosols may also impact climate indirectly by influencing cloud microphysical properties as critical seeds for cloud formation (cloud condensation nuclei CCN), known as the indirect effect [*Charlson et al.*, 1992]. Through effects on cloud lifetime/albedo and the

hydrological cycle, the aerosol indirect effect is generally hypothesized to cool the climate. However, the extent to which it cools the climate is highly uncertain [*IPCC,* 2007]. The current state of knowledge regarding the aerosol direct and indirect effects on climate is poorly constrained by a limited understanding of aerosol optical and CCN properties as well as emission inventories.

1.1.2 Health Impacts

In addition to climate impacts, aerosols adversely impact human health. Exposure to atmospheric aerosols by inhalation has been linked to a number of negative health outcomes, ranging from decreased lung function to pre-mature morbidity [*Dockery et al.*, 1993; *Pope*, 2000; *Pope et al.*, 2002]. Previous studies have shown that aerosol size (e.g. PM2.5 vs. PM10) [*Dockery et al.,* 1993*; Samet et al.,* 2000] and chemical composition are key factors associated with negative outcomes. More recent toxicological studies have demonstrated that cellular oxidative stress, a condition triggered by toxic levels of reactive oxygen species (ROS, e.g.), is the main mechanism driving adverse health outcomes associated with aerosols [*Ayres et al.,* 2008*; Tao et al.,* 2003]. These studies argue that ROS or catalysts for ROS formation are the most toxic aerosol species. Though several aerosol properties and components are hypothesized to influence human health, the exact underlying mechanisms associated with aerosol toxicity are still poorly understood, motivating continued research on this subject.

1.2 Iron in Atmospheric Aerosols

Atmospheric aerosols are generally comprised of organic carbon, elemental carbon, sulfate, nitrate, ammonium, and trace metals. In general, trace metals

constitute a small fraction of atmospheric aerosols on a mass basis; however, their impact on human health and climate change is evident. For instance, adverse health effects related to oxidative stress stem from high levels of ROS that form as a consequence of the redox cycling of trace metals [*Kelly*, 2003; *Vidrio et al.*, 2008]. In addition, trace metals are often critical catalysts for nutrient uptake in marine biological species, which in turn, impact global climate change [*Martin et al.*, 1994].

Iron is an abundant trace metal in atmospheric aerosols. In comparison to other trace metals, iron has a pronounced effect on both human health and global climate change. Due to it's high redox activity and abundance in the atmosphere, iron has often been observed as the most significant source of ROS via metal-mediated pathways in aerosols, thus, is strongly linked to health-related impacts caused by oxidative stress [*Shafer et al.,* 2010*; Smith and Aust,* 1997*; Zhang et. al.*, 2008]. Iron also plays an important role in the global carbon cycle through effects on marine productivity [*Martin et al.*, 1994]. As a critical micronutrient for phytoplankton productivity, iron indirectly affects sequestration of carbon species to the deep ocean by phytoplankton, which is considered a significant sink for atmospheric carbon (CO_2). Deposition of aerosol iron from crustal and anthropogenic sources is thought to be a major source of soluble (bio-available) iron to marine regions far from alternative sources of iron (e.g. rivers, hydrothermal vents, etc.) [*Gao et al.*, 2003; *Jickells et al.*, 2005; *Lam and Bishop*, 2008].

The role of iron in both human health and biogeochemical cycles largely depends on the fraction that is readily soluble in water [*Costa and Dreher*, 1997; *Dreher et al.*, 1997; *Prahalad et al.*, 2001; *See et al.*, 2007; *Valavanidas et al.*, 2008;

Wells et al., 1995]. Of the total iron in ambient aerosols, the soluble fraction is often thought to be a small fraction. However, this is in contrast to several field observations showing that iron solubility (soluble iron/total iron) is significantly variable and can comprise a large portion of total iron (0.01-80%) [*Chen and Siefert*, 2004; *Johansen et al.*, 2000; *Mahowald et al.*, 2005; *Zhu et al.*, 1993; *Zhuang et al.*, 1992]. While several chemical particle properties and atmospheric processes have been shown to influence iron solubility, there is still significant uncertainty on the primary factors that control solubility [*Baker and Croot*, 2010and references within]. Identifying major sources, aerosol properties, and atmospheric processes promoting iron solubility in aerosols is essential to accurately assessing it's impact on human health and global climate change.

1.3 Factors Influencing Iron Solubility

There are many natural and anthropogenic sources of soluble (bio-available) iron in aerosols. While crustal material is thought to be a significant source of iron, it is predominately comprised of insoluble iron oxide and silicate (clay) minerals, containing less than 3% soluble iron content on average [*Claquin et al.*, 1999]. More recent studies have recognized the importance of natural and anthropogenic combustion sources to soluble iron in atmospheric aerosols [*Chuang et al.*, 2005; *Guieu et al.*, 2005; *Luo et al.*, 2008]. In several marine regions, these combustion sources may be the predominant source of soluble iron [*Luo et. al.,* 2008]. Mechanical wear from industrial and vehicular operations [*Choel et. al.*, 2007; *Majestic et al.*, 2009; *Choel et. al.*, 2010] is also a known source of iron. However, the soluble iron portion is widely variable and dependent on emission conditions and

source material composition. Though it is widely accepted that iron solubility significantly varies among sources, much less is known about the particle properties and mechanisms driving these differences.

Aerosol chemical properties, such as speciation (chemical composition and oxidation state), have been shown to play a critical role in iron solubility [*Cwiertny et al.*, 2008; *Journet et al.*, 2008; *Schroth et al.*, 2009]. While iron oxides in crustal material, such as goethite and hematite, have relatively high amounts of total iron compared to clay minerals, they generally contain less soluble iron content [*Journet et al.*, 2008]. This study attributed these solubility differences among these minerals to their structural properties (crystalline vs. ionic structure). Furthermore, iron sulfates observed in anthropogenic combustion material are much more soluble than both iron oxides and iron-containing clay minerals [*Schroth et al.*, 2009]. Other studies have shown that Fe(II)-containing solid phases in various crustal material may significantly contribute to iron solubility in acidic aerosol conditions [*Cwiertny et. al., 2008*].

In addition to mineralogy, iron aerosols can experience a series of atmospheric processes during long-range transportation, which may ultimately increase it's solubility. Photo-reduction of organically-complexed Fe(III) has been hypothesized to enhance iron solubility in cloud and fog water, by forming more soluble Fe(II) [*Erel et al.*, 1993; *Faust and Zepp*, 1993; *Pehkonen et al.*, 1993; *Siefert et al.*, 1994]. While some studies have demonstrated compelling evidence for enhanced iron solubility due to photo-reductive mechanisms [*Siefert et al.*, 1994; *Willey et al.*, 2005], others have observed no such evidence [*Parazols et al.*, 2006].

Physical sorting of iron-containing atmospheric aerosols has also been hypothesized as an alternative process promoting iron solubility [*Baker and Jickells*, 2006; *Ooki et al.*, 2009]. In this hypothesis, deposition of coarse particles by gravitational settling occurs shortly after atmospheric emission, sorting out coarse particles from fine particles during long-range transportation. The fine particles left behind have relatively large surface areas allowing for significant interaction between surface iron and the deliquescent layer, which in turn, affect iron solubility. However, a recent combined laboratory and modeling study suggested that this mechanism may not be an important factor to iron solubility in dust samples [*Shi et. al.*, 2011].

Another mechanism promoting iron solubility is the acidification of iron aerosols by secondary acids in urban pollution, known as acid-processing [*Duce and Tindale*, 1991; *Meskhidze et al.*, 2003; *Solmon et al.*, 2009]. During this process, secondary acidic species (H_2SO_4,HNO_3, and HCl) condense onto the surface of an insoluble iron aerosol, subsequently decreasing aerosol pH in the absence of sufficient neutralizing cations. In acidic media, the dissolution of all iron species is thermodynamically favored, thus, resulting in enhanced soluble iron content. Modeling studies and laboratory studies have demonstrated that acid-processing is a viable explanation for the dissolution of iron species in crustal material during typical long-range atmospheric transportation [*Hand et al.*, 2004; *Mackie et al.*, 2005; *Meskhidze et al.*, 2003; *Shi et. al.,* 2011]. Furthermore, recent laboratory and field studies suggested that acid-processing (pH cycling during in-cloud processing) could be linked to the formation of extremely soluble iron particles, resulting in an overall increase iron solubility [*Shi et al.*, 2009; *Takahashi et al.*, 2011].

Decades of research on iron solubility have clearly established a fundamental background on the potential sources and atmospheric formation processes of soluble iron in aerosols. However, significant inconsistencies exist among field, laboratory and modeling data, indicating the need for continued research. A comprehensive dataset of unique aerosol properties in conjunction with bulk iron solubility could reduce these measurement inconsistencies. This can be achieved by using a synergistic measurement approach that employs unique analytical methods.

1.4 Need for Highly Time-Resolved Soluble Iron Measurements

Traditionally, atmospheric concentrations of soluble iron have been measured by filtration techniques, where ambient aerosols are collected on filters over extended periods of time and then extracted into aqueous solution for subsequent analyses. The relatively long sample integration periods inherent with this method, typically 12 to 24 hours, inhibit investigating variability in WS_Fe(II) concentrations over shorter timescales. Sample alteration during collection and analysis is also a potential drawback of filter-based methods. Inter-conversions of Fe(II)/Fe(III) on the filter during sample collection, sample storage or the extraction process prior to analysis, may result in measurement biases [*Majestic et al.*, 2006]. More highly time-resolved measurements, from an online instrument set-up, have been shown to provide new insights into Fe sources by having the capability to explore acute transient events that may have a pronounced effect on human health [*Kidwell and Ondov*, 2004].

1.5 Need for Iron Speciation Measurements

Though there are countless benefits associated with online instrumentation, they are not always capable of providing detailed information on unique aerosol properties, such as iron speciation and particle mixing state (e.g. elemental associations). These two properties can provide key insight to sources and atmospheric processes of soluble iron. Relatively few analytical tools are currently available to provide such detailed characterization of iron, which are described in detail by *Majestic et. al.* [2007]. Typically, studies of aerosols rely upon chemical extractions or spectroscopic techniques that provide speciation information on bulk properties of iron in a sample. Spectrophotometry (e.g. ferrozine) and high performance liquid chromatography (HPLC) have been used to quantify Fe(II) and Fe(III) in bulk aerosol samples, but yield little information on molecular composition [*Johansen et al.*, 2000; *Zhuang et al.*, 1992]. Mossbauer spectroscopy has been successfully used to directly characterize the oxidation state and chemical composition in aerosol samples [*Hoffmann et al.*, 1996]; however, collection of aerosol over a several month period is required to obtain sufficient mass for analysis (~1 g). Recent innovations in synchrotron-based X-ray absorption spectroscopy, specifically X-ray Absorption Near Edge Structure (XANES) and microscopic X-ray fluorescence, have made it possible to explore oxidation state, chemical composition, and mixing state of single particles. These methods require minimal sample preparation and are capable of single particle analysis. XANES and EXAFS have been widely used to probe iron speciation in soil samples [*Marcus et al.*,

2008; *Prietzel et al.*, 2007]. Werner et. al. [2007] recently extended EXAFS to atmospheric aerosols to identify oxidation state and mineralogy of chromium in urban California. A few studies have demonstrated the feasibility and benefits of synchrotron-based X-ray spectroscopic techniques using a low energy X-ray beam for the analysis of iron in aerosol samples, but primarily focused on oxidation state characterization [*Majestic et al.*, 2007; *Takahama et al.*, 2008].

In this dissertation, a recently developed online technique (PILS-LWCC) and synchrotron-based offline techniques were used to understand iron solubility in aerosols. Several pertinent research questions involving sources and atmospheric processes contributing to iron solubility in atmospheric aerosols were addressed. These topics include:

- Temporal and seasonal variability of soluble iron aerosols
- Iron speciation in ambient and source particles and particle mixing in urban aerosols and source emission aerosols
- Major sources and atmospheric processes of soluble iron in urban and rural regions

CHAPTER 2

DEVELOPMENT OF A SEMI-CONTINUOUS METHOD TO MEASURE WATER-SOLUBLE FERROUS IRON IN ATMOSPHERIC AEROSOLS

This chapter describes the development of a semi-continuous method to measure water-soluble ferrous iron (WS_Fe(II)) in atmospheric aerosols by coupling a Particle-into-Liquid Sampler (PILS), Liquid Waveguide Capillary Cell (LWCC) and a portable spectrophotometer (PILS-LWCC). Measurements from this method were used to characterize and identify sources of WS_Fe(II) in urban and rural aerosols and are referred to in a significant portion of this dissertation

2.1. Particle into Liquid Sampler (PILS)

The Particle-into-Liquid Sampler (PILS) was used for particle collection in this method. Essentially, it is a device used to collect aerosols into de-ionized water for chemical analysis Figure 2.1 presents a schematic of the PILS. In this device, ambient air is pulled through a cyclone (URG, Chapell Hill, North Carolina), selecting for particles with aerodynamic diameters less than 2.5 μm, and then into the PILS chamber via vacuum pump at a flow rate of 16.7 l min^{-1}. Upon entering the PILS, ambient air is mixed with a turbulent flow of steam (1.6 ml min^{-1}, 100 °C), causing rapid cooling of the steam and creating a supersaturated environment. In this supersaturated environment, water vapor condenses onto particles ranging from 0.03 to 10 μm, growing the particles to a size large enough to be collected by impaction. These condensed particles are subsequently collected onto a quartz impaction plate and transferred from the plate to a continuous flow of de-ionized water (>18.0 MΩ), thus, creating a continuous sample of ambient aerosol. The

ambient aerosol concentration in aqueous solution can be calculated from Equation 2.1, where C_A is the ambient aerosol concentration (ng m^{-3}), C_L is the aqueous solution concentration (µg L^{-1}), F_L is the liquid flow rate (mL min^{-1}), and F_A is the air flow rate (L min^{-1}).

$$C_A = \frac{1000 C_L F_L}{F_A}$$

Equation 2.1. Equation used to calculate WS_Fe(II) in ambient air

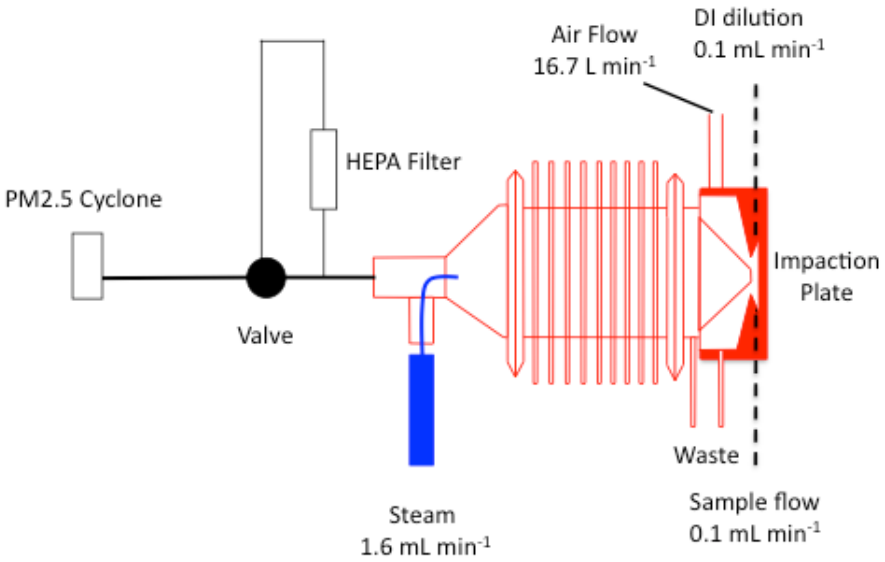

Figure 2.1. Schematic of Particle-Into-Liquid Sampler (PILS), modified from Orisini et. al. (2003).

2.2 WS_Fe(II) Detection: Spectrophotometry and Liquid Waveguide Capillary Cell

To effectively develop a semi-continuous system for detection of water-soluble ferrous iron (WS_Fe(II)) in aerosols, a robust method capable of detecting metals at trace levels must be employed. Spectrophotometric methods have widely been used to quantify water-soluble trace metals. Using this technique, specific organic ligands with high absorptivities interact with water-soluble trace metals, forming colored complexes that can be detected by a spectrophotometer. The amount of light absorbed by the colored complex is linearly proportional to the trace metal concentration in solution. Stookey et. al. [1970] developed a spectrophotometric technique specific for WS_Fe(II) analysis based on maximum light absorption of WS_Fe(II) complexed to the ferrozine ligand (3-(2-pyridyl)-5,6-diphenyl-1,2,4-triazine-4-4'-disufonic acid) at 562 nm [*Zhang et. al.*, 2001]. This technique has been successfully used to detect WS_Fe(II) in a variety of environments.

While detection of WS_Fe(II) at trace levels is possible using conventional instrumentation employed with standard sample cell (e.g. cuvette, ~1cm light path length), these levels are much higher than the WS_Fe(II) concentration range expected in the atmosphere, indicating the need to improve measurement sensitivity. One relatively inexpensive way to improve sensitivity is to increase the path length of the sample cell. Recent advances in optical flow-through capillary cells (e.g. liquid waveguide capillary cells) have made it possible to considerably increase the path length of standard spectrophotometry sample cells. These cells

house sample tubing coated with a material having a refractive index lower than water. This property allows incoming light to be restricted to the liquid sample while being reflected throughout the sample cell. Therefore, the light absorbed or transmitted by the sample can be transferred through the cell, and subsequently to the detector using fiber optic cables. These optical flow-through cells are manufactured with light-path lengths up to hundreds of centimeters, resulting in drastic improvements on the sensitivity of traditional spectrophotometric techniques.

In this study, a 100cm liquid waveguide capillary cell with an internal sample volume of 250 μl (World Precision Instruments, Sarasota, FL) was used to provide sufficient sensitivity for WS_Fe(II) aerosol measurements. A fiber optic cable was used to direct UV/VIS light from the dual deuterium, tungsten halogen light source (DT-Mini2, World Precision Instruments, Sarasota, FL) to the LWCC. A second fiber optic cable was used to direct the light reflected or absorbed by the sample to a portable spectrophotometer (USB4000 Spectrophotometer) for absorbance measurements. Figure 2.2 shows a schematic of the LWCC connected to the light and portable spectrophotometer.

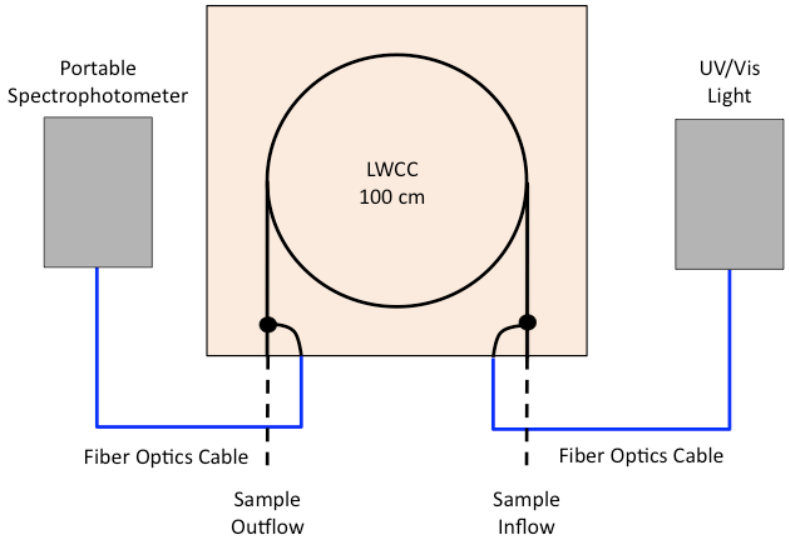

Figure 2.2. Schematic of a 100 cm Liquid Waveguide Capillary Cell (LWCC) coupled to an UV/Vis light source and portable spectrophotometer.

2.3 Coupling the PILS to LWCC and Portable Spectrophotometer: PILS-LWCC

The PILS has been coupled to a number of analytical instruments, such as an ion chromatograph and total organic carbon analyzer, to measure major atmospheric components [*Orsini et. al.,* 2003, *Sullivan et. al.*, 2006]. However, to adapt the liquid system to measure WS_Fe(II) in the aerosols, detectors were replaced and significant measures were taken to minimize sample dilution.

The integrated system, referred to as PILS-LWCC, was developed and modified from a flow-through measurement system, built by *Zhang et. al.* [2001] for WS_Fe measurements in seawater. The measurement system by *Zhang et. al.* [2001] was characterized by a gas-segmented continuous sample flow of 1 ml min^{-1} through the sample cell, a flow rate selected for optimal operation of the LWCC with

a gas-segmented sample (e.g. to minimize air bubble interferences and maximize sensitivity). Consequently, this high sample flow rate could not be used in the PILS-LWCC without significantly diluting the aerosol sample. For this reason, a batch analysis system, using a collection vial, was used in this study instead of a continuous flow through system. A schematic of the coupled PILS-LWCC system is shown in figure 2.3. In this system, two mutli-channel peristaltic pumps equipped with Tygon tubing controlled the liquid flows the PILS-LWCC: one for PILS operation and the second one for the liquid handling system to the spectrophotometer (outlined in green in figure 2.3). A polypropylene 2-position valve was used to direct either water or aerosol sample (from the collection vial) to the liquid handling system for spectrophotometric analysis of the background or WS_Fe(II) sample measurement, respectively.

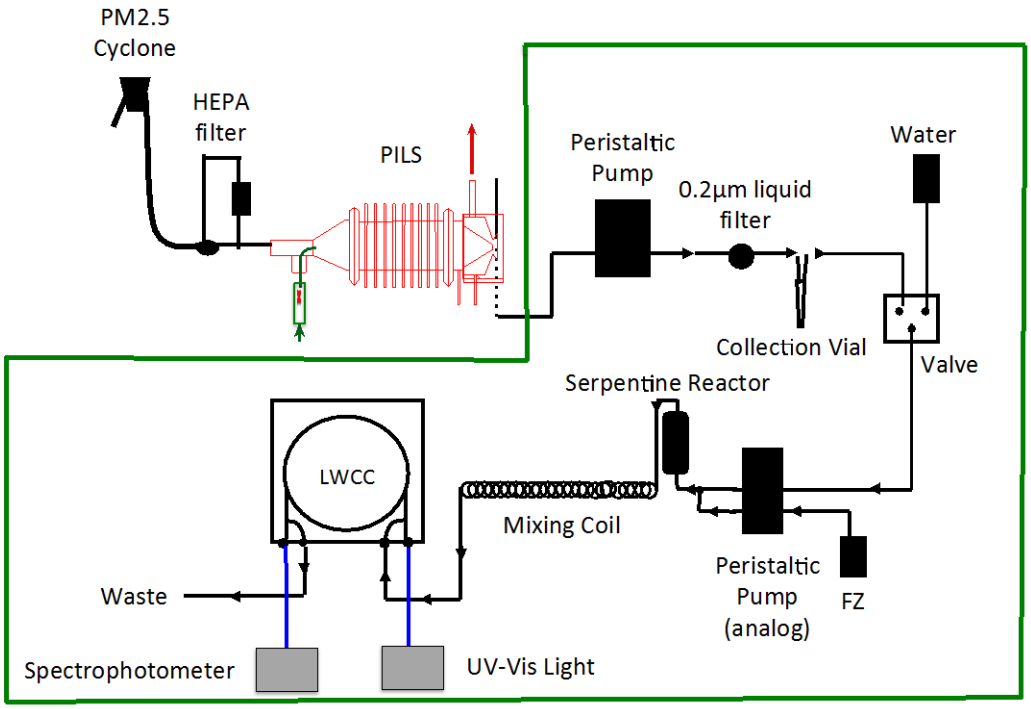

Figure 2.3. Schematic of the PILS-LWCC semi-continuous coupled system. The liquid handling portion of the coupled system is outlined in green.

The PILS-LWCC was designed to make a 12-minute semi-continuous measurement of WS_Fe(II) in aerosols. As previously described in detail in section 2.1, a continuous sample flow was supplied to the liquid handling system (outlined in green) from the PILS. From the PILS, the aerosol sample flow (0.1 mL min^{-1}) was pumped through a polypropylene syringe filter (removing insoluble particles with a diameter greater than 0.22 µm) and directed to a 15-ml polypropylene collection vial. After 12 minutes of sample accumulation (~1.2 ml), the 2-position valve was switched to the sample, and a second peristaltic pump, controlled by a computer program (DaqFactory) emptied the vial at a flow rate 0.12 mL min^{-1}. The flow rate

used to empty the sample from the vial was 0.2 mL min^{-1} faster than the sample flow rate into the vial to ensure complete removal of the sample and to separate the sample from subsequent background measurements with a large air bubble. After 2 minutes of emptying the collection vial, the 2-position valve was switched back to the DI water supply, pumping water through the liquid handling system downstream of the sample. The sample was subsequently guided to a sample tee and combined with 5 mM ferrozine at a flow rate of 0.01 mL min^{-1}, yielding a 1:10 ratio of ferrozine to aerosol sample. This mixed sample (sample + ferrozine) was then directed to a Teflon super-serpentine reactor (Global FIA, Fox Island, Washington) and a series of handmade mixing coils (100-turns) constructed of PEEK tubing (o.d: 1/16 in, i.d.: 0.030 in, Upchurch Scientific, Oak Harbour, Washington) to enhance mixing of ferrozine solution and WS_Fe(II) in the sample. Before the sample was pumped into the LWCC for analysis, the flow was halted for 4 minutes, allowing for additional reaction time for WS_Fe(II) in the sample to complex with ferrozine. After this reaction time, the mixed sample was pumped into the LWCC and light absorbance measurements were recorded at 562nm and 700nm. WS_Fe(II) was quantified by the light absorbed at 562 nm (maximum light absorbance of WS_Fe(II)-ferrozine complex) normalized to 700 nm (measurement baseline). After WS_Fe(II) measurements were completed, a large air bubble was pumped through the LWCC, removing any micro-bubbles on the LWCC walls, followed by a background measurement (DI + ferrozine). This integrated PILS-LWCC method resulted in a 12-minute semi-continuous measurement of WS_Fe(II) in aerosol samples.

2.4 Reagents and Standards

To maintain trace-metal clean conditions, reagents and standards used for PILS-LWCC calibration and operation were prepared in acid-cleaned amber or clear polyethylene bottles. An acidified (pH 1 by HCl) 1000 mg Fe(II) L^{-1} stock solution was prepared by adding 0.702g ammonium iron(II) sulfate hexahydrate (Sigma-Aldrich, St. Louis, MO) to 10g of ultra-pure water (>18MΩ) gravimetrically. Working Fe(II) standards ranging from 1 to 20 μg L^{-1} for instrument calibration were prepared by serial dilution of 1000 mg Fe(II) L^{-1} stock solution by 40 ml of ultrapure water and were acidified (pH 2 by HCl). Although a 10 mM ferrozine solution was used in other continuous flow-through configurations [*Zhang et. al.*, 2001], a 5 mM solution was sufficient for the reaction conditions in the PILS-LWCC. This two-fold dilution of ferrozine solution significantly reduced the amount of ferrozine ligand consumed in the online system. This solution was prepared by adding 0.255 g of ferrozine (3-(2-pyridyl)-5,6-diphenyl-1,2,4-triazine-4-4'-disufonic acid, Sigma-Aldrich, St. Louis, MO) to 100ml of ultra-pure water. A Brij-35 surfactant was added in a 1:100 ratio to the ferrozine reagent to minimize large backpressures caused by air bubbles entering the system, causing substantial background noise [*Zhang et al*., 2001]. All stock solutions and reagents were stored in a dark refrigerator (4°C).

2.5 System Performance

2.5.1 Calibration Curve

The PILS-LWCC was calibrated using WS_Fe(II) working standards ranging from 1 to 20 μg L^{-1}. To calibrate the PILS-LWCC, WS_Fe(II) standards were pumped

through the liquid handling system and analyzed by the spectrophotometer in a similar fashion as ambient samples during typical PILS-LWCC operation. Figure 2.4 represents a typical calibration curve of the PILS-LWCC method, with a slope of 0.045 ± 0.0003 and r2=0.9995. During the course of instrument development and validation, the stability of the calibration curve was investigated by quantifying the variability of the slope taken during different sampling periods (shown in Table 2.1). The slope varied from 0.0423 and 0.0462, with a mean value of 0.0448, N=6.

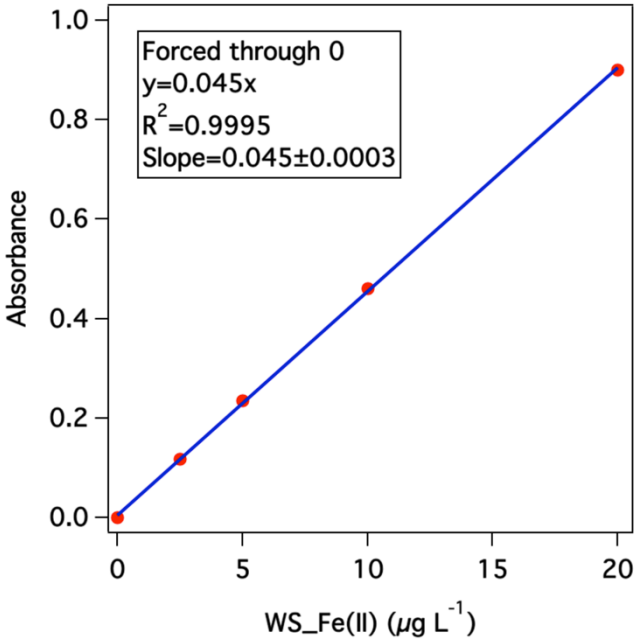

Figure 2.4 PILS-LWCC liquid handling system calibration. Linear regression results are presented. The y-intercept was forced through 0.

Table 2.1. Linear regressions results of the PILS-LWCC calibration curve taken during different days in a variety of field studies

Day	*Slope (a.u/ug L-1)*	*Y-intercept*	*r2*
1*	0.045 ± 0.0003	N/A	0.9995
2	0.0446 ± 0.0003	0.0097 ± 0.0038	0.9999
3	0.0459 ± 0.0007	0.0125 ± 0.0049	0.9997
4	0.0423 ± 0.0010	0.0590 ± 0.00268	0.9994
5	0.0449 ± 0.0007	0.0050 ± 0.0098	0.9997
6	0.0462 ± 0.0005	0.0005 ± 0.0062	0.9997

*Linear regression shown in Figure 2.X: y-intercept forced through 0

The uncertainty associated with the liquid handling system was <3% and was ultimately determined by the variability of absorbance measurements of a low WS_Fe(II) concentration standard (1 μg L^{-1}) analyzed 11 consecutive times. Figure 2.5 shows the absorbance measurements of these consecutive analytical runs, demonstrating the high stability of this method.

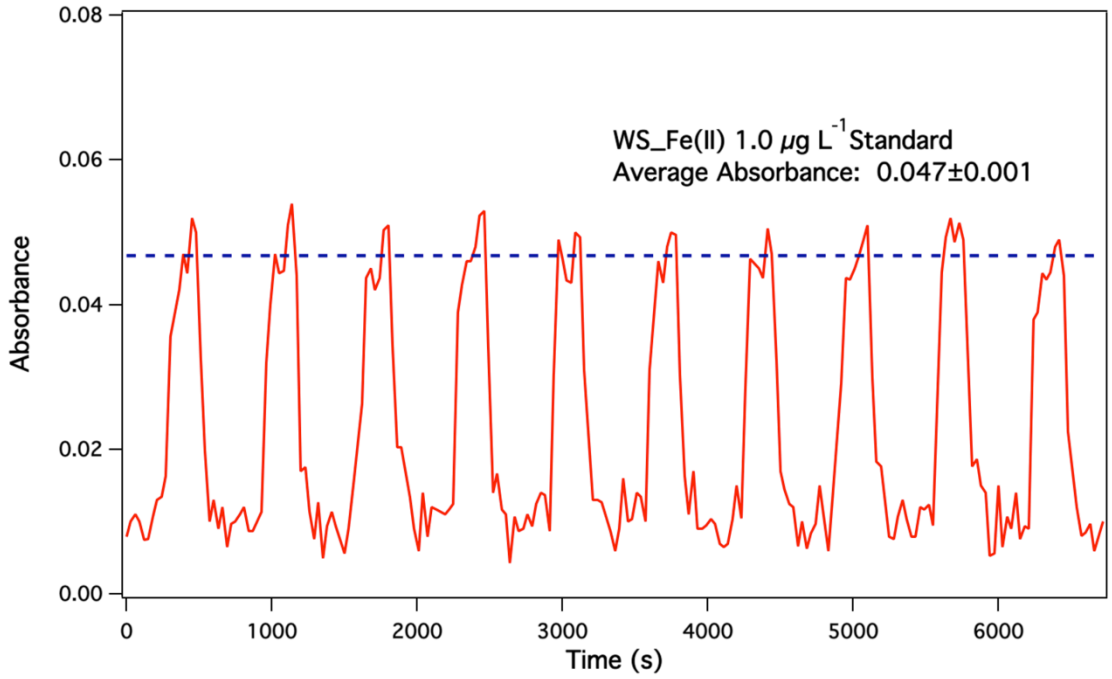

Figure 2.5. Light absorbance at 562nm of a 1 μg L^{-1} WS_Fe(II) standard analyzed 11 consecutive times using the PILS-LWCC liquid handling system. De-ionized water was analyzed before and after each standard run, resulting in a steady baseline. The dashed line represents the average light absorbance of 1 μg L^{-1} WS_Fe(II) standard for this analysis.

2.5.2 Instrumental Background, Detection Limit, and Method Uncertainty

Dynamic blanks were taken periodically for 1-1.5 hours/day during field operation of the PILS-LWCC to assess measurement interferences caused by

background noise (e.g. PILS instrumentation/operation or atmospheric gaseous components). During periods of dynamic blanks, ambient air was forced through a high efficiency particulate filter (HEPA filter, Pall Life Sciences) before being directed to the PILS, resulting in an aerosol-free sample (e.g. background sample). This background sample was ultimately subtracted from the ambient WS_Fe(II) concentration to produce background-corrected ambient data. A time series of WS_Fe(II) ambient and background signals during a summer ground-based field study in Atlanta, GA is shown in Figure 2.6. A line was interpolated through each 1-1.5 hour-long dynamic blank sample, yielding a continuous background signal during this sample period. Although the background signal is relatively consistent throughout the field study, there is some variability within this data. This variability is especially apparent when the background sample was collected during periods of high transient WS_Fe(II) peaks (outlined in blue boxes in Figure 2.6). During these peaks, the background signal is notably higher than the signal during periods lacking these events. This elevated background is likely due to carryover effect from high ambient concentrations to the background signal and is common in online/semi-continuous measurement systems. The mean WS_Fe(II) level determined from dynamic blanks was 8.2±2.5 ng m^{-3} (N of background samples=10) for the entire study and 4.2 ± 1.5 ng m^{-3} (N of background samples=11), when WS_Fe(II) transient events were omitted. Based on 3X the standard deviation of the dynamic blank (transient WS_Fe(II) events omitted), the method limit of detection was calculated as 4.6 ng m^{-3}. Although the LOD exceeds the ambient WS_Fe(II) concentration in the marine environment, it is well below the majority of ambient

signal observed during this study and in other urban settings [*Majestic et. al.*, 2006]. The method uncertainty was calculated to be 12% based on combined uncertainties of liquid flow rates (10%), air flow rates (5%), and the precision of the liquid handling system (3%). Overall, the background levels, detection limit and method uncertainty show that the PILS-LWCC can be used to explore WS_Fe(II) in typical urban environments.

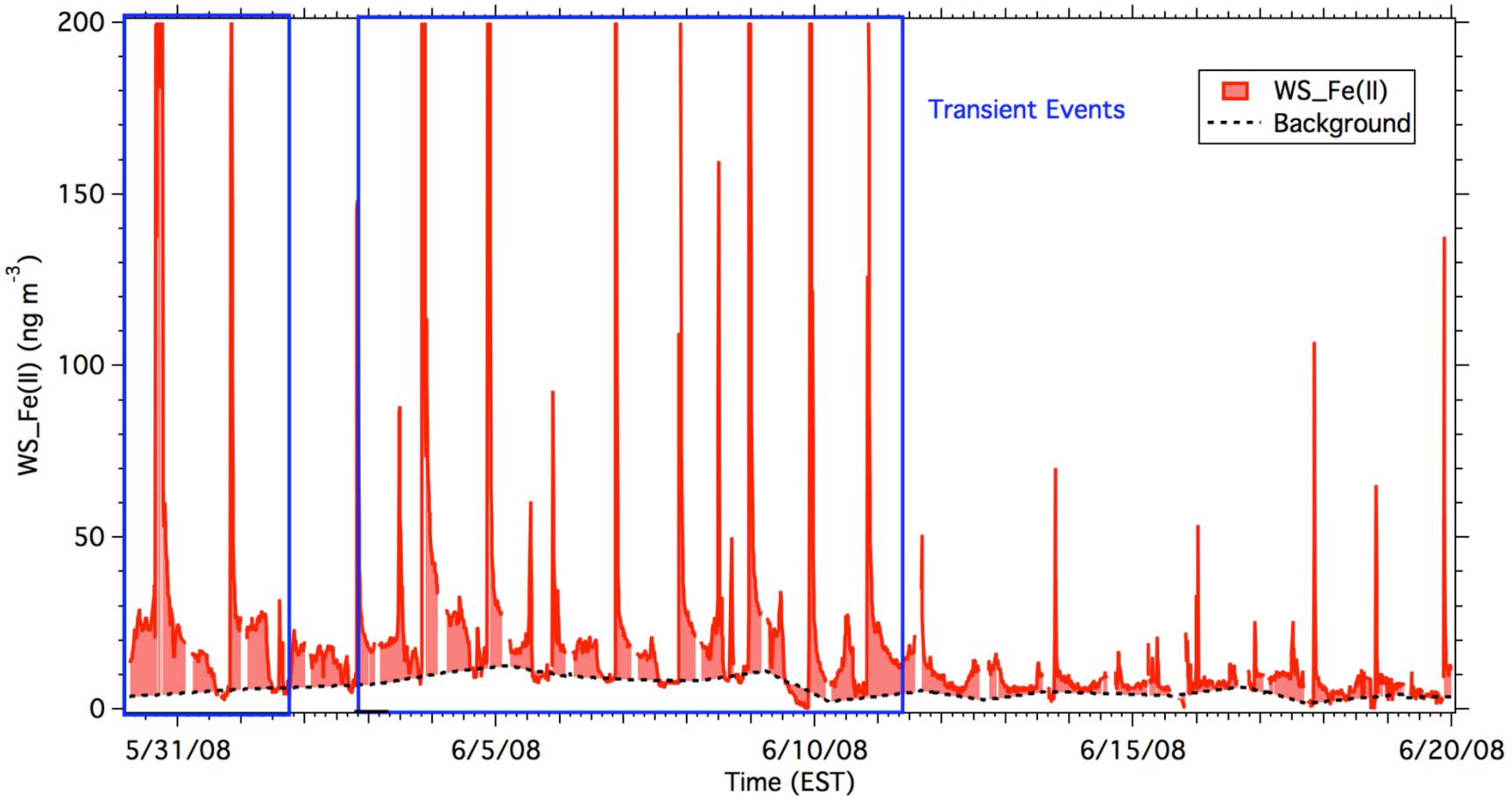

Figure 2.6. Time series of WS_Fe(II) measurements from the PILS-LWCC taken during a ground-based field study in Atlanta, GA during summer 2008. WS_Fe(II) is presented as red shading, and the instrument background (HEPA filtered ambient air) is shown by the black dashed line. The blue box outlines WS_Fe(II) transient events characterized by significantly elevated concentrations that were observed during this field study.

2.5.3 Artifacts

Because iron is a non-volatile species, sampling artifacts are generally associated with changes in oxidation state that occur during sample treatment and/or storage. These artifacts may largely affect the way WS_Fe(II) is interpreted, thus, a direct assessment of artifacts stemming from the PILS-LWCC is essential. Loss of WS_Fe(II) may occur during sample collection due to the specific conditions the particle is exposed to inside the PILS. For example, particles are exposed to 100°C for a short period of time, before being rapidly cooled (< 1 s residence time [*Orsini et al.*, 2003]), which may potentially drive the oxidation of WS_Fe(II). Redox changes may also occur from rapid dilution of the particles during condensational growth, resulting in a potential increase in particle pH, also driving oxidation of WS_Fe(II).

In addition to artifacts associated with sample collection, sampling biases may result from sample preparation. For example, *Murray and Gill* [1978] showed that the ferrozine compound can induce oxidation upon complexation of WS_Fe(II). However, *Hong and Kester* [1986] demonstrated that this particular mechanism is expected to account for less than 10% of WS_Fe(II) loss with the reagent concentrations relevant to this study. Furthermore, while ferrozine specifically complexes with WS_Fe(II), other transition metals (e.g. Cu(I) and Co(II)) can interact with ferrozine forming a colored complex, leading to an overestimation of WS_Fe(II) in solution. Intercomparison of PILS-LWCC measurements with filter-based techniques were used to assess the issue of positive and negative artifacts associated with sample collection and preparation of this technique.

2.6. PILS-LWCC vs. Filter Comparison

Filters were collected during periods of PILS-LWCC operation at two urban field sites (Fire Station 8 and Jefferson Street) in Atlanta, GA and a field site adjacent to a prescribed burn in South Georgia. During these periods, PM2.5 was collected on Zeflour or Teflon filters for approximately 24-hours at a nominal flow rate of 16.7 L min^{-1}. After sample collection, filters were immediately stored in sealed, dry polyethelene bags in the dark at 4°C and analyzed within 2-4 days to minimize oxidation of Fe(II). For WS_Fe(II) analysis, the filters were manually extracted into ultrapure de-ionized water for 30 minutes by ultrasonication. The filter extract was then forced through a 0.45um-pore size syringe filter (removing insoluble particles with diameter larger than 0.45um), and analyzed using the ferrozine technique (12-minute operationally defined measurement). The time delay between filter extraction and WS_Fe(II) analysis was typically 60 minutes.

Figure 2.7 shows the comparison between filter and PILS WS_Fe(II) separated by different field studies. In general, the PILS-LWCC WS_Fe(II) compares well with the filter-based measurements during these field studies. Deming regressions of PILS and filter WS_Fe(II) measurements of the urban (w/out the transient events) and prescribed burning field studies show similar slope values that are close to 1 (PILS/filter WS_Fe(II) = 0.84 ± 0.10 , indicating that the PILS-LWCC yields reasonable WS_Fe(II) concentrations based on existing technology.

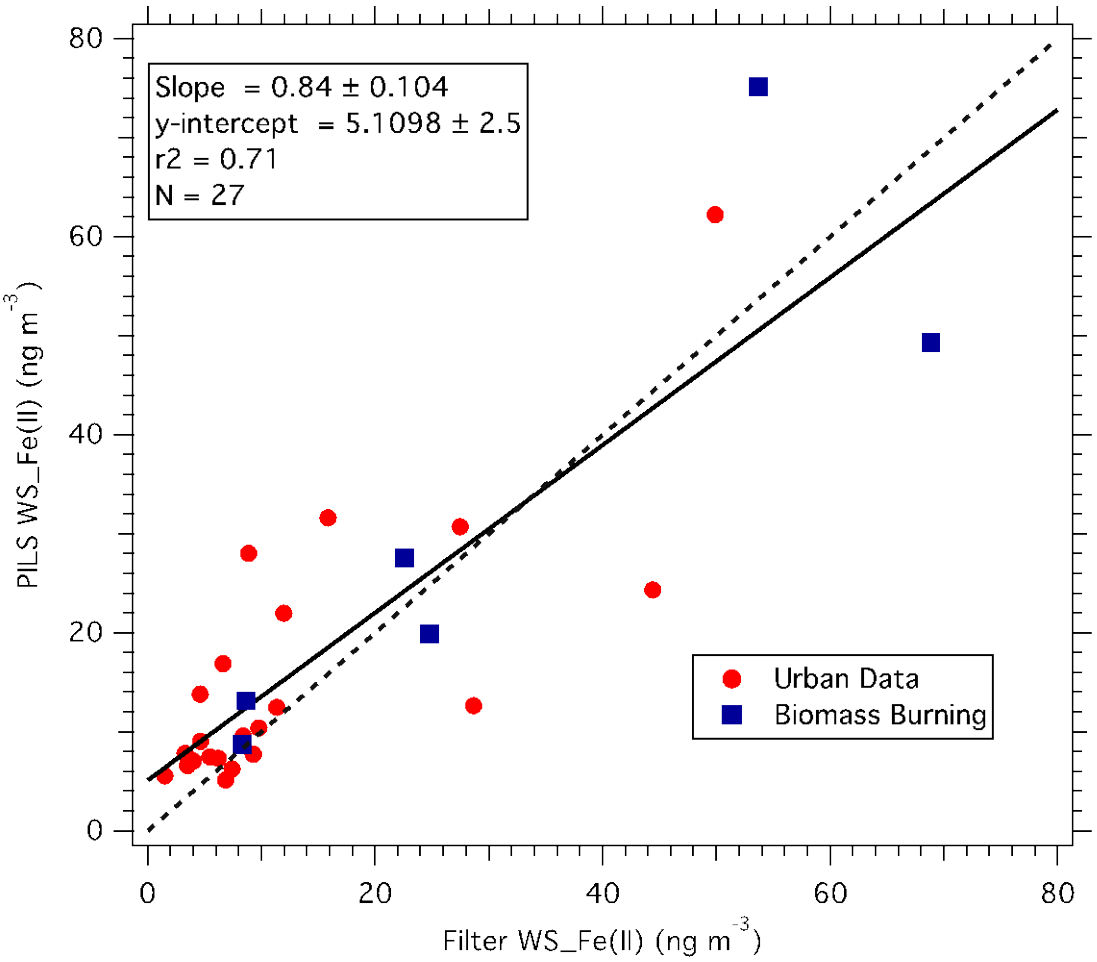

Figure 2.7. Comparison WS_Fe(II) measurements taken collected using the PILS and filter-based techniques. Measurements were collected from urban (red circles: Fire Station 8 and Jefferson Street) and biomass burning field studies (blue squares: South Georgia). The dashed line represents the Deming regression of data. The solid line is a 1 to 1 line.

Though there is generally good agreement between filter and PILS WS_Fe(II) (r2 = 0.71), a moderate amount of scatter is evident. As discussed earlier in this chapter, redox changes in Fe aerosol can occur during sample storage or treatment, leading to WS_Fe(II) sampling artifacts. These potential redox changes that occur during filter storage or filter/PILS sample treatment likely caused the scatter within this comparison. For instance, it is possible that WS_Fe(II) was oxidized during PILS collection. However, this potential PILS sampling artifact is likely counteracted by WS_Fe(II) oxidation that occurs

during filter extraction when WS_Fe(II) particles are in aqueous solution for an hour. Through this comparison, it appears that artifacts exist for both filter and PILS-based measurements, indicating that WS_Fe(II) measurements are operationally-defined. While measurement artifacts may be inevitable using the PILS-LWCC method, this method marks major progress in measuring trace metals in fine atmospheric aerosols that has significantly improved measurement time resolution from conventional filter-based techniques. However, the results in this study clearly highlight the challenges inherent with this measurement.

2.7 Modifications to the PILS-LWCC

The PILS-LWCC was later modified to measure WS_Fe(II) and WS_Fe (e.g. total soluble iron: WS_Fe(II) + WS_Fe(III)) in fine atmospheric aerosols. The performance, field-deployment, and validation of this modified technique are discussed in detail in Appendix A.

CHAPTER 3

CHARACTERIZATION OF WS_FE(II) IN URBAN AND RURAL REGIONS USING NEAR REAL-TIME DATA

In this chapter, WS_Fe(II) measurement from urban sites in the Eastern USA: Atlanta, Georgia, Dearborn, Michigan, and a prescribed burn in Ichauway, GA are presented. These results are compared to meteorology parameters and other highly time-resolved measurements of atmospheric species to characterize WS_Fe(II) temporal variability and investigate sources and atmospheric processes that may affect ambient WS_Fe(II) concentrations.

3.1 Sampling Sites

3.1.1 Dearborn, Michigan

The PILS-LWCC with a PM2.5 inlet was deployed at a public school parking lot in Dearborn, Michigan (42.307°N, -83.150°W), a suburb ~20 km southwest of central Detroit, during the Lake Michigan Air Directors Consortium (LADCO) winter field campaign from 19 January – 8 February 2008. Detroit, Michigan, and its surrounding counties are consistently non-attainment areas for PM2.5 National Ambient Air Quality Standards. *Hammond et. al.* [2008] showed that air quality in east and southwest Detroit (near Dearborn, Michigan) is impacted by coal combustion, gasoline/diesel traffic, and industrial sources (iron/steel manufacturing plants, oil refineries, sewage sludge incinerator, and automotive manufacturing plants).

The Dearborn sampling site was located in the center of the River Rouge industrial area, where many point sources, including power plants, steel mills, petroleum refineries, and auto plants, are located within a 10 km radius of the site, and mixed with residential

neighborhoods. A rail-switching yard directly south of the site and a steel mill that manufactures hot-rolled carbon steel sheet metal was approximately 1 km SW of the site. Significant heavy-duty diesel truck traffic associated with industrial activity was common on local streets.

Supporting measurements taken at this site included hourly concentrations of elemental and organic carbon (EC and OC) using an on-time ECOC analyzer (Sunset Laboratory, Forest Grove, Oregon) following the NIOSH 5040 method [*Birch*, 1998; *NIOSH*, 1996]. Hourly PM2.5 mass concentrations were measured with a Tapered Element Oscillating Microbalance (Thermo Fisher Scientific Inc., Walthan, Massachusetts). Hourly averaged meteorological data were available from a local meteorological station approximately 1km NW of the sampling site.

3.1.2 Atlanta, GA

To provide insight on seasonal variability, the PILS-LWCC was deployed in Atlanta, Georgia, during periods in fall (PM10), spring (PM2.5) and summer (PM2.5) at two different sites: Fire Station 8 (33.802°N, -84.435°W) and Jefferson Street (33.776°N, -84.413°W). These sites are located approximately 3 to 4 km from central Atlanta and are separated by approximately 2 km. WS_Fe(II) measurements from these sites offer a general representation of the air quality in metropolitan Atlanta; although, the Fire Station 8 site is known to have locally high aerosol concentrations (annual average higher by 1-2 $\mu g/m^3$). Fire Station 8 is located in a mixed industrial-commercial area with two large rail yards within ~200 m. A fire station and traffic intersection with significant diesel truck/automobile traffic are also located within ~50 m of the site. The Jefferson Street site is part of the Southeastern Aerosol Research and Characterization Study (SEARCH) and

Aerosol Research Inhalation Epidemiology Study (ARIES). This site is located in a mixed commercial/residential area and has a characteristic urban signature [*Solomon et al.*, 2003]. A Greyhound bus maintenance facility with frequent diesel bus traffic during daytime hours and several busy roadways with traffic intersections are located within ~200 m from the site. *Hansen et al.* [2006] provides a detailed description of the site. Receptor modeling of PM2.5 total iron from this site has shown that it is mostly associated with vehicular, industrial and crustal sources [*Liu et al.*, 2005].

The PILS-LWCC was operated at Fire Station 8 during a three-week fall period (16 Nov- 8 Dec 2007) without the cyclone inlet (PM10), a one-week spring period (16 April - 22 April 2008) and a three-week summer period (1 June - 20 June 2008) with the cyclone installed (PM2.5). Ancillary measurements pertinent to the study included 5 minute measurements of light-absorbing PM2.5 aerosol mass using an AE-16 single channel aethalometer (Magee Scientific Company, Berkeley, California), one-minute particle number concentration measurements using either a Condensation Particle Counter (TSI Incorporated, Shoreview, Minnesota) or an Optical Particle Counter (Met One, Grants Pass, Oregon) and meteorology parameters. Later in the summer (4 August - 6 September 2008), the PILS-LWCC (PM2.5) was moved to the Jefferson Street site for the August Mini-Intensive Gas and Aerosol Study (AMIGAS) field campaign that included the deployment of several continuous aerosol and gas-phase measurements. Semi-continuous measurements of PM2.5 major inorganic anions (SO_4^{2-}, NO_2^-, NO_3^-, Cl^-) and cations (NH_4^+, Na^+, K^+, Ca^{2+}) were provided by the PILS-IC [*Orsini et al.*, 2003]. Five-minute averages of criteria gases (SO_2, O_3, and NO_y), meteorological parameters, PM2.5 mass concentrations (TEOM; Thermo Fisher Scientific Inc., Walthan, Massachusetts), and one-hour averages of light-absorbing

aerosol (Aethalometer, Model RTA8, Magee Scientific Company, Berkely, California) were provided by the existing techniques deployed for the SEARCH study.

3.1.3 Biomass Burning: Ichauway, GA

A prescribed burn performed in early March 2008 in a longleaf pine and wiregrass forested region (~ 400 acres) provided the opportunity to characterize WS_Fe(II) emissions from biomass burning. These prescribed burning activities were in Ichauway, Georgia (31.276°N, -84.472°W), and organized by the Joseph W. Jones Ecological Research Center. The PILS-LWCC (PM2.5) and a suite of sampling instruments were deployed directly adjacent to the burn area to characterize aerosol and gaseous emissions. Water-soluble potassium (PM2.5), a tracer for biomass burning, was measured in 8-minute integrals by an electrochemical technique using an additional PILS. An Optical Particle Counter (Met One, Grants Pass, Oregon) provided 1-minute size-resolved number concentration (0.3μm - 2.5μm).

3.2 Results and Discussion

3.2.1 Dearborn Measurements: Urban/Industrial Site in Winter

The January 2008 Dearborn LADCO study afforded an opportunity to measure PM2.5 WS_Fe(II) in an industrial setting during winter when atmospheric photochemical processes are expected to be at a minimum. Measurements of WS_Fe(II) were taken during a roughly 2-week sampling period when the mean temperature was -3.3°C, but ranged widely from -14.3°C to 17°C. Mean and median concentrations of PM2.5 WS_Fe(II) during the study were 17.7 and 9.8 ng m^{-3}, respectively (Table 3.1). The data show significant temporal variability (Figure 3.1), with concentrations ranging from below the detection limit (LOD) to 434 ng m^{-3}. During episodes of snowfall, representing roughly 30% of the

data, PM2.5 WS_Fe(II) concentrations were typically below the detection limit of 4.6 ng m^{-3}, likely due to the wet deposition of WS_Fe(II) (Figure 3.1). The data suggest a regional background concentration of approximately 10 ng m^{-3} with frequent PM2.5 WS_Fe(II) peaks (8 peaks in an 18 day period) ranging from 50 to 400 ng m^{-3} lasting for 6 to 12 hours. No correlation was found between PM2.5 WS_Fe(II) and PM2.5 mass concentration during these peaks (R^2=0.004, N=48 for 8 transient events), indicating that the observed WS_Fe(II) was not linked to any other major PM2.5 chemical component. These higher PM2.5 WS_Fe(II) concentration events typically occurred during low wind-speed periods (Figure 3.1) suggesting influences from local emissions.

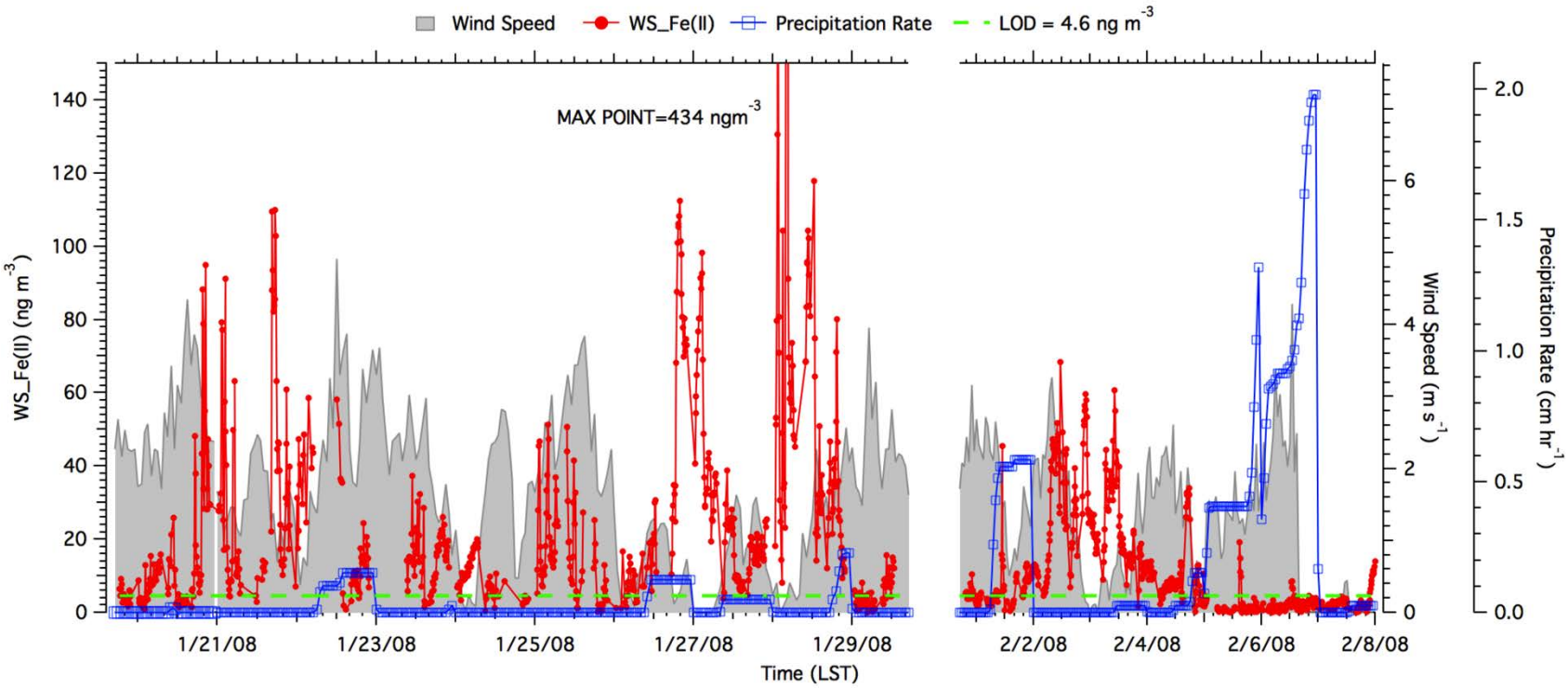

Figure 3.1. Time series of PM2.5 WS_Fe(II) (red dotted line) and wind speed (gray shading) in Dearborn, MI during part of the 1-month study. The WS_Fe(II) LOD of 4.6 ng m^{-3} and precipitation rate is indicated by the dashed green line and blue squares, respectively.

Table 3.1. WS_Fe(II) statistics for all measurements at the various sampling sites during different seasons. All concentrations are presented in ng m^{-3} at ambient temperature and pressure.

Season	*Sample Period*	*PM Size*	*Min*	*Max*	*% below LOD*	*Mean*	*Med*	*Std Dev*	*N*
Fall ATL FS8	11/16/07 - 12/6/07	PM10	LOD	195	4.6	34.8	24.2	30.5	1401
Spring ATL FS8	4/16/08 - 4/22/08	PM2.5	LOD	64.5	27.0	14.8	10.5	13.7	456
Summer ATL FS8	6/1/08 - 6/20/08	PM2.5	LOD	356.1	36.7	13.4	6.9	28.3	2050
Summer ATL AMIGAS JST	8/10/08 - 9/6/08	PM2.5	LOD	41.8	49.7	5.1	4.6	3.6	1278
Dearborn, MI LADCO	1/19/08 - 2/8/08	PM2.5	LOD	434	30.2	17.7	9.8	26.3	1458

Note, for the statistical analysis data below, the LOD are included as a value of 1/2 LOD

The wind roses in Figure 3.2 show that highest wind speeds were predominately from the southwest, but highest concentrations were mainly from the south. Industrial sources located within 10 km south of the site include a coal-fired power plant, a cement kiln, a large petroleum refinery, a wastewater treatment plant, and two steel mills. Correlation between PM2.5 EC or OC and PM2.5 WS_Fe(II) throughout the study were not significant (R^2=0.03 and 0.12, respectively N=323 (for both EC and OC analysis), based on 12-minute WS_Fe(II) merged to the 48-minute OC and EC measurements) indicating that industrial emissions likely influenced PM2.5 WS_Fe(II) rather than mobile emissions.

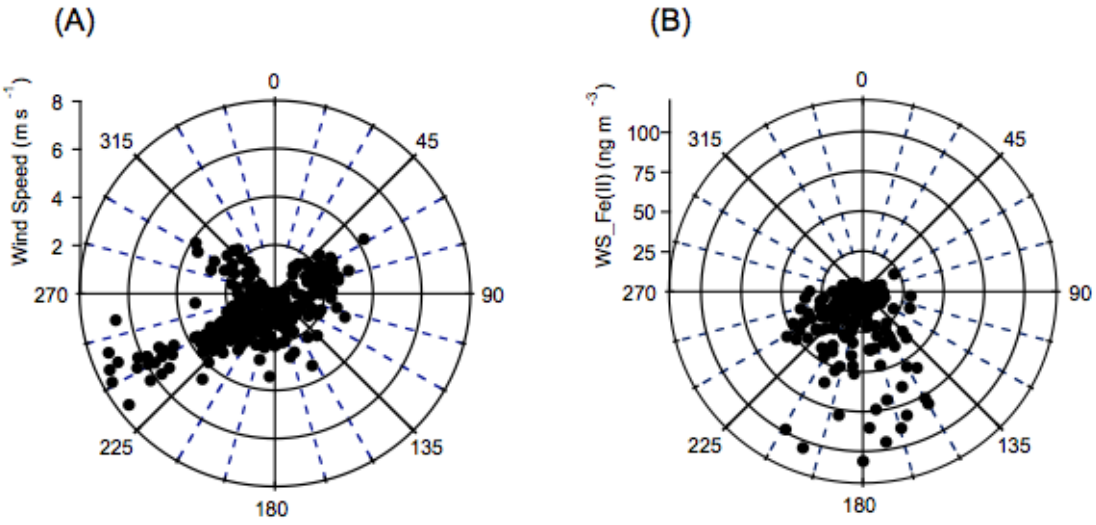

Figure 3.2 Wind rose plots of data from the Dearborn, MI study showing hourly-mean meteorological parameters and PM2.5 WS_Fe(II) concentration. a) Wind speed (m s^{-1}) versus wind direction, b) PM2.5 WS_Fe(II) concentration (ng m^{-3}) versus wind direction (a data point, 434 ng m^{-3}, is off scale)

3.2.2 Atlanta: Measurements During Various Seasons

3.2.2.1. Overall Seasonal Variability and Transient Events

Measurements of WS_Fe(II) were completed in Atlanta, GA at Fire Station 8 during three different seasons to investigate seasonal and temporal variability. In addition to these measurements, the AMIGAS study during August/September 2008 in Atlanta provided an opportunity to measure WS_Fe(II) simultaneously with several other atmospheric tracer species for a more comprehensive investigation of sources. Statistical summaries of WS_Fe(II) measurements at the Atlanta sites are given in Table 1.

The median WS_Fe(II) concentrations recorded at the Atlanta Fire Station 8 site during fall, spring, and summer were typically from LOD to 24.2 ng m^{-3}, for both PM10 and PM2.5, with highest concentrations in the fall associated with PM10. The measured levels are of similar magnitude to those reported for PM10 soluble (total = II +III) iron in Los Angeles, CA, East St. Louis, Illinois, and Waukesha, Wisconsin (from 0.4 to 11 ng m^{-3}) [*Majestic et al.*, 2007] and downwind of China (TSP 32 ng m^{-3}) [*Chuang et al.*, 2005]. However, these concentrations are roughly 1 to 2 orders of magnitude higher than fine and coarse levels of WS_Fe(II) recorded in remote marine regions [*Johansen et al.*, 2000; *Siefert et al.*, 1999]. Fire Station 8 median concentrations tended to be higher in spring compared to summer, and lowest concentrations (median: 4.6 ± 3.6 ng m^{-3}) were observed in August and September during the AMIGAS study at the Jefferson Street site. The observed seasonal variability could be associated with differences in meteorology (e.g., prevalent wind direction, boundary layer height) or chemical processes, such as enhanced

summertime photochemistry and oxidant concentrations shifting iron away from the Fe(II) oxidation state [*Sedlak et al.*, 1997]. However, there is evidence for redox chemistry playing a role in the WS_Fe(II) seasonal trend since an extensive data set of total water-soluble iron collected from 24-hr integrated FRM filters consistently shows higher total water-soluble Fe in summer (mean: 40-50 ng m^{-3} for J, J, A) compared to fall/winter months (mean: 15–20 ng m^{-3} N, D, J, F) for several years. In this method, iron was quantified by Inductively Coupled Plasma-Optical Emission Spectroscopy (ICP-OES) or Inductively Coupled Plasma-Atomic Absorption Spectroscopy (ICP-AAS) on aliquots obtained through aqueous extraction of FRM filters. Although the difference in our WS_Fe(II) and the total water soluble iron seasonal trend may be caused by differences in analytical techniques (ICP-OES/ICP-AAS vs. UV/Vis spectroscopy) and/or sample extraction (filter vs PILS), it may also be a direct result of WS_Fe(II) shifting to a more oxidized state at times when photochemistry and oxidant concentrations are expected to be enhanced (e.g. summer).

The Atlanta Fire Station 8 datasets exhibited high temporal variability in all seasons with concentrations ranging from the LOD to approximately 200 ng m^{-3} in the fall, and LOD to approximately 350 ng m^{-3} in the summer. Figure 3.3 shows a time-series of a multi-day period during November (PM10) and June (PM2.5), both at Fire Station 8. In November, WS_Fe(II) concentrations varied during all hours of the day (Figure 3a), a feature that was also observed in the spring dataset (data not shown). In contrast, temporal variability during June measurements was largely driven by unique transient PM2.5 WS_Fe(II) events that generally occurred in the

early evening and lasted for approximately 1-2 hours. Peak concentrations reached ~200-350 ng m^{-3}, which were superimposed on a low WS_Fe(II) background of ~ 10 ng m^{-3} that was present for most of the day. These events consistently occurred over roughly a 16-day period and then ended. A dramatic decrease in wind speed roughly 1-2 hours prior to these events was also observed (Figure 3b). Although wind directions were variable at these peak WS_Fe(II) times (consistent with low wind speeds), most peaks were associated with winds from the southern quadrants (SE to SW). For a short period (2-3 days) during these events, measurements were made of particle number concentrations with a CPC (D_p range:0.01 to > 1μm) and OPC (D_p range:0.3 to > 5μm). PM2.5 WS_Fe(II) peaks tracked well with the CPC data but not with the OPC data, suggesting increases only in the ultrafine particle number concentration (sizes below ~0.1 μm diameter). In addition, no correlation was observed between PM2.5 WS_Fe(II) and light absorbing aerosol (e.g., soot; R^2 = 0.0001, N=101, for total of 7 events). The combination of correlation with ultrafine particle number concentrations and lack of correlation with black carbon suggests that these WS_Fe(II)-rich particles were associated with fresh combustion-related activity, but likely not related to internal combustion engines (mobile sources). Due to the clockwork nature of these transient events around 2000 to 2200 every night, these events appear to be related to a regular activity occurring near the sampling site.

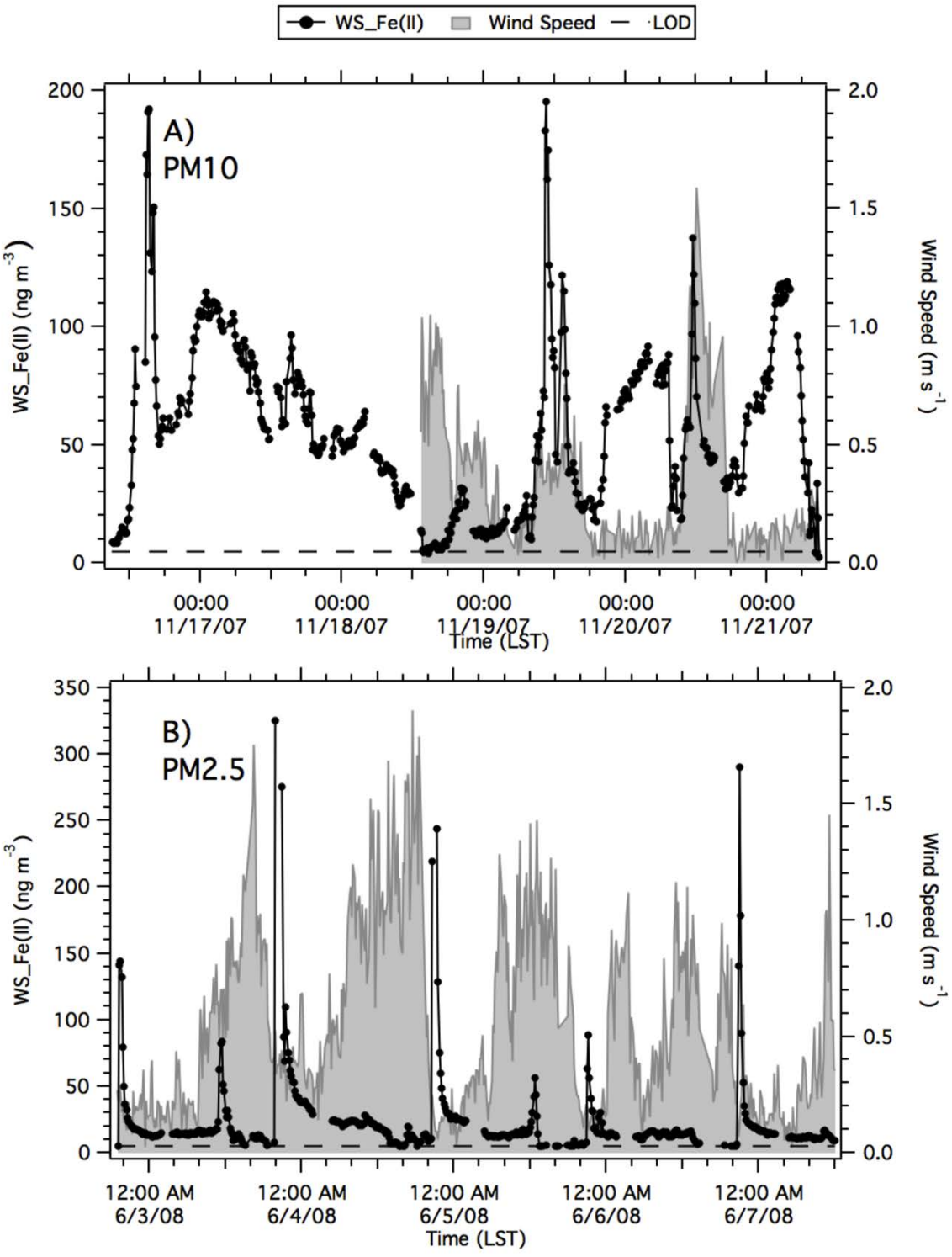

Figure 3.3 Examples of WS_Fe(II) time series measured in Atlanta for 5-day periods during a) Fall and b) Summer. The dotted black line represents WS_Fe(II) concentration, and the dashed black line represents WS_Fe(II) LOD (4.6 ng m^{-3}). Wind speeds are also plotted (gray shading) when data is available.

3.2.2.2 Transient Events: WS_Fe(II), SO_2, SO_4^{2-} and Particle Acidity:

Additional transient PM2.5 WS_Fe(II) events were observed in Atlanta during the 1-month (August-September 2008) AMIGAS study at Jefferson Street, but with much smaller peak concentrations (typically 10-40 ng m^{-3}). Because this intensive study involved continuous real-time measurement of trace-gas and aerosol composition, a more detailed analysis of the source of the observed WS_Fe(II) peaks was feasible. These WS_Fe(II) events occurred during a three day period when wind speeds (~2.5 m s^{-1}) were low, and the highest PM2.5 mass concentrations (~34 μg m^{-3}) were observed, suggesting stagnant atmospheric conditions. In addition, the average PM2.5 sulfate (SO_4^{2-}) concentration increased to ~7 to 10 μg m^{-3} from typical concentrations of ~2 to 4 μg m^{-3}. In general, these transient WS_Fe(II) events tracked well with mid to late afternoon peaks in PM2.5 SO_4^{2-} concentration that were associated with SO_2 peaks. Similar late afternoon SO_4^{2-} peaks have been observed in Atlanta during the summer and are thought to result from the entrainment of relatively near-by coal-fired power plant SO_2 emissions into the expanding daytime planetary boundary layer, combined with afternoon photochemical production of SO_4^{2-} [*Weber and al.*, 2003]. These events also tracked well with PM2.5 mass data (data not shown), which is consistent with large increases of PM2.5 SO_4^{2-}, which is a major component of PM2.5 in Atlanta. Figure 3.4 shows the average diurnal trends for SO_2, SO_4^{2-}, and WS_Fe(II) (based on hourly-averaged data), and indicates that for all three compounds, increases in concentrations were most often observed during late afternoon.

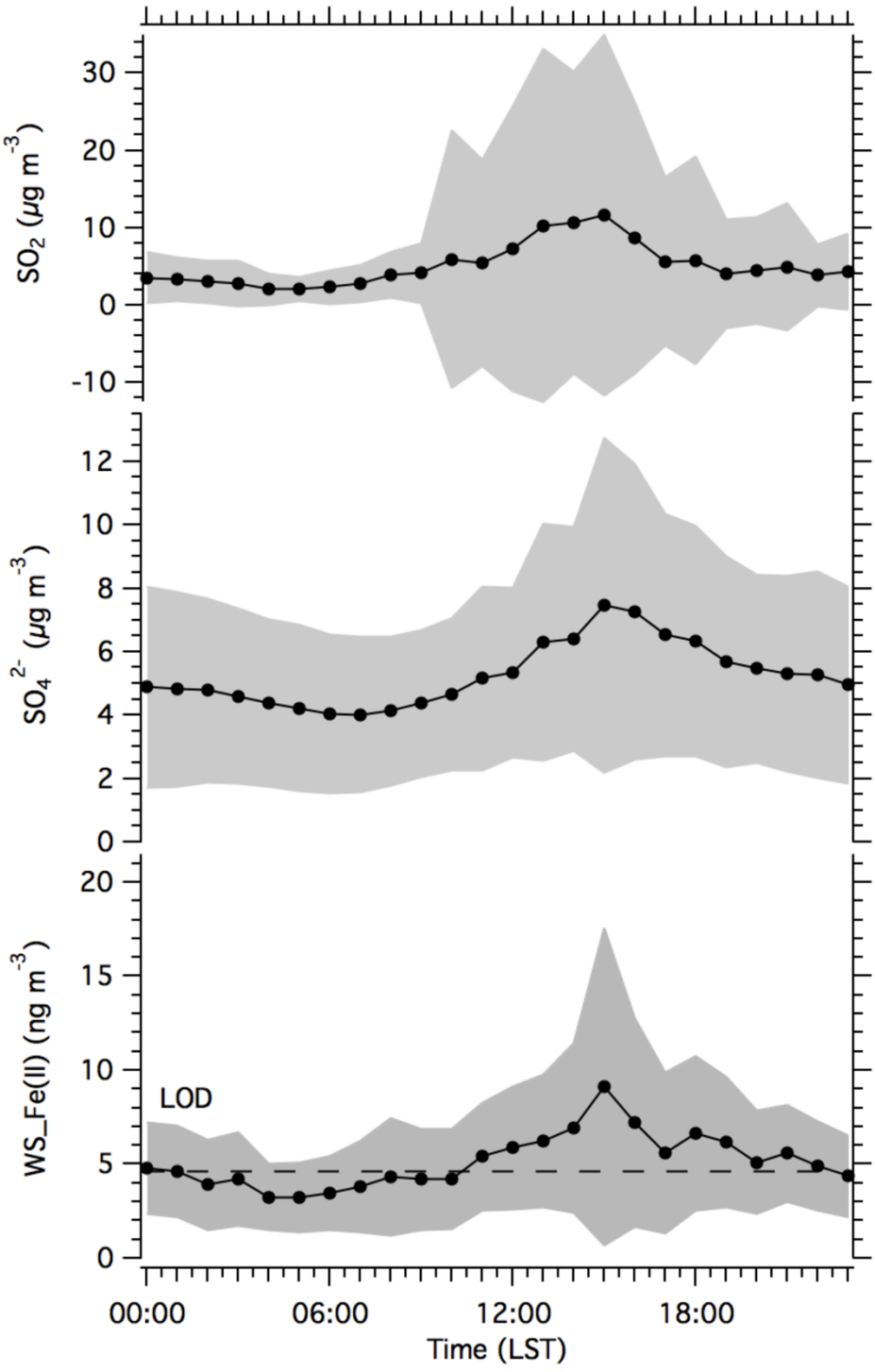

Figure 3.4 Mean (dotted black line) and plus/minus one standard deviation (gray shading) of hourly-averaged data for PM2.5 WS_Fe(II), SO_4^{2-}, and SO_2 during August-September 2008 AMIGAS study in Atlanta. The dashed black line represents the WS_Fe(II) LOD (4.6 ng m^{-3}).

Figure 3.5 shows real-time measurements of SO_2, SO_4^{2-} and WS_Fe(II) compounds for the three-day period during the AMIGAS study. Although the SO_4^{2-} peaks followed SO_2 maxima data, the relative proportions in peak heights varied. Differences in proportions of SO_2 and SO_4^{2-} for the various plumes can be attributed, at least in part, to differences in photochemical aging, where more aged plumes are expected to have higher SO_4^{2-} relative to SO_2 due to photochemical conversion of SO_2 to SO_4^{2-}. Photochemical age, for example, may account for the differences in proportions between SO_2 and SO_4^{2-} for peaks labeled A (more fresh) and B (more aged) in Figure 5. During this time period, peak concentrations of WS_Fe(II) tend to follow SO_4^{2-} but not SO_2. Event B exhibited the highest SO_4^{2-} and WS_Fe(II) concentrations recorded for the AMIGAS study, but the associated SO_2 maxima was clearly not the highest observed. These comparisons suggest that PM2.5 WS_Fe(II) was associated with the SO_2 plumes, but for the most part, WS_Fe(II) was not emitted directly along with SO_2. Several studies have shown that coal-fired power plant fly ash emissions contain iron [*Reddy et al.*, 2005; *R D Smith*, 1980], and this may be the source of the WS_Fe(II) observed here; however, other factors appear to influence the enhancement and/or stability of WS_Fe(II). A few studies suggest that aerosol acidity may play a role in enhanced WS_Fe(II) concentrations through an influence on iron solubility and stability [*Duce and Tindale*, 1991; *Meskhidze et al.*, 2003; *Zhuang et al.*, 1992], while one study observed no relationship between increased Fe solubility and atmospheric acidic species [*Baker et al.*, 2006]. At low pH values, the solubility of various forms of insoluble iron, such as iron oxides, is enhanced, and transformations between iron oxidation states are substantial

slower; thus, WS_Fe(II) may persist in the particle for longer periods of time. During the AMIGAS study, it is possible that either WS_Fe(II) or insoluble iron was internally mixed with highly acidic SO_4^{2-} particles formed by SO_2 oxidation, resulting in either increased stability of WS_Fe(II) or the mobilization of insoluble iron to WS_Fe(II).

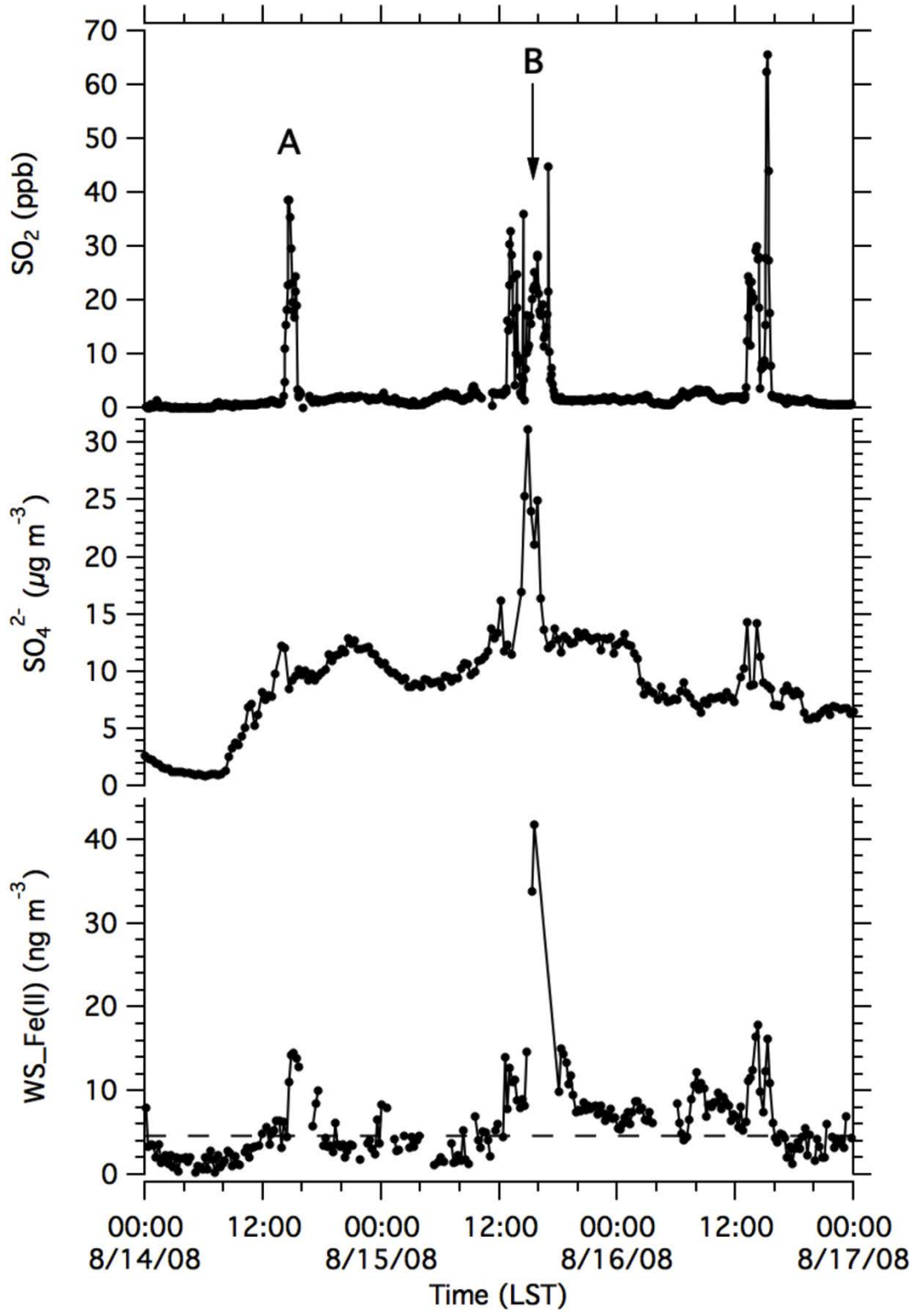

Figure 3.5 Sample time-series during a three-day period of the AMIGAS study showing transient SO_2 events and corresponding PM2.5 SO_4^{2-} and WS_Fe(II).

For a more comprehensive analysis, SO_2 and WS_Fe(II) data for the entire AMIGAS study (August – September 2008) were merged onto the SO_4^{2-} measurement 20 minute time scale. If SO_2 concentration increased 4 times the background concentration of 1 ppbv during the entire study, the peak was deemed an SO_2 transient event. For each SO_2 peak, the average concentration increase relative to background levels was determined for SO_2, SO_4^{2-}, and WS_Fe(II) (denoted as ΔSO_2, ΔSO_4^{2-}, and ΔWS_Fe(II)). For example,

$$\Delta WS\_Fe(II) = \frac{\sum (WS\_Fe(II)_i - WS\_Fe(II)_b)}{n}$$

where, $WS\_Fe(II)_i$ is the concentration recorded in the peak, $WS\_Fe(II)_b$ the average of the WS_Fe(II) concentration measured at the time just prior to and after the SO_2 peak, and *n* is the number of measurements made within the WS_Fe(II) peak. In addition to this analysis, the degree of aerosol acidity was assessed through an ion balance between the suite of measured PM2.5 anions and cations, since aerosol pH was not directly measured. Studies in Atlanta have shown that the major ions associated with fine particles are SO_4^{2-} and NH_4^+, with much lesser amounts of NO_3^- [*Solomon et al.*, 2003]. Other ions (ie. crustal elements) are only minor components of Atlanta PM2.5 and do not significantly contribute to the ion balance [*Solomon et al.*, 2003]. Ratios of $(SO_4^{2-} + NO_3^-)/ NH_4^+$ in equivalence units that are greater than one result from an excess of SO_4^{2-} and NO_3^- relative to NH_4^+, which is likely balanced

by the unmeasured H^+ cation and correspond to an acidic aerosol. Aerosol particles near neutral will have anion/cation equivalent ratios near one.

A total of 17 SO_2 peaks were observed during the study, and shown in Figure 3.6 are the ΔWS_Fe(II) correlations with ΔSO_2, ΔSO_4^{2-} and the anion/cation ratio for each peak. Unfortunately, during AMIGAS there were few large sulfate peaks; thus, the correlations tend to be dominated by the one major peak (event B) observed in the afternoon of August 15, 2008, when the relative change in SO_4^{2-} concentration was ~8 μg m^{-3} compared to other peaks where the change was in the range of 1-2μg m^{-3}. The results show a general increasing trend between ΔWS_Fe(II) and apparent aerosol acidity. The correlation with SO_4^{2-} is also expected, since plumes with highest sulfate are likely to be the most acidic, due to titration of all available neutralizing ammonia.

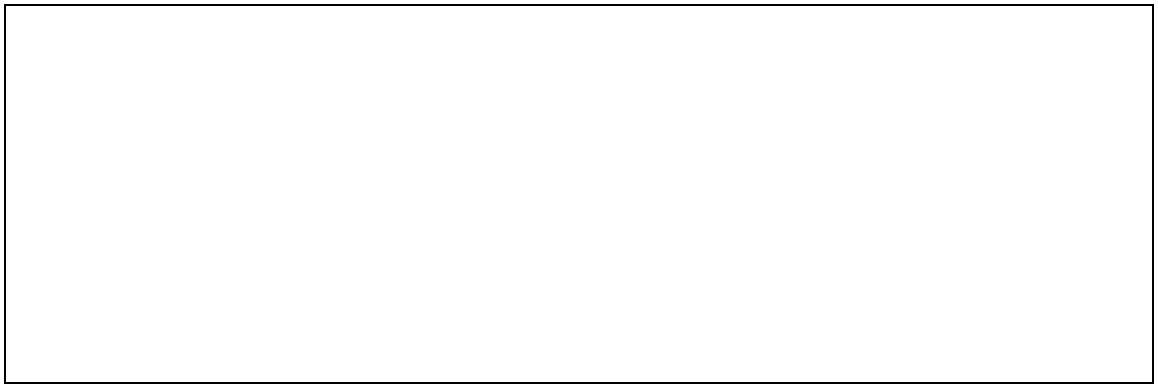

Figure 3.6 ΔWS_Fe(II) correlation to ΔSO_2, ΔSO_4^{2-}, and the anion/cation equivalence ratio for each of the 17 SO_2 peaks observed during AMIGAS. ΔWS_Fe(II) is the average WS_Fe(II) concentration increase relative to background concentrations (average of WS_Fe(II) recorded at the time just before and after the SO_2 peak). For each plot the coefficient of determination (R^2) is given for all data and when the largest peak during Event B (open circle, also see Figure 5) is excluded.

These data also suggest that the PM2.5 WS_Fe(II) and sulfate were internally mixed (present in same particles), which in turn would imply that most WS_Fe(II) was associated with accumulation mode particles (the size that most secondary sulfate particles occur). Given that the PILS-LWCC only measures WS_Fe(II) and no other online WS_Fe(III) and total Fe were available during the AMIGAS study, the exact sources of the iron in these plumes cannot be identified. Thus, we cannot determine whether WS_Fe(II) or some form of iron, that was later acid-processed to WS_Fe(II), was co-emitted with SO_2. However, WS_Fe(II) does not appear to have been emitted directly with the SO_2. It is also possible that catalytic conversion of SO_2 to SO_4^{2-} in aqueous drops containing H_2O_2 by Fe(II)[*Breytenbach et al.*, 1994] may have played a role.

The influence of SO_2 plumes in the transient PM2.5 WS_Fe(II) events observed at Fire Station 8 cannot be assessed since comparable time resolved SO_2 or aerosol SO_4^{2-} measurements are not available. However, most of the June Fire Station 8 events shown in Figure 3b were different than those observed during the AMIGAS study, both in magnitude and timing. In general, the Fire Station 8 peak concentrations were significantly greater and were typically observed much later in the day, often near midnight; thus, suggestive of different sources or processing of WS_Fe(II).

3.2.2.3 Diurnal Variability and Photochemical Processes

Some studies have observed diurnal variability in WS_Fe(II), possibly driven by photochemical processes. For example, *Willey et al.* [2000] attributed daytime increases in rainwater Fe(II) measurements to photo-reduction processes. This

well-studied mechanism for the formation of WS_Fe(II) in atmospheric liquid water involves conversion of Fe(III) complexed to specific organic acids (i.e. carboxylic acid moieties) through a ligand-to-metal charge transfer yielding reduced iron and an oxidized organic complex [*Pehkonen et al.*, 1993].Other studies focusing on cloud water samples, however, have not observed a diurnal trend of WS_Fe(II) that is indicative of photochemical activity [*Parazols et al.*, 2006].

To investigate if a persistent diurnal pattern in WS_Fe(II) was present in our measurements, the data for each season was binned into hourly mean WS_Fe(II) concentrations. Figure 3.7 shows the diurnal variability for the Atlanta measurements during three different seasons. Specific transient WS_Fe(II) events were removed from the dataset prior to binning and averaging the data that were apparently associated with a source other than photo-reductive processes, such as the late evening transient events during the summer at Fire Station 8 (Figure 3.7c), and all WS_Fe(II) associated with the SO_2 events during the AMIGAS study (Figure 3.7d). All other data are included in the averages plotted in Figure 3.7. Based on this analysis, no net increase in WS_Fe(II) concentration was observed during the daytime; therefore, we conclude that iron photo-reductive processes do not appear to have a significant net effect on the ambient WS_Fe(II) concentration during the periods studied at these sites. However, it is possible that WS_Fe(II) was formed by photo-reductive processes during the study, but was counterbalanced by the WS_Fe(II) lost from oxidative processes, resulting in no net increase in ambient concentrations during daytime hours.

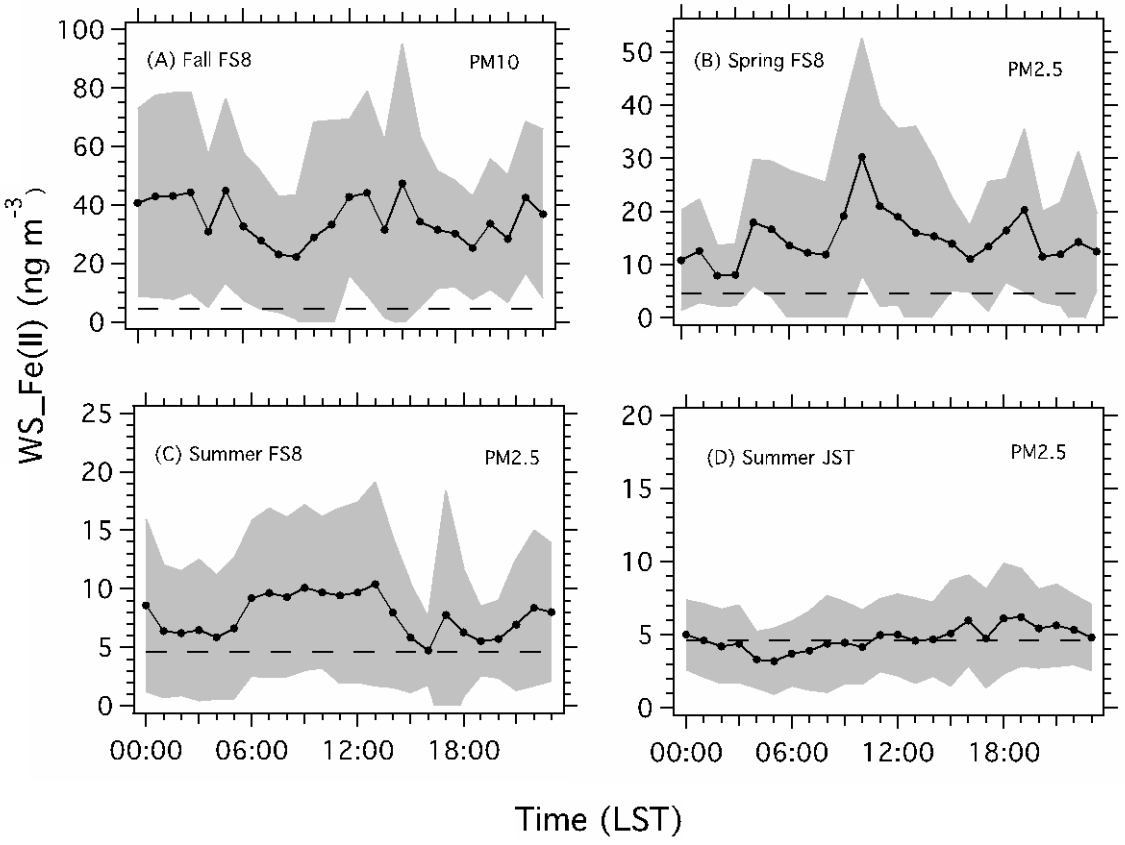

Figure 3.7 Diurnal trends during different seasons in Atlanta, GA. For each plot, the dotted black line represents mean hourly WS_Fe(II) concentration and the gray shaded area is plus/minus one standard deviation. The dashed black line represents the WS_Fe(II) LOD. FS8 stands for Fire Station 8 site, and JST stands for Jefferson Street site. Transient events were removed from Summer FS8 and Summer JST data prior to binning and averaging.

3.2.2.4 Mobile Sources: WS Fe(II) and Light Absorbing Aerosol

As discussed above, no correlation was observed between PM2.5 light-absorbing aerosol (or elemental carbon, EC) and WS_Fe(II) during the wintertime at Dearborn, MI. A similar result was observed in Atlanta throughout all the measurements at the Fire Station 8 and Jefferson Street sites (r^2=0.34, N=744 fall (FS8); r^2=0.04, N=342 spring (FS8); r^2=0.004, N=1637 summer (FS8); r^2=0.01,

N=535 summer (AMIGAS), based on 5-minute measurements of light-absorbing aerosol merged to WS_Fe(II) 12-minute data at FS8 and 12-minute WS_Fe(II) data merged to 1-hour light absorbing aerosol data for AMIGAS). However, there are studies showing a link between iron, mobile sources [*Hammond et al.*, 2008; *Majestic et al.*, 2009] and EC [*Chuang et al.*, 2005]. *Chuang et al.* [2005] found a strong relationship between 24-hour integrated WS_Fe, believed to be primarily WS_Fe(II), and EC (R^2=0.7) as well as no association between enhanced iron solubility and mineral dust events based on measurements from Cheju, Korea. They conclude that WS_Fe was better associated with long-range transport of Asian anthropogenic emissions related to combustion processes rather than processing of mineral dust. We do not view these results as contradictory to our results. Although EC is mainly linked to mobile emissions (in the absence of biomass burning) in North America [*Schauer*, 2003 *and references within*] this is not the case in Asia, where it can be associated with coal or other forms of fossil fuel emissions [*Streets et al.*, 2001]. For our sampling sites, mobile sources were not directly linked to enhanced WS_Fe(II) concentrations. In *Chuang et. al.* [2005], EC is not used as a specific tracer of mobile sources, but used as a more general tracer of Asian anthropogenic emissions. Another possibility for the poor correlation between EC and WS_Fe(II) during our sampling periods may be that soluble iron from mobile sources is predominately emitted as WS_Fe(III). Our findings combined with those by *Chaung et al.* [2005] highlight that more studies in different regions are required before we can accurately assess the relationship between combustion sources and water-soluble iron.

3.2.3 Impact of Biomass Burn Aerosols on Urban WS_Fe(II) Spatial Distribution

Studies have reported total iron concentrations in biomass burning emissions, which is typically a small portion (i.e. less than 1%) of total burn emissions [Chen et. al.2007; *Lee et al.*, 2005; *Yamasoe et al.*, 2000]. One study hypothesized that biomass burning emissions may be a direct source of water-soluble iron in aerosols. This same study further concluded that pyrogenic sources have only a minor impact on the atmospheric flux of soluble iron to the atmosphere (8.3×10^9 g yr^{-1}), representing roughly 10% of soluble iron from arid regions [*Guieu et al.*, 2005].

In this study, measurements of PM2.5 WS_Fe(II) were made in a prescribed burn to characterize fire emissions and determine whether these emissions could have an impact on Atlanta WS_Fe(II) concentrations. Figure 3.8 shows a time-series of particle number concentration (sizes between 0.3 to 2.5 μm diameter), PM2.5 water-soluble potassium (WS_K), and PM2.5 WS_Fe(II) during one period of the prescribed burning. A clear relationship between WS_Fe(II) and WS_K, a known marker for biomass-burning [*Andreae*, 1983], show that PM2.5 WS_Fe(II) is associated with biomass burning emissions. In these experiments, WS_Fe(II) and WS_K were highly correlated (R^2=0.88, N= 17) and based on linear regression, the emission ratio of WS_Fe(II) relative to WS_K was estimated at 15±2 mg/g (intercept of 2.7±3.1 ng m^{-3}).

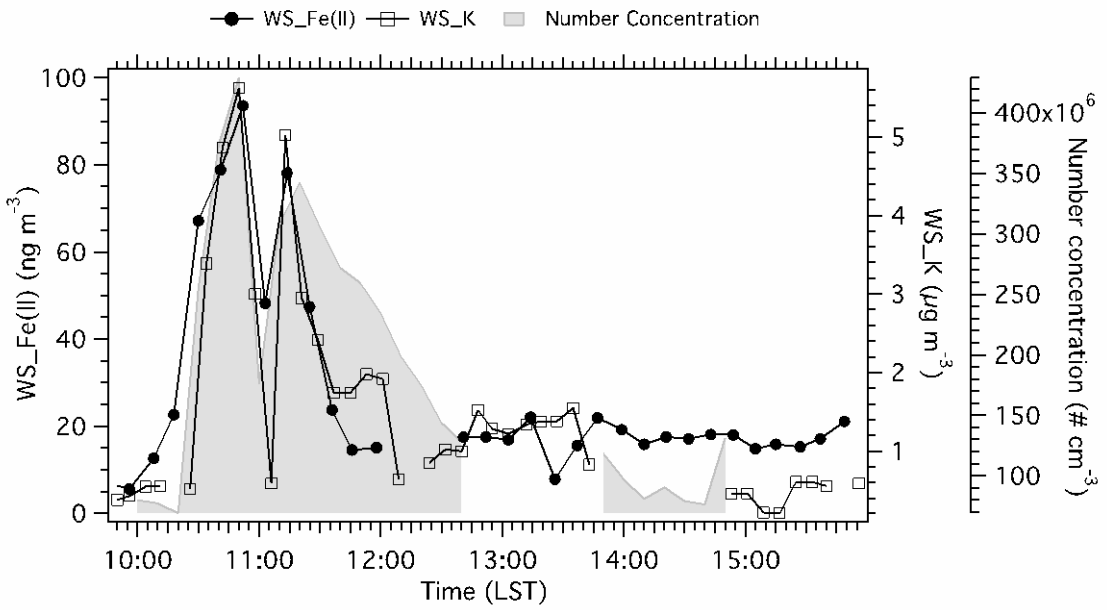

Figure 3.8 PM2.5 WS_Fe(II) (dotted black line), number concentration (particles larger than 0.3 μm diameter: gray shading), and fine particle WS_K (black open square line) during a prescribed burn in Icahauway, GA are presented when the site was impacted by two plumes.

Even within the region of burning the highest PM2.5 WS_Fe(II) concentration observed was only 94 ng m^{-3}. In comparison to the urban measurements, this is less than peak WS_Fe(II) levels recorded in Atlanta (~200-300 ng m^{-3}) or Dearborn (~400 ng m^{-3}), suggesting that biomass burning likely did not significantly contribute to the large transient events observed (this is also consistent with lack of correlation with light absorbing aerosol or EC).

Wood burning also likely did not significantly contribute to the background (regional) concentrations of WS_Fe(II) observed in Atlanta. For example, using the above emission ratio, and an analysis of 2007 FRM filters in urban Atlanta (South Dekalb, GA EPD Site), during winter when biomass burning is most prevalent, a

recorded mean WS_K concentration of 0.043 μg m^{-3} corresponds to a PM2.5 WS_Fe(II) concentration of only 0.7 ng m^{-3}, which is, below our instrument detection limit. Moreover, in the spring of 2007, extensive fires in South Georgia at times severely impacted Atlanta air quality over extended time periods. Based on 24-hour integrated filter measurements, maximum WS_K concentrations of 0.1 μg m^{-3} correspond to a WS_Fe(II) concentration of only 1.6 ng m^{-3}. Although this analysis is highly uncertain, when it is considered along with the relatively low PM2.5 WS_Fe(II) concentrations recorded next to the fires, it suggests that biomass burning was likely not an important contributor to the WS_Fe(II) measured in the urban regions of this study. Significant influence of biomass burning on ambient WS_Fe(II) concentrations are likely limited to regions that experience extensive forest fire impact in otherwise pristine environments.

3.3 Summary

To date, filter-based measurements with long (e.g., 24 hr) integration times have been used to quantify WS_Fe(II) and characterize sources in various environments. This study presents the first continuous and near-real-time WS_Fe(II) measurements from a number of sites. The following findings are reported:

1) Typical background PM10 and PM2.5 WS_Fe(II) concentrations recorded in Atlanta, GA and Dearborn, MI were on the order of tens of ng m^{-3}, which is comparable to WS_Fe(II) measured in other urban areas based on integrated filter sampling techniques.

2) Sampling at the various sites in Atlanta, GA during different seasons suggests a general trend: highest mean WS_Fe(II) concentrations were observed in fall/winter (mean: 34.8 ± 30.6 ng m^{-3}) and lowest concentrations recorded in summer (mean: 5.1 ± 3.6 ng m^{-3}). Integrated filter measurements in Atlanta, however, have shown an opposite seasonal trend for total water-soluble iron, with highest concentrations in the summer. These combined results may be linked to a higher conversion rate of WS_Fe(II) to oxidized forms of iron during periods of higher oxidant concentrations (e.g. summer).

3) High WS_Fe(II) concentrations were typically associated with frequent transient WS_Fe(II) events (~1-12 hours) at the urban sampling sites in this study. In Dearborn, event concentrations ranged from 100 to 400 ng m^{-3} and were likely associated with local industrial activity. At Fire Station 8 in Atlanta, unique summertime WS_Fe(II) transient event concentrations ranged from 200 to 350 ng m^{-3} and appeared to be linked to fresh combustion-generated particles from some unidentified activity near the site. Several transient WS_Fe(II) events in Atlanta were also found to be associated with SO_4^{2-} and SO_2 peaks, with a general increasing trend of ambient WS_Fe(II) concentrations with apparent particle acidity. However, the actual source of iron in the transient events both at Detroit and Atlanta sites could not be identified with our dataset.

4) Daily 1-hr averages of WS_Fe(II) concentrations at all urban locations and seasons showed no evidence for a significant or consistent diurnal trend, suggesting that photo-reductive processes did not result in a significant net increase in ambient concentrations of WS_Fe(II) during our study periods.

5) A poor correlation between WS_Fe(II) and light-absorbing aerosol (or elemental carbon, EC) was observed at all urban sites during all seasons, indicating that mobile source emissions are not directly linked to enhanced WS_Fe(II) concentrations.

6) WS_Fe(II) was associated with biomass burning emissions based on a strong relationship observed between WS_Fe(II) and WS_K (R^2=0.88). An emission ratio of WS_Fe(II)/WS_K = 15 mg/g (N=17) was estimated based on measurements within a prescribed burn of longleaf pine and wiregrass in south Georgia. Although significant WS_Fe(II) increases in concentration were observed within the prescribed burn (WS_Fe(II) range: 5 to 94 ng m^{-3}), the highest recorded WS_Fe(II) concentration near the burn region was less than typical transient events in Atlanta. While biomass burning likely impacts WS_Fe(II) in regions with high biomass burning activity, it is not believed to have had a significant influence on WS_Fe(II) in the urban regions we studied.

CHAPTER 4

CHARACTERIZATION OF IRON SPECIATION IN AMBIENT FINE AEROSOLS: INSIGHT ON FACTORS CONTROLLING IRON SOLUBILITY

The water-soluble portion of iron aerosols is associated with adverse health outcomes as catalysts for ROS formation and biogeochemical cycles, which in turn, impact the global climate. Several aerosol properties and atmospheric processes are hypothesized to have a significant impact on iron solubility, but major inconsistencies on the primary controls of solubility exist between field and laboratory measurements. These inconsistencies make it challenging to assess human health and climate impacts associated with iron aerosols. In Chapter 3, the sources and processes contributing to WS_Fe(II) aerosols, a significant portion soluble iron, were explored using a novel semi-continuous technique. Though these measurements provided unique insight on iron solubility, they could not provide information on speciation (oxidation state and chemical composition), a property that potentially influences iron solubility (soluble iron/total iron). In this chapter, iron speciation and particle mixing state (e.g. elemental associations), of single iron-containing particles from urban and rural regions are characterized and compared to iron solubility. These results are presented in this chapter and build on the knowledge of soluble iron aerosols established in Chapter 3.

4.1 Methods

4.1.1 Filter Collection and Storage

Iron particles collected on Teflon filters (Whatman, Piscataway, New Jersey: 47mm-diameter, 2um pore size) were analyzed using XANES and microscopic X-ray

fluorescence. Twenty-four hour integrated PM2.5 filters were collected during different seasons at three urban sites and one rural site (Table 4.1) for the ongoing Assessment of Spatial Aerosol and Composition in Atlanta (ASACA) air quality study (Butler et. al., 2003) and used in this analysis.

Table 4.1. ASACA filter information

ASACA sample site	*Site Type*	*Local Sources*	*Winter Date*	*Summer Date*
Fire Station 8 Atlanta, GA (urban)**	Industrial	Rail yard Diesel Traffic	1/28/10	6/3/09
Fort McPherson Atlanta, GA (urban)*	Commercial/ Residential	Major Interstate Mobile	2/10/09	6/8/09
South Dekalb Atlanta, GA (urban)*	Commercial/ Residential	Major Interstate Mobile	11/11/08	9/9/09
Fort Yargo Winder, GA(rural)**	State Park	Forested Region	11/29/09	7/4/09

*Analyzed with XANES in October 2009
**Analyzed with XANES in February 2010

During sample analysis, ambient air at a nominal flow rate of 16.7 L min^{-1} was pulled through a cyclone (URG, Chapel Hill, North Carolina USA), selecting for particles with an aerodynamic diameter less than 2.5 μm (PM2.5), then directed through a series of two annunlar glass denunders (URG, Chapel Hill, North Carolina USA), removing acidic and alkaline gases. The particles were then collected onto the Teflon filter (Whatman, Piscataway, New Jersey: 47mm-diameter, 2um pore size). Filter samples were subsequently cut using ceramic scissors with one half used for Fe solubility measurements and the other half used for synchrotron-based analyses.

Samples were stored in sealed polyethylene bags in a dark freezer (~-20°C) immediately after collection and were analyzed within 1 to 11 months. Because iron is non-volatile, sampling artifacts are likely associated with changes in iron

oxidation state during sample storage. *Majestic et. al.* [2006] studied this specific artifact in aerosol samples and observed minimal Fe(II) loss on samples stored in a dark freezer for periods up to 6 months. In addition, *Takahama et. al.* [2008] found no evidence for significant Fe(II) loss in samples stored in freezing temperatures over extended periods of time (> 1 year). Although Fe(II) loss due to chemical conversion is possible on these samples, it is not expected to be significant based on the sample storage time and conditions employed in this study.

4.1.2 Synchrotron-based X-ray spectroscopy

Synchrotron-based X-ray spectroscopy is based on the principle that every element has characteristic absorption edges that correspond to the binding energy of electrons in individual quantized shells (e.g. K, L_2, and L_3). In this technique, incident X-rays of sufficient energy bombard atoms, ejecting the electrons from an electron shell. Subsequently, an outer shell electron may relax into the vacated position, emitting a characteristic fluorescence signal. K-edge XANES spectroscopy, used in this study, specifically explores the absorption edge associated with the innermost, K-shell electrons. The ejected electrons of the innermost K-shell interact with neighboring atoms. These interactions are influenced by the type, oxidation state and structural arrangement of atoms in a particle and are reflected in XANES spectra [*Ingall*, 2011]. Thus, XANES spectra provide information on both oxidation state and the mineralogical structure associated with the element of interest.

A total of 221 iron-containing particles deposited on the Teflon filters were analyzed on the 2-ID-D beamline at the Advanced Photon Source at Argonne National Laboratory in Argonne, Illinois, USA. The 2-ID-D beamline uses an energy

dispersive Si-drift detector (Vortex EM, with a 50 mm^2 sensitive area, and a 12.5 μm Be window; SII NanoTechnology, Northridge CA, USA) to measure X-ray fluorescence of the sample. All measurements were conducted under a helium atmosphere in order to minimize absorption and fluorescence artifacts caused by low-Z elements in air. A randomly selected area of each filter sample (~0.5 cm^2) was placed over a slot of an aluminum sample mount for direct spectroscopic analysis of the iron particles on the filter. The sample was initially analyzed in microscopic X-ray fluorescence mode to identify regions on the filter with detectable iron concentrations (e.g. iron-containing particles). In this mode, a monochromatic X-ray beam with a diameter of ~400 nanometers was scanned over a filter area (typically ~40 X 40 μm) at a step size of 0.4 μm and 0.4 s dwell to produce an elemental distribution map of the filter. These maps were produced by setting the X-ray energy to 7200 eV, which allowed for the collection of K-edge X-ray fluorescence data on elements with masses from aluminum to iron (Al, Si, P, S, Cl, K, Ca, Ti, V, Cr, Mn, and Fe). The fluorescence data was converted into concentration data (μg/cm^2) for each element using a calibration with NBS standards. In addition to locating iron-containing particles, calibrated data from these maps was used to characterize the association of other elements with iron. An energy scan (e.g. XANES analysis) was subsequently collected for iron-containing particles identified in microscopy mode (typically 30 iron-containing particles/filter). The X-ray energy scale was calibrated to the iron K-edge (7112.0 eV) using an iron metal foil before XANES measurements were performed. The incident X-ray energy was varied from

7090 to 7180 eV in 0.5 eV increments using a monochromator for a 0.5-3.0 s dwell to produce an energy scan near the iron K-edge of a given iron-containing particle.

4.1.3 XANES spectra analysis using ATHENA software (2.1.1)

ATHENA software (version 2.1.1) was used to process the raw energy spectra. Individual energy scans were smoothed using a three-point algorithm for 10 iterations. The energy scans were subsequently normalized using the edge step normalization option to avoid mathematical discrepancies caused by directly dividing the fluorescence signal of incident X-ray beam by the signal in the upstream ionization chamber. The pre-edge centroid of the XANES spectra was the primary spectral feature used to determine oxidation state. The pre-edge centroid position was only determined from high intensity spectra (>5000 intensity counts: 103 spectra) to avoid any interferences caused by the low signal to noise ratio in low intensity spectra. The pre-edge feature was normalized by subtracting the pre-edge absorption from the background absorption, calculated by interpolating a cubic spline equation through the absorption 1 eV before and after the pre-edge feature. A Gaussian equation was fit to the normalized pre-edge feature to determine the pre-edge centroid position. In addition, XANES energy scans of a wide range of Fe(II) and Fe(III) minerals were collected at the 2-ID-D beamline. Similar pre-edge centroid analysis was applied to XANES standard data of common Fe minerals (augite, pyrite, iron (II) oxalate, iron (II) sulfate, goethite, hematite, iron (III) sulfate, iron (III) sulfate) to compare to ambient sample data. Oxidation state was determined by the relationship between oxidation state and pre-edge centroid position. In this study, a linear equation was interpolated through Fe(II) (augite,

pyrite, iron (II) sulfate, iron (II) oxalate) and Fe(III) (goethite, hematite, iron (III) oxalate and iron (III) sulfate) mineral data with the mean pre-edge centroid position of Fe(II) and Fe(III) minerals representing 0% Fe(III) and 100% Fe(III), respectively. The pre-edge centroid position determined from single particles was converted to % Fe(II) content using this interpolation. Several studies have used a similar approach to convert pre-edge centroid position of K-edge XANES spectra of octahedral-coordinated Fe minerals into % oxidation state [*Bajt*, 1994; *Lam and Bishop*, 2008; *Wilke et al.*, 2001].

4.1.4 Iron Solubility Analysis

Iron solubility of the filter samples was measured using the ferrozine technique by *Stookey* [1970], based on the absorption of light by the Fe(II)-ferrozine complex at 562nm to quantify Fe(II) in solution. A DTMini-2 equipped with a dual deuterium and tungsten halogen bulb (Ocean Optics: Dunedin, Florida, USA) provided light in the UV/VIS range (200-800nm), and a USB2000 spectrophotometer (Ocean Optics: Dunedin, Florida, USA) was used for light absorption measurements. A 100cm Liquid Waveguide Capillary Cell (LWCC) (World Precision Instruments: Sarasota, Florida, USA) provided a long liquid absorption path length to enhance measurement sensitivity. The spectrophotometer was calibrated using five ammonium Fe(II) sulfate standards ranging from 0 to 20 Fe(II) ppb liquid concentration (typical r^2=0.9999) before iron solubility analysis.

One half of each filter sample was placed in an acid-cleaned 30 ml amber Nalgene bottle, diluted by 15 to 20 ml of de-ionized water (>18.0 MΩ). PM2.5 was extracted into solution via 30 minutes of ultra-sonication. A 10 ml aliquot of the

extracted sample was filtered through a 0.45um PTFE filter (Fisher Scientific: Pittsburgh, Pennsylvania, USA) to remove insoluble particles (>0.45um diameter) from the solution. Ferrozine (5.1 mM) was added to the sample aliquot (100µl ferrozine/10 ml sample) and pulled through the LWCC after 10 minutes of incubation time. Light absorption was immediately measured at 562nm (max light absorption of Fe(II)-Ferrozine complex) and 700nm (background measurement) to yield a 10-minute operationally-defined soluble Fe(II) measurement. Hydroxylamine (HA) was subsequently added to the remaining filtrate (100 µl HA/10 ml sample) to reduce soluble Fe(III) to Fe(II). After 10 minutes of incubation time, the light absorption measurements were repeated following the same procedure as the Fe(II) measurements, yielding the total soluble iron (Fe(II) + Fe(III)) content of the filtrate. Fe(III) concentration was determined by subtraction of the Fe(II) soluble concentration from the total soluble iron concentration.

4.2. Results and Discussion

4.2.1 Identification of Iron-Containing Particles

Using microscopic X-ray fluorescence, several areas were scanned on each urban and rural filter (1 - 4 maps per filter) to map out the spatial distribution and concentration of elements from aluminum to iron (Al, Si, P, S, Cl, K, Ca, Ti, V, Cr, Mn, and Fe), referred to as elemental maps. Iron-containing particles were identified in this analysis and were subsequently analyzed using XANES spectroscopy. In addition, the elemental maps provided data on the elements that were associated with iron in each particle, thus particle mixing state. The combination of XANES spectra and microscopic X-ray fluorescence were used to characterize mineralogy.

Figure 4.1 shows an example of iron, aluminum, and silicon elemental maps from the South Dekalb winter (11/11/08) filter. The fourth map presented in Figure 1 shows the combined signal of all 3 elemental maps, indicating that both aluminum and silicon were associated with certain iron-containing particles in this sample.

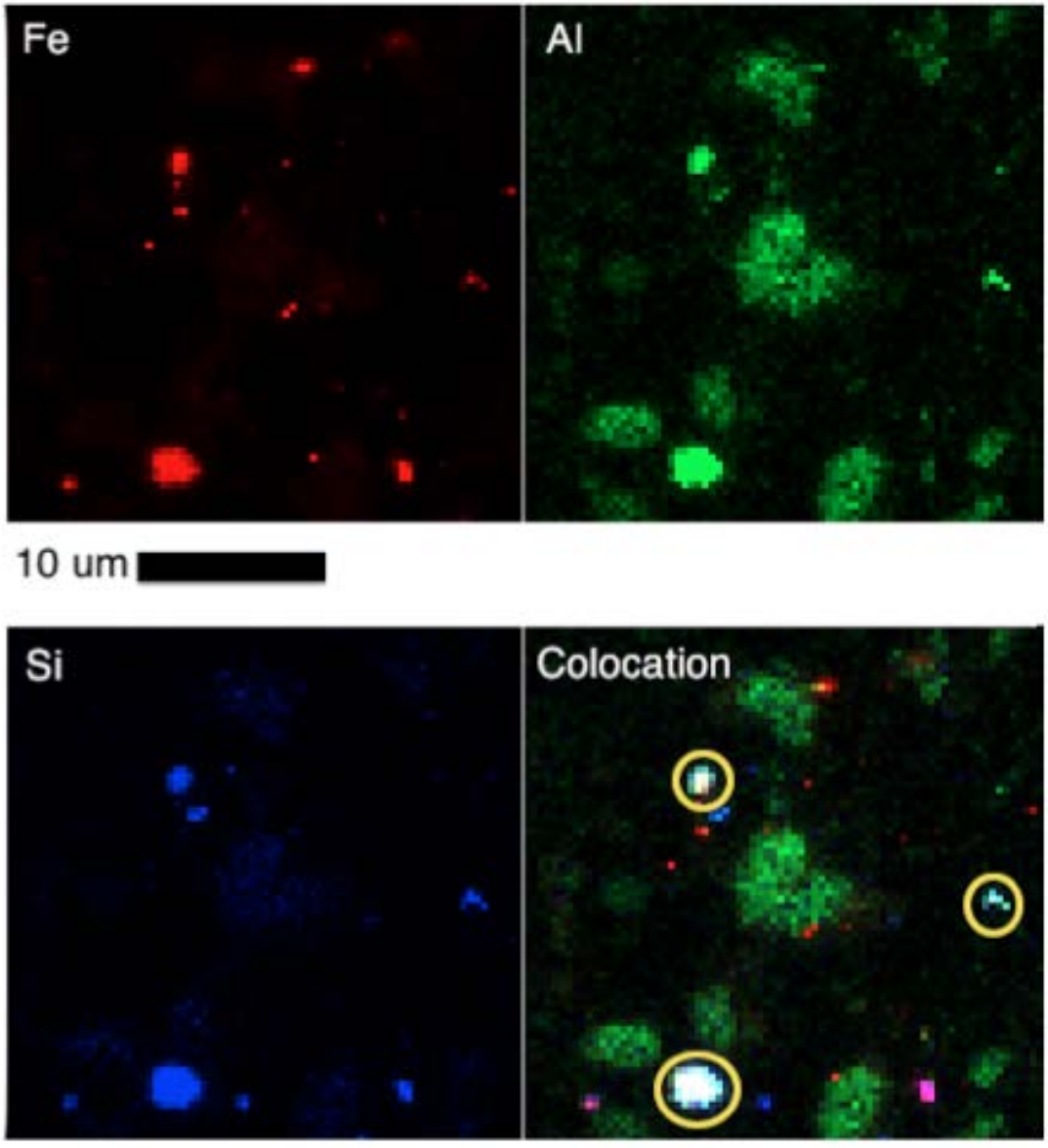

Figure 4.1 Elemental maps (30 X 30 um) of iron (red), aluminum (green), and silicon (blue) from South Dekalb 11/11/08 filter sample are presented. The fourth map is a colocation map, where the iron map is superimposed on aluminum and silicon maps. The white particles on the colocation plot indicate that iron, aluminum and silicon are concentrated in this area. The yellow circles on the colocation plot indicate 3 iron-containing particles that are enriched in aluminum and silicon.

As a test of the synchrotron-based techniques, the iron concentration determined from this study was compared to the iron concentration of filter samples collected for other field studies in Atlanta, but analyzed using different techniques (ICP-MS or ICP-AA). In this study, the iron concentration of a given elemental map (typically 40 X 40 μm) was multiplied by the total filter area divided by the elemental map area to determine the total iron concentration of the sample. When 2 or more elemental maps were collected for a given sample, the average of the total iron concentration from all elemental maps was used to determine the concentration of the sample. A wide range of iron concentrations was observed on the samples, ranging from 0.37 to 41.7 ug/cm^2, corresponding to ambient air concentrations between and 15 and 1734 ng/m^3. Although the total iron calculated using elemental maps had moderate uncertainty (Table 4.2), the majority (e.g. 7 out of 8) of the iron from our samples were within the range (mean ± standard deviation) of typical iron concentration observed in urban and rural sites in the Southeastern US (Table 4.2). However, the iron concentration (1734 ng/m^3) observed at the urban site Fire Station 8 during the winter was much higher than typical concentrations observed in Atlanta, GA and urban Southeastern US sites. Although this concentration was observed at Fire Station 8, which is characterized as an urban Atlanta site with poor air quality (e.g. PM mass concentration generally 30% greater than other Atlanta sampling sites (Trail, 2010)), the total concentration was probably a direct result of an uneven distribution of iron on the filter. Iron on this particular elemental map may have been concentrated with respect to the remaining sample area, leading to an overestimation of total iron collected on the

filter. This result reflects the uncertainties associated with calculating absolute concentrations of aerosol components using synchrotron-based technology. However, the majority of data appear to represent urban and rural areas in the Southeastern US well. In the following statistical analysis, this Fire Station 8 winter sample is excluded (*refer to Section 4.2.6*).

Table 4.2. Total Fe concentration measured in Southeastern US during 2008

Site	*Season*	*Mean*	*Median*	*Max*	*Min*	*Stdev*	*N*
Urban[a]	Summer	98.6	81.3	1030.0	15.4	66.2	154
	Winter	56.8	46.9	395.0	0.0	37.7	194
Atlanta, GA South Dekalb[b]	Summer	111.2	95.8	248.0	24.6	51.6	25
	Winter	61.2	45.8	172.0	6.5	46.8	25
Atlanta, GA Jefferson St.[c]	Summer	61.2	45.8	172.0	6.5	46.8	22
	Winter	49.0	36.0	184.8	2.7	34.6	73
Rural [d]	Summer	75.0	39.2	407.8	12.9	10.1	69
	Winter	22.2	20.5	74.9	2.7	20.0	71
Yorkville, GA [c,e]	Summer	54.1	33.8	331.2	10.5	66.3	29
	Winter	22.1	20.4	61.5	2.7	11.7	28

4.2.2 Iron Oxidation State and Mineralogy

The pre-edge centroid position is the primary XANES spectra feature used to determine oxidation state and coordination chemistry of a given iron particle. It has been widely used to study iron in common minerals in soils [*Prietzel et al.*, 2007; *Wilke et al.*, 2001] and continental shelf particles in the ocean [*Lam and Bishop*, 2008]. The energy of the pre-edge centroid position shifts anywhere from 1.4 to 3 eV for a change of one valence electron (e.g. Fe(II) to Fe(III)).

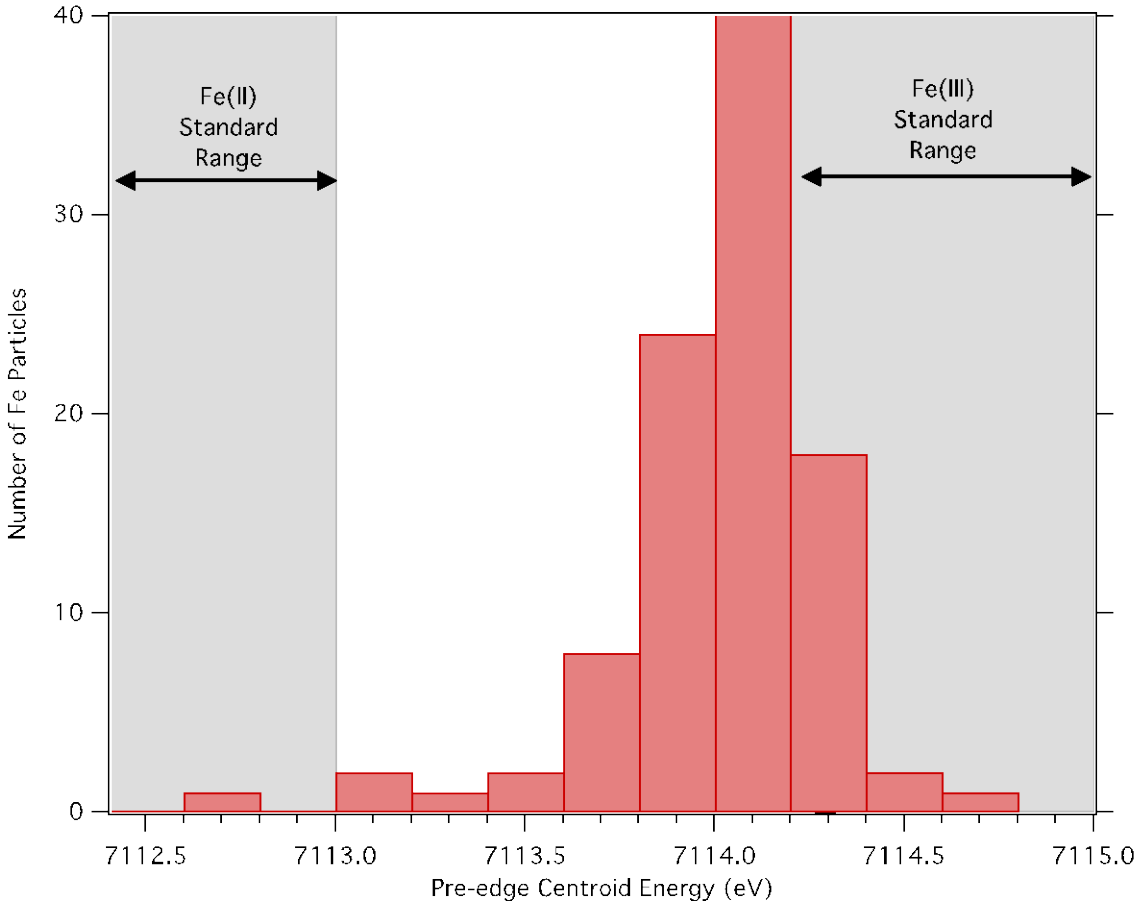

Figure 4.2 Histogram of pre-edge centroid energy positions determined from XANES spectra of individual iron particles from urban and rural sites is plotted. The gray shaded areas on the map represent the range of pre-edge centroid positions for common Fe(II) and Fe(III) minerals.

The pre-edge centroid position was calculated for 103 particles (e.g. particles with high intensity spectra, >5000 raw counts) from the filter samples. Figure 4.2 shows the distribution of pre-edge centroid positions for single iron-containing particles from our samples. The pre-edge centroid position varied by 2.05 eV among filter samples, ranging from 7112.75 to 7114.8 eV, with an average of 7114.0 ± 0.3, indicating significant oxidation state variability among our samples. The majority of the pre-edge centroid data for the urban and rural Fe particles falls between the centroid positions observed for Fe(II) and Fe(III) minerals (Figure 4.2). Figure 4.3 shows corresponding percent Fe(II) to total Fe of single particles, based on pre-edge centroid position, on each of the 8 filters identified by sampling site and season. The Fe(II) fraction in single particles from both urban and rural sites was generally between 5 and 35%, with the majority of the particles consisting of roughly 25% Fe(II). The rural site (Fort Yargo) during the winter had a much higher Fe(II) content than the other filters, having a mean Fe(II) content of 53%. In addition, a few particles (e.g. 6 out of 103) had much lower pre-edge centroid positions (7112.75 - 7113.15eV) compared to the average of the entire dataset (7114.0 eV), indicating iron in these particles was 100% Fe(II). The Fe(II) content of single particles in this study is greater than those observed by *Takahama et. al.* [2008], who showed a majority of marine and urban Fe aerosols exists as mixed-oxidation state agglomerations and surface-reduced particles, containing less than 10% Fe(II). The results presented in our study compared to those of *Takahama et. al.* [2008] suggests that large differences in iron redox state may characterize iron collected in different regions and seasons.

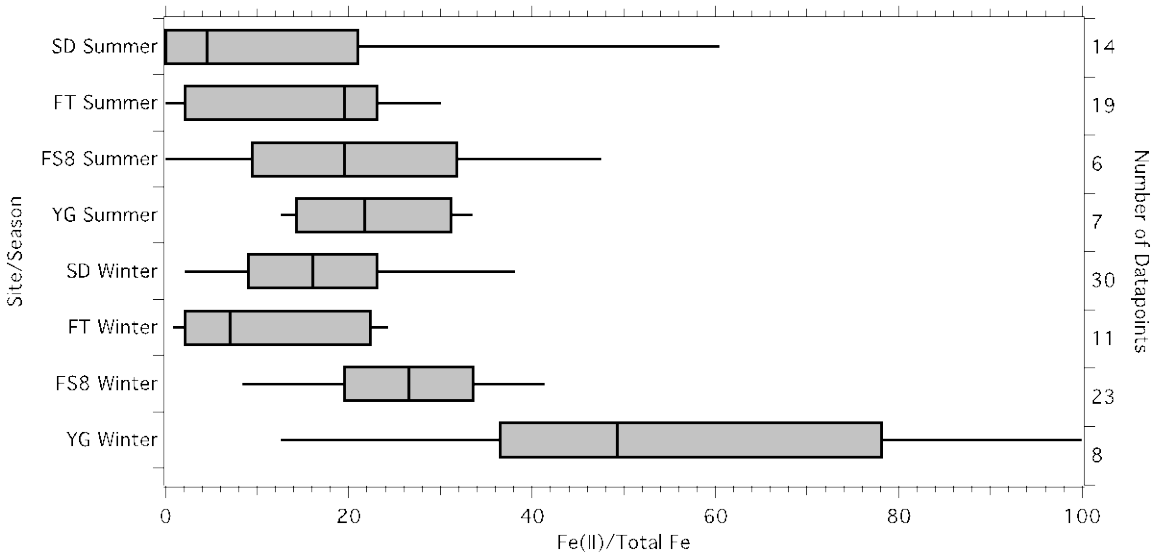

Figure 4.3. Percentage of Fe(II) to total Fe (Fe(II) + Fe(III)) observed in single particles on filter samples are plotted for individual sites separated by season. 50th percentile (black vertical line), 25th and 75th percentiles (upper and lower box), 10th and 90th percentiles (upper and lower whiskers) of each dataset are represented in this graph. The right axis represents the number of data points represented for each sampling site/season.

XANES spectra were similar for most of the Fe particles analyzed, regardless of season or site. Figure 4.4 shows a XANES spectra observed for a typical oxidized and reduced particle (based on pre-edge centroid position) observed in this study. Although the reduced particle shows a strong decreased shift in pre-edge and K-edge peak position, the shape of the spectra is similar to that of oxidized particles. Figure 4.5a shows the XANES spectra of a typical Fe particle observed in this study compared to the XANES spectra of several Fe(II) and Fe(III) compounds. The XANES spectra, for the most part, closely follows the spectra of iron oxides (e.g. goethite and hematite) and lacks a resemblance to other classes of Fe minerals, such as silicates (augite and biotite), sulfides (pyrite), organics (Fe(II) and Fe(III) oxalate),

and sulfates (Fe(III) sulfate), suggesting that the majority of Fe in urban aerosols is iron oxides. Further separation into specific Fe oxides was difficult, since differences in spectral features amongst this mineral class are very subtle. Most of the XANES spectra of the reduced particles follow the spectra of iron oxides with a shift in edge position; however, a few (2 out of 13) spectra of "more reduced" (pre-edge centroid position <7113.6eV) particles show a strong resemblance to silicates (e.g. biotite) shown in Figure 4b.

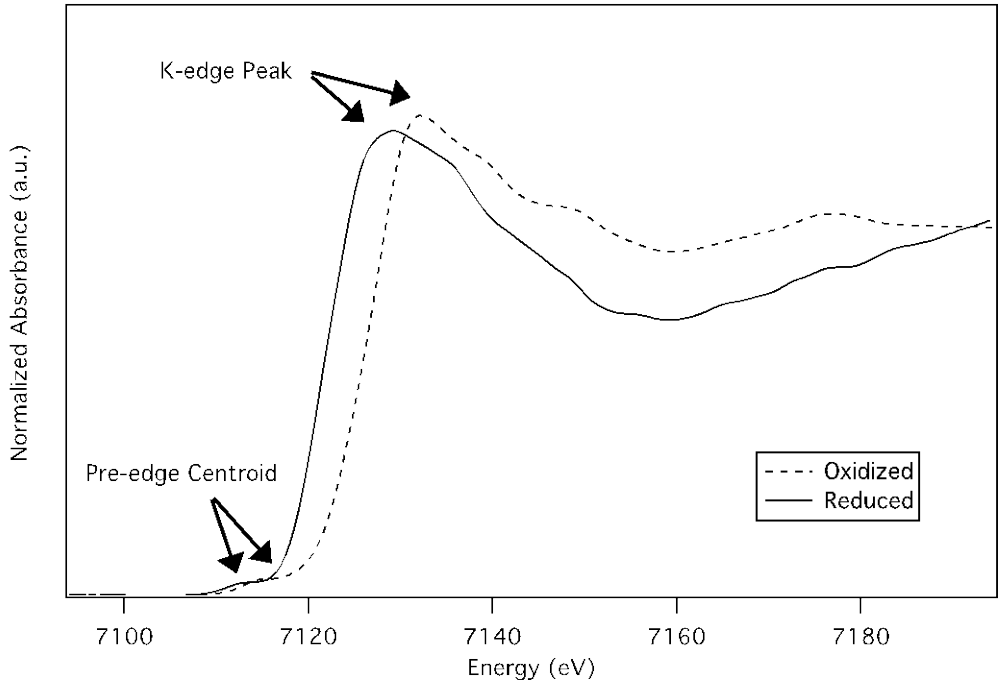

Figure 4.4. XANES spectra of an oxidized (dashed line) and reduced Fe particle (solid line)

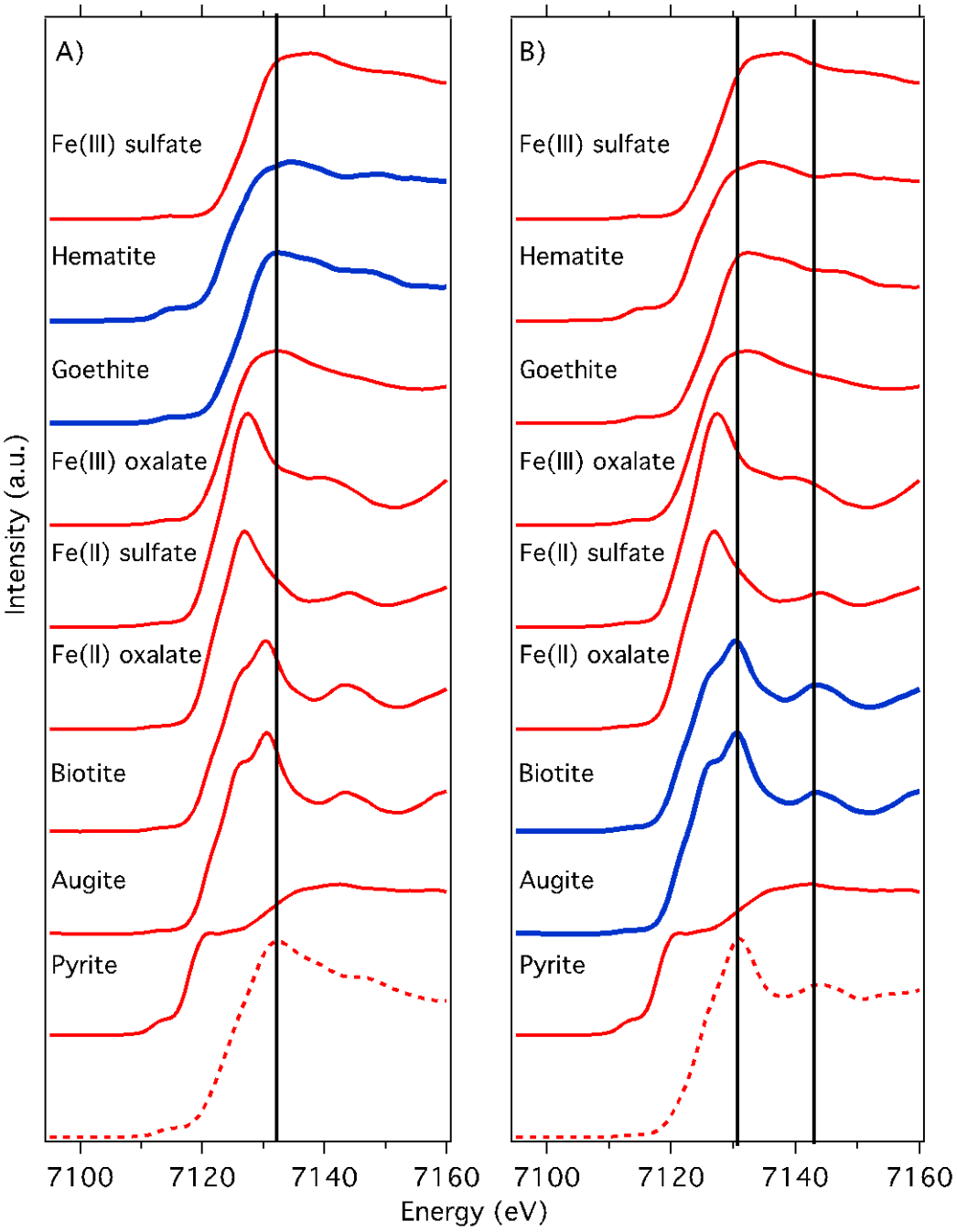

Figure 4.5. Comparison of XANES sample spectra (dashed line) to the spectra of common Fe mineral standards (solid line). Two sample XANES spectra are plotted: A) represents a typical Fe urban oxidized particle corresponding to the majority of the data and B) represents a reduced Fe particle (solid line) observed in a few particles. Fe standards shown in blue resemble the sample XANES sample spectra for A) iron oxide group and B) iron-containing aluminosilicates. The horizontal lines on the graph represent the energy where key XANES spectral features were identified.

4.2.3 Elemental Composition of Iron-Containing Particles: Insight on Mineralogy

In addition to the XANES spectra, the elemental composition determined from microscopic X-ray fluorescence measurements of each iron-containing particle was investigated to further understand iron mineralogy. The concentration of each element from aluminum to iron was converted into molar units (mol/cm^2) and compared to the iron molar concentration of each particle. Collectively, the iron data showed no strong correlation with any element (r^2<0.20) for Fe mol vs. X mol, where X represents elements from Al to Mn. However, when Fe (mol) was plotted against Al (mol) as in Figure 4.6, two elemental associations with iron emerged.

The trends indicate that iron-containing particles could be divided into two groups. The first group, comprising the majority of particles (163 out of 221, 74%) (Figure 4.6: outlined by the blue area), were low in silicon (Si molar concentration < 0.1), yet contained a relatively consistent fraction of aluminum, in a 4.9:1 Fe:Al molar ratio (r^2=0.81, $p<0.05$, e.g. within 0.05 statistical significance level). The aluminum content of these particles greatly exceeded trace aluminum levels that would be expected in pure iron oxide minerals, which ideally contain only Fe, O, and OH. Iron is commonly substituted by cations of similar size and charge, like aluminum, in iron oxide matrices, and is often observed in crustal particles (Cornell and Schwertmann, 2003). For example, aluminum-substitution observed in goethite can vary from 0-33% on a molar basis. This data coupled with the XANES spectra suggest that these particles are likely Al-substituted Fe-oxides.

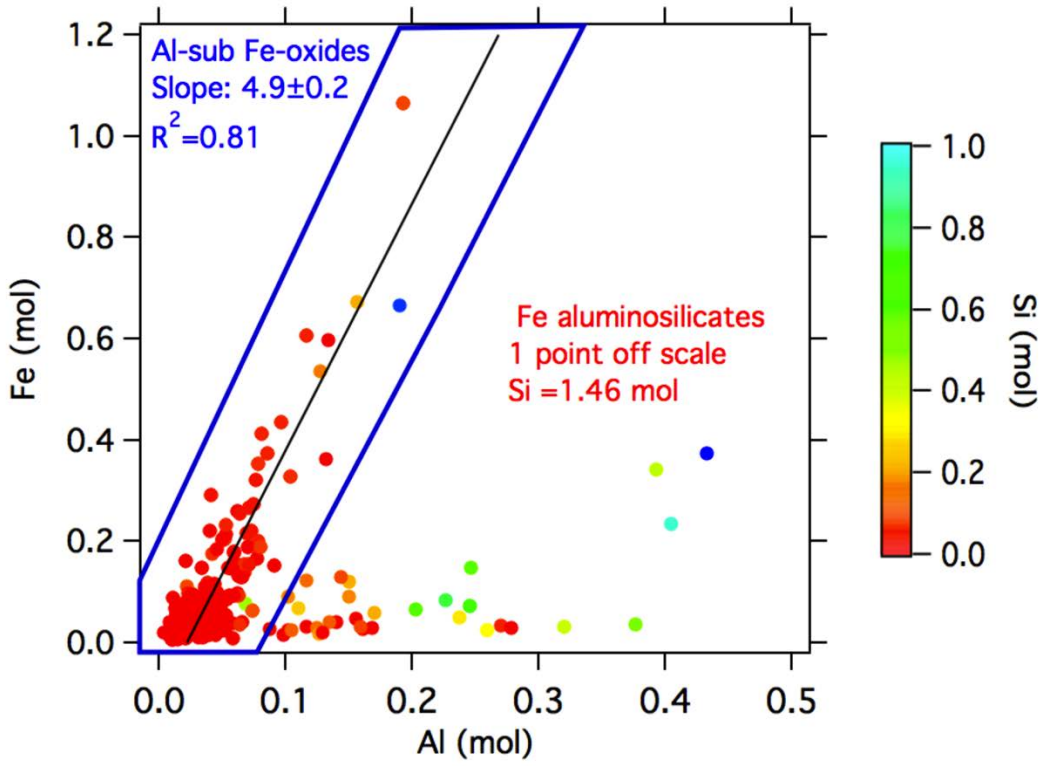

Figure 4.6. Iron and aluminum molar concentrations of iron-containing particles identified on urban and rural filters. The color scale denotes the silicon content in the particles. The blue outline represents single particles that are Al-substituted Fe-oxides.

The second group of particles (26 out of 221, 12%), shown in Figure 4.7, is characterized by lower iron concentrations and enhanced levels of silicon and aluminum relative to the first group of particles, referred to here as Fe-aluminosilicates. The silicon content of these particles strongly correlates with aluminum, with a 1.4 Si/Al molar ratio, (r^2=0.72, $p<0.05$), which compares well to Si/Al molar ratios of common aluminosilicate minerals (typically 1 to 4) [*Deer et al.*, 1978]. The XANES spectra of these particles are best matched by the spectra of common iron oxides, indicating that these particles contain a significant amount of iron in the form of oxides, which are oxidation products of Fe-aluminosilicates [*Deer*

et al., 1978]. The Si/Al molar ratio coupled with XANES spectra, which indicates iron oxide, suggests these particles are processed Fe-aluminosilicates.

4.2.4 Spatial and Seasonal Trends of Iron-Containing Particles

Figure 4.7 shows the distribution of Al-substituted Fe-oxides and processed Fe-aluminosilicates particles at urban and rural sites. Al-substituted Fe-oxides and processed Fe-aluminosilicates are observed at both urban and rural sites. For the urban sites, South DeKalb and Fort McPherson, show a mixture of both types of particles, regardless of season, while Fire Station 8 particles were exclusively associated with Al-substituted Fe-oxides for both winter and summer (Figure 4.7, with the exception of 1 point). In addition, Fort Yargo contained both types of particles during the winter, but was exclusively associated with processed Fe-aluminosilicates in the summer. Overall, the predominance of Al-substituted Fe-oxide and processed Fe-aluminosilicate particles from our samples is consistent with a bulk study of aerosols collected within an urban area in Germany over a 5-month period, where aerosols were comprised of 78% iron oxides and 22% Fe silicates [*Hoffmann et al.*, 1996]. However, our results clearly show mineralogical differences are a function of both site and season, as is the case at Fire Station 8 and Fort Yargo.

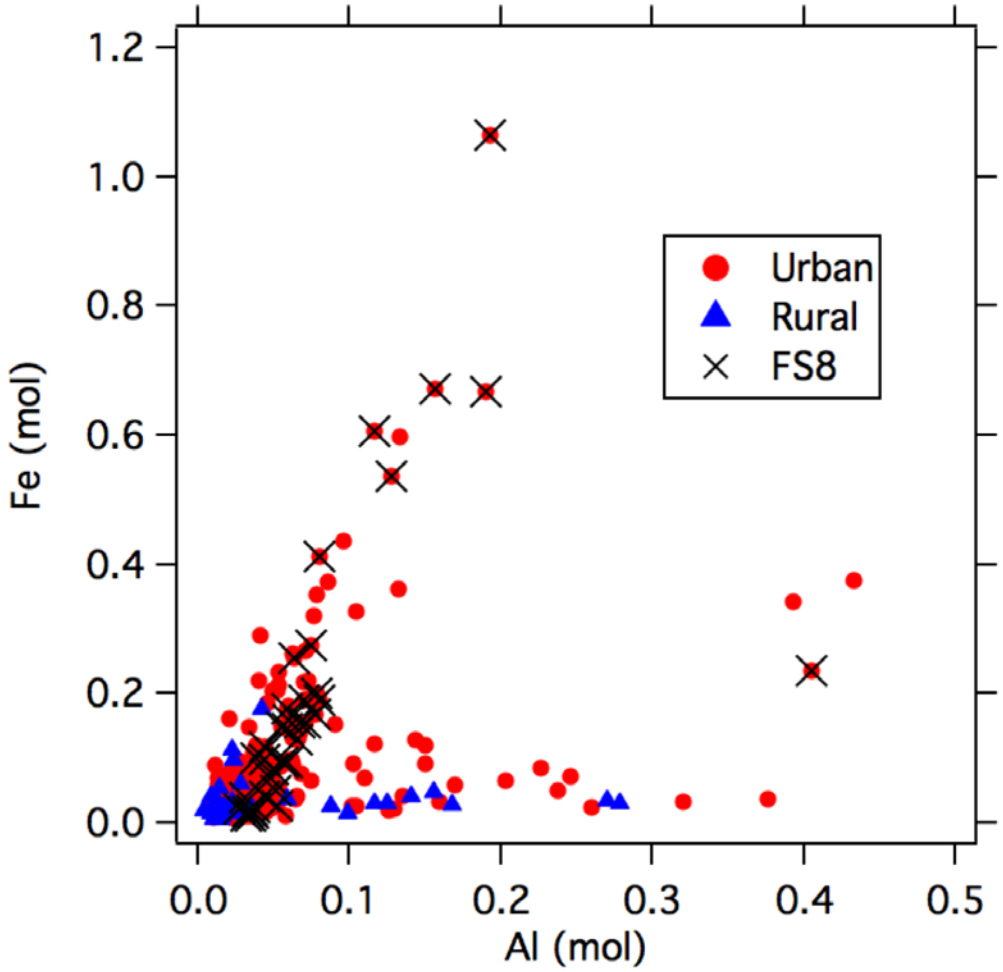

Figure 4.7. Iron and aluminum molar concentrations of iron-containing particles identified on urban and rural filters. These particles are segregated by urban (red circles), rural (blue triangles), and Fire Station 8 (black X) sites.

4.2.5 Iron Solubility: Insight on Factors Controlling Solubility

Iron solubility data were collected for all the urban and rural filters for different seasons using the ferrozine method. Results from the solubility analysis are presented in Table 4.3. A significant amount of variability was observed in urban areas, with the soluble iron concentration ranging from 3.4 to 47.9 ng/m^3, while the iron solubility at the rural site was low ranging from 4.3 to 5.8 ng/m^3. These concentrations are typical of Fe solubility in urban and rural aerosol in the

Table 4.3. Solubility Results for Urban and Rural Filters

Site	*Season*	*Soluble Fe(II)*[a] *(ng/m³)*	*Soluble Fe* [a,b] *(ng/m³)*	*Total Fe* [c] *(ng/m³)*	*N*[d]	*Total Fe(II)*[e]*/ Total Fe*	*Soluble Fe*[b]*/ Total Fe*
				Rural Sites			
Fort Yargo	Summer	2.0 ± 0.08	4.3 ± 0.17	78.0 ± 43.1	2	0.22	0.055
	Winter	4.9 ± 0.2	5.8 ± 0.23	15.4 ± 3.6	3	0.49	0.38
				Urban Sites			
Fire Station 8	Summer	4.6 ± 0.06	13.6 ± 0.18	52.6	1	0.20	0.26
	Winter	30.0 ± 1.0	49.9 ± 1.64	1734 [e]	1	0.27	0.028
Fort McPherson	Summer	4.0 ± 0.04	12.9 ± 0.14	88.1 ± 32.2	2	0.20	0.15
	Winter	6.9 ± 0.09	12.2 ± 0.16	96.5	1	0.07	0.13
South Dekalb	Summer	5.8 ± 0.1	10.8 ± 0.22	174.0 ± 86.3	2	0.05	0.062
	Winter	3.0 ± 0.06	3.4 ± 0.07	174.0 ± 39.5	3	0.16	0.020

a) Measured by ferrozine technique
b) Soluble Fe = Soluble Fe(II) + Soluble Fe(III)
c) Measured by XANES spectroscopy
d) Number of XANES elemental maps used to determine total Fe concentration
e) Measured by XANES spectroscopy, mean value of single particle oxidation state calculated for each filter
f) Outlier: Concentration is outside the standard deviation of typical total PM2.5 Fe concentration measured on filters collected in urban and rural areas in Southeastern US (seen in Table 4.3)

Midwestern US [*Majestic et al.*, 2007]. Generally, soluble iron followed total iron concentrations. For instance, the highest soluble iron concentration (47.9 ng/m^3) corresponded to the highest total iron concentration (1734 ng/m^3). To investigate solubility in relation to other variables, soluble iron concentration was normalized to total iron content to yield f iron solubility (e.g. soluble iron/total iron content). Iron solubility was between 2 and 38% (mean: 15.8 +/- 11.8 %) at individual urban and rural sites during different seasons. These iron solubility levels compare reasonably well to those found in common iron oxide (<1%) and silicate (3-6%) minerals [*Journet et al.*, 2008; *Schroth et al.*, 2009], suggesting our mineralogy data correspond well to expected fractional solubility levels.

The iron solubility was compared to a number of variables to assess their influence. No clear relationship was found between iron solubility and total iron content ($r^2=0.004$, $p>0.05$). These results are consistent with several studies, which have reported iron solubility as an inconsistent fraction of total iron, ranging anywhere between 0 to 80% of total iron [*Baker and Croot*, 2010; *Mahowald et al.*, 2005]. In addition, speciation (oxidation state and mineralogy) was also compared to iron solubility. Figure 4.8 shows iron solubility and Fe(II) content (as determined by XANES analysis) for each filter sample, indicating a moderate relationship between these two variables ($r^2=0.56$, $p> 0.05$); however, further analysis suggest this trend is not statistically robust. These results agree with *Majestic et. al.* [2007], whose results yielded no evidence for a trend between total Fe(II) and solubility in a

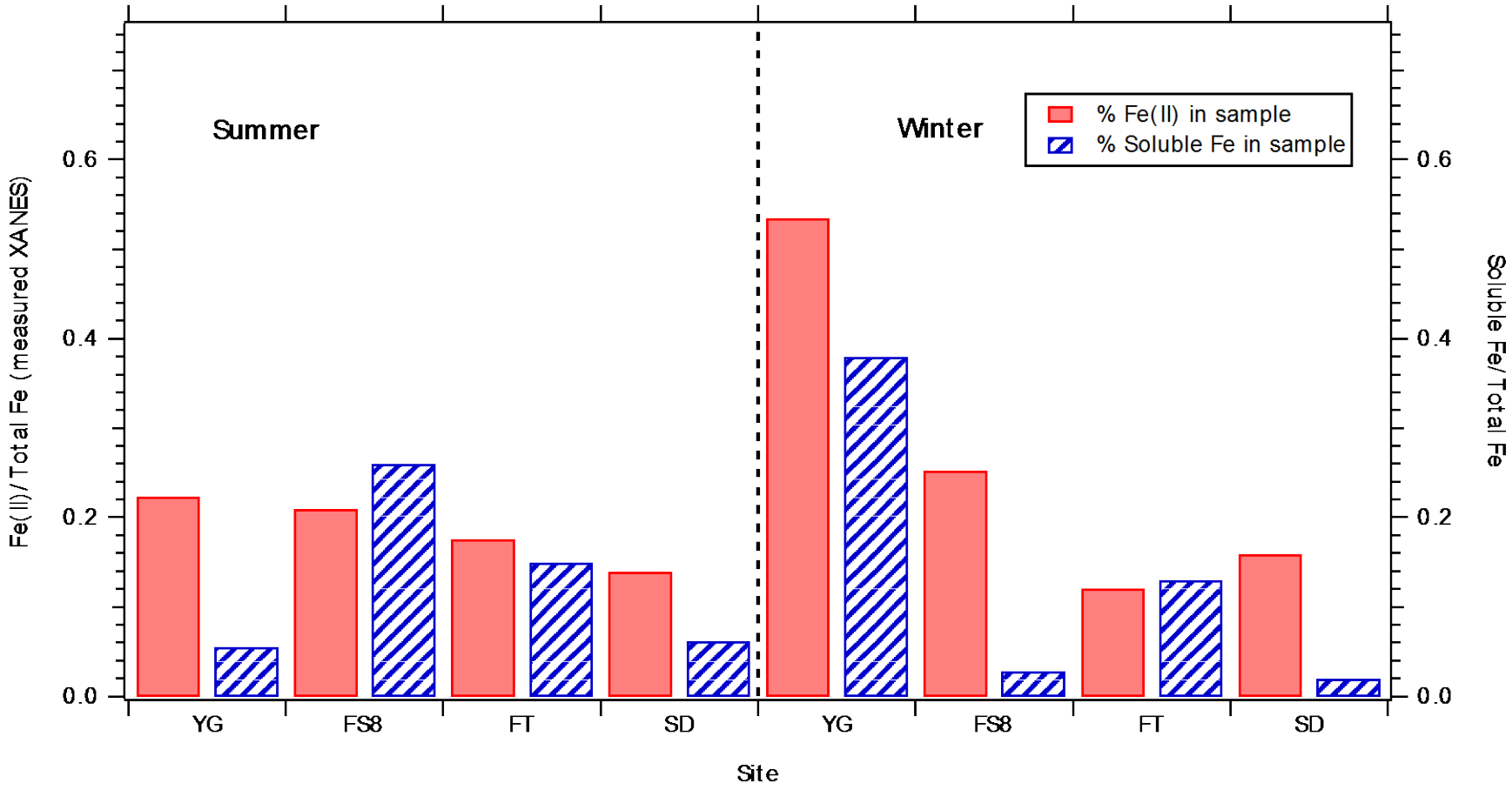

Figure 4.8. Fractional total (soluble + insoluble) Fe(II) measured by XANES (red bars) and fraction iron solubility (blue hatched bars) content in each filter sample.

number of urban aerosol samples ($r^2=0.02$, $p>0.05$, $N=11$). Furthermore, the absence of trend with speciation is more profound when iron solubility is compared among different sites. The most significant difference in the mineralogy of particles in this study was observed between Fire Station 8 site (summer and winter) and Yargo site (summer), where particles were exclusively associated with Al-substituted Fe-oxides and processed Fe-aluminosilicates, respectively. No significant difference in iron solubility was observed at these two sites, suggesting iron speciation is not the only factor influencing solubility.

Although no clear relationship between iron solubility and mineralogy was observed in this study, several laboratory experiments on iron-containing crustal and oil fly-ash particles provide evidence supporting this relationship (Journet et. al., 2008, Schroth et. al., 2009). One reason explaining the lack of trend in this study is the two dominant mineral phases observed (e.g. Al-substituted Fe-oxides and processed Fe-aluminosilicates) have similar iron solubility levels (iron oxides (< 1 %) and iron silicates (3 - 6%) [*Journet et al.*, 2008; *Schroth et al.*, 2009]. Thus, various mixtures of these two phases are not expected to yield large variations in solubility, which is the case in our data where fractional iron solubility is low and only slightly variable among different sites. A stronger association between mineralogy and solubility, however, is expected in areas where highly soluble iron minerals (e.g. iron sulfate) are the dominant source of iron in aerosols. For instance, iron oxides and silicates in crustal particles (< 6% iron solubility) are significantly less soluble than iron sulfates in oil fly ash (~80% iron solubility) [*Journet et al.*, 2008]. No iron sulfates, which are typically produced by industrial combustion,

were observed in this study. However, *Liu et. al.* [2005] showed that industrial sources comprise a small, but measureable component (< 10%) of Atlanta PM2.5. Given the limited single particle analysis used in this study, the small fraction of iron-containing particles from industrial combustion may not have been detected. This small fraction of iron sulfates may have contributed to the somewhat enhanced solubility levels observed in our data at several sites (> 6%) compared to that of pure iron oxide (< 1%) or silicate (3-6%) minerals. In addition, low levels of iron sulfates may also explain the minor differences in iron solubility levels between different sites and seasons.

Another factor possibly affecting the relationship between mineralogy and solubility in this study is that ambient aerosol may have undergone a variety of atmospheric processes altering its chemical and physical properties. As demonstrated in Chapter 3, enhancements in Fe(II) solubility were associated with acidic sulfate plumes in Georgia. Secondary sulfate is a significant portion of particle mass (~50%) in the Southeastern US [*Liu et. al.*, 2005], which can form sulfuric acid in the absence of sufficient neutralizing cations. In this study, acid-processing mechanisms may play a more central role than speciation or work synergistically with speciation to influence iron solubility. More detailed studies involving particle pH, iron speciation, and solubility are necessary to understand factors that influence iron solubility in ambient aerosols.

4.2.6 Atmospheric Implications: Insight on Human Health Toxicity

Fine aerosols that contain iron have been shown to generate toxic levels of ROS [*Shafer et al.*, 2010; Zhang et. al., 2008]. Recent experiments have related toxicity to iron oxidation state in nanoparticles (diameters smaller than 100nm). Reduced iron in nanoparticles, either present as water-soluble or crystalline Fe(0) or Fe(II), has been shown to be more efficient than Fe(III) in ROS generation [*Auffan et al.*, 2008; *Keenan et al.*, 2009]. For example, *Auffan et. al.* [2008] showed oxidation of Fe(0) and Fe(II) oxides (e.g. magnetite) immediately produce ROS, while Fe(III) oxides (e.g. maghemite) produced little to no ROS within one hour. Although particles in this study are larger (approximately 0.4-2.5 um) and presumably less reactive than nanoparticles due to less surface area per mass, the same mechanisms are likely involved in the formation of ROS via iron-mediated pathways (e.g. Fenton reactions). Thus, Fe(II) is a plausible precursor for immediate production of ROS in PM2.5. The ambient particles we investigated contained various amounts of Fe(II) and Fe(III), with the Fe(II) fraction accounting for approximately ~5 to 35% of total iron. These results indicate that a significant portion of iron-containing particles is in a redox state that can produce ROS immediately. Although Fe(II) is not always soluble in ambient aerosols (a factor strongly associated with ROS formation), particle-bound Fe(II) may interact with specific species (e.g. acidic aerosol) during atmospheric transit, promoting it's solubility.

4.3 Conclusions

We present a novel approach for exploring the speciation of iron in single atmospheric fine particles collected over urban and rural regions during different seasons using synchrotron-based XANES spectroscopy and microscopic X-ray fluorescence techniques. The majority of the particles contained mixtures of oxidized (Fe(III)) and reduced (Fe(II)) iron, with an average of 25% of the iron present as Fe(II). Particulate iron from urban and rural sites in Georgia was observed primarily in two phases, Al-substituted Fe-oxides and processed Fe-aluminosilicates. Though the composition of these aerosols was substantially different than pure minerals, it was consistent with modifications that occur during oxidation processes. Temporal and spatial variations in the oxidation state of iron and relative abundance of Al-substituted Fe-oxides and processed Fe-aluminosilicates did not coincide with the iron solubility. Solubility may be controlled by iron minerals from minor sources, for example, combustion sources of iron sulfides that were not detected by XANES as a component of overall mineralogy. In addition, other physical or chemical properties (e.g. particle acidity or size) may act in conjunction with mineralogy to influence iron solubility. These other properties may control the toxicity of iron-containing particles more than bulk mineralogy.

CHAPTER 5

IRON SOLUBILITY RELATED TO SINGLE PARTICLE SULFUR CONTENT IN SOURCE EMISSION AND AMBIENT FINE PARTICLES

Results from the previous chapter demonstrated that iron solubility was not solely controlled by solid-phase Fe(II) content or the abundance of major iron phases in samples (iron oxides vs. aluminosilicates), thus, iron speciation. This lack of relationship strongly suggests that other aerosol properties or atmospheric processes (e.g. acid-processing) primarily control iron solubility in urban and rural aerosols. Characterization of specific aerosol properties, such as particle mixing state, can provide key information on processes experienced by iron-containing particles that help to understand factors driving solubility. Furthermore, an inventory of iron solubility in different sources may help to understand what sources significantly contribute to soluble iron in aerosols. In this chapter, iron speciation and particle mixing state of single iron-containing particles in source emission and ambient PM2.5 are presented and compared to changes in iron solubility. These results help to gain a comprehensive picture of factors controlling iron solubility in aerosols.

5.1 Methods

5.1.1 Sample Collection

Five PM2.5 source emission samples including: mobile emissions (diesel and gasoline vehicle exhaust), coal-fly ash, biomass burning emissions and mineral dust. Additionally, two PM2.5 samples of ambient urban aerosol were characterized. All samples were collected on 47-mm Teflon, Zeflour or Teflo filters (Pall Corporation,

Port Washington, NY). Samples were sectioned in appropriate portions using ceramic scissors for bulk iron solubility (e.g. soluble and total iron measurements) and single particle synchrotron-based chemical property measurements (e.g. XANES and micro X-ray fluorescence). The sampling protocol for source emission and ambient PM2.5 are described in detail in the following sections.

5.1.1.1 Mobile Sources

PM2.5 in diesel engine exhaust was collected from a 10.8-L diesel engine onto Teflo filters using a source dilution sampling (SDS) system at Cummings Diesel Solutions, as described by *Liu et. al.* [2008]. The engine was fuelled by 2004 Chevron Ultra-Low Sulfur diesel fuel. The Federal Transit Protocol (FTP) driving cycle was used during sampling to represent typical urban American driving conditions [*Protection of the Environment*, 2001]. Exhaust samples from a 3.3-L gasoline spark ignition engine were collected onto Teflo filters using a chassis dynamometer and constant volume sampler (CVS) system at the E-180 facility supported by the Environmental Protection Agency. The gasoline engine was fueled by a custom gasoline blend made by Gage Products (Ferndale, Michigan), representing conventional gasoline found in a typical urban gas station. The LA92 driving cycle was used to simulate typical on-road driving conditions in urban US environments, which consists of four different driving stages. A first stage sample was used in this study.

5.1.1.2 Biomass Burning

Biomass burning samples were collected during a controlled burn experiment in Atlanta, GA. Biomass material typical of the Southeastern US,

consisting of a mix of organic material from both coniferous and deciduous trees and assorted shrubs, was used as fuel. The biomass material was dried in an oven set to 45°C 2 days prior to the burn. During the burn experiment, a filter sampler was set adjacent to and 1 m above the burn area. A cyclone inlet (URG, Chapel Hill, North Carolina) was used to select for PM2.5 and set upstream of a filter sampler. Biomass burning particles were collected onto Teflon filters (Pall Life Sciences, Port Washington, NY) for 30 minutes at a nominal flow rate of 16.7 L min^{-1}.

5.1.1.3 Coal Fly Ash and Mineral Dust

The Southern Company provided polydisperse coal fly ash particles collected from an electrostatic precipitator at Miller Coal-Fired Power Plant Unit 4 in Quinton, AL. Polydisperse mineral dust samples were collected from the native soil of Atlanta, GA, roughly 1 foot below the ground surface. The PM2.5 fraction of coal fly ash and mineral dust samples was collected onto 47-mm filters by aerosolizing the particles using an aerosol generator [*Kumar et al.*, 2011] equipped with a cyclone inlet upstream of a filter sampler.

5.1.1.4 Ambient Particles

Ambient PM2.5 was collected onto Teflon filters (47mm diameter, Pall Life Sciences) for 24 hours at a nominal flow rate of 16.7 L min^{-1} for the ongoing Assessment of Spatial Aerosol Composition in Atlanta (ASACA) field study. Winter (1/28/11) and summer (8/4/10) samples collected at the South Dekalb field site located in a mixed commercial-residential urban area, roughly ~8 km from a major interstate (I-285). More details on sample collection of these ASACA filters are provided in [*Butler et al.*, 2003]. Samples were stored in sealed polyethylene bags in

a dark freezer (~-20°C) immediately after collection and were analyzed within 6 months. Under such storage conditions iron oxidation on PM2.5 filters has been shown to be insignificant [*Majestic et al.*, 2006].

5.1.2 Bulk Iron Solubility and Synchrotron Measurements

Soluble iron was measured on a portion of each filter sample (either ½ or ¼ portions) using the ferrozine technique by Stookey et. al. (1970), specifically used to measure water-soluble Fe(II) in solution. A USB4000 portable spectrophotometer (Ocean Optics) inline with 100cm liquid waveguide capillary cell (World Precision Instruments: Sarasota, Florida, USA) was used for measurements. Detailed information on instrument calibration, sample extraction, and analysis are discussed in Chapter 4. Briefly, water-soluble PM2.5 on each filter was extracted into 10-20 ml of deionized water by 30 minutes of ultrasonication. PM2.5 extraction was followed by the removal of insoluble particles (> 0.2 um diameter) in the filter extract by a 0.2 um pore size PES (polyethersulfone) or PTFE (polytetrafluoretylene) syringe filter. Subsequently, 5 mM ferrozine solution was added in a 1:100 ratio of ferrozine reagent to sample. After precisely 10 minutes, water-soluble Fe(II) (WS_Fe(II)) was measured. Following the WS_Fe(II) measurements, a 40 uM solution of hydroxylamine hydrochloride in a 1:100 reagent to sample ratio was used to reduce WS_Fe(III) to WS_Fe(II), and a measurement was repeated again after 10 minutes. This particular measurement increment was used to minimize reduction of WS_Fe(III) by ferrozine, which can result in measurement artifacts. Overall, this method yields an operationally-defined 10-minute measurement of total water-soluble iron (e.g. Fe(II) + Fe(III)).

Total iron (water insoluble + soluble) was measured on a separate portion of each filter sample (either ½ or ¼ portions) using microwave-aided acid digestion and SF-ICPMS. The PM on this portion was microwave digested in mini-Teflon bombs (7 mL), using a mixed-acid solution, consisting of 1.0 ml of 16M nitric acid, 0.250 mL 12M hydrochloric acid, and 0.1 mL of hydrofluoric acid. Upon completion of the automated microwave program (Milestone Ethos +; 20 minute ramp to 200°C; hold 20 minutes at 200°C), the digestate was diluted to 15 ml using ultrapure water (> 18MΩ). The filter digest solution was analyzed using a magnetic-sector inductively-coupled plasma-mass spectrometer (Thermo-Finnigan Element 2), for iron (and a large suite of additional elements). Iron was quantified at m/z 56 in medium resolution (3950), resolving all spectral interferences, and confirmed at m/z 54. A series of NIST Standard Reference Materials, digested along with the samples, confirmed digestion recovery. This measurement was used in conjunction with soluble iron to yield the bulk iron solubility (soluble/total iron) for each filter sample.

Iron speciation and particle mixing state data were collected using synchrotron-based technology (e.g. X-ray Absorption Near-Edge Structure (XANES) spectroscopy and micro X-ray fluorescence measurements). These protocol for these measurements is discussed in detail in Chapter 4, sections 4.1.2 and 4.1.3.

5.2. Results and Discussion

5.2.1 Bulk Iron Solubility in Source Emission Particles

Bulk iron solubility in a variety of source emission PM2.5 is shown in Table 5.1. Significant variability in iron solubility, ranging from 0.0003% to 75%, was

observed among different sources of iron PM2.5, yielding a low and high iron solubility group. Atlanta mineral dust and coal fly ash samples comprised the low solubility group, having practically no water-soluble iron (e.g. both samples <0.01% iron solubility). In contrast, the water-soluble iron content of biomass burning and mobile samples (diesel and gasoline) was significantly higher, comprising the high iron solubility group. These differences in iron solubility were compared to a number of physical and chemical particle properties determined by synchrotron-based measurements to understand primary controls on iron solubility.

Table 5.1. Bulk Iron Solubility and Single Particle Elemental Ratios of Source Emission and Ambient Particles

Source	*Iron Solubility**	*Fe/Si***	*Fe/S***
Crustal Species	0.0009	4.0	41.2
Coal Fly Ash	0.0006	1.05	8.04
Biomass Burning	0.46	1.92	2.56
Diesel Exhaust	0.51	0.73	1.13
Gasoline Exhaust	0.75	0.41	0.63
Ambient Summer	0.22	5.82	0.33
Ambient Winter	0.09	15.33	9.59

*WS_Fe (WS_Fe(II) + WS_Fe(III))/Total iron (water-soluble + insoluble iron) based bulk iron solubility measurements

**Mean value based on single particle elemental data collected during X-ray fluorescence microscopy of multiple particles from each filter

5.2.2 Iron Speciation and Bulk Iron Solubility

It is well established that iron solubility is influenced by oxidation state and chemical composition [*Journet et al.*, 2008; *Schroth et al.*, 2009]. For instance, reduced iron (e.g. Fe(II)) is far more soluble than oxidized iron (Fe(III)) in the pH range expected in atmospheric aerosols. This leads to the expectation that particles abundant in Fe(II) should have higher iron solubility than those depleted in Fe(II). The oxidation state of single iron-containing particles in different sources was compared to bulk iron solubility to explore the relationship between these two factors. Figure 5.1 shows large variations in single particle oxidation state among different sources, ranging from 0 to 98% Fe(II) content. In general, single iron-containing particles in these sources were a complex mixture of Fe(II) and Fe(III), typically comprised of more oxidized than reduced iron (Fe(II) content: mean=28.3%, min=4.2%, and max=48.9%). Despite the significant variability observed in both oxidation state and bulk iron solubility, Fe(II) content did not consistently follow iron solubility. For example, the Fe(II) content ranged from 0% to 50% in the low solubility group (e.g. dust and coal fly ash, both <0.01% iron solubility), with dust having the lowest Fe(II) content (e.g. median Fe(II) content: 4.6) and coal fly ash having an Fe(II) content comparable to levels observed in the high solubility group (median Fe(II) content: ~36%). These results suggest that Fe(II) content in these particles is not the primary factor controlling solubility.

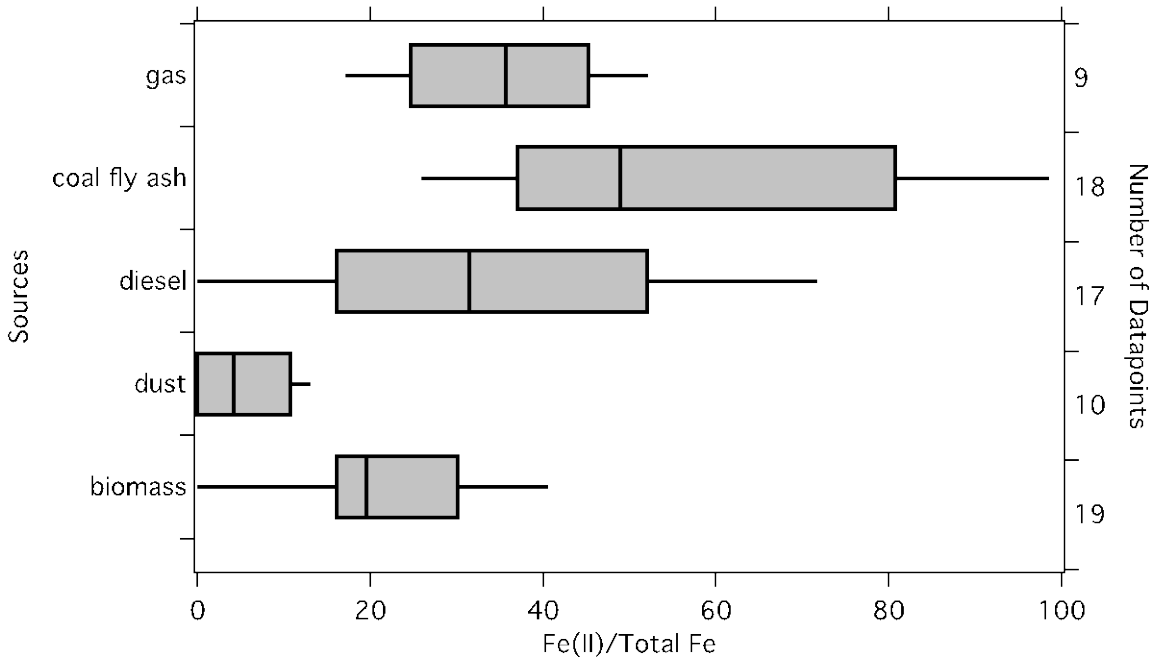

Figure 5.1 Oxidation state of single particles separated by different sources. Each box represents the 25th (bottom), 50th (middle line inside box), 75th (top) of oxidation state data in single iron-containing particles of a given source. The line above and below each box represent the 90th and 10th percentile of the data.

Along with oxidation state, differences in mineralogy can influence iron solubility. Despite their relatively low iron content, iron in alumnosilicate minerals such as feldspars and clays is much more soluble than iron bound in common iron oxide minerals such as goethite, hematite, and magnetite [*Journet et. al.*, 2008]. Molar concentrations of various elements (Al to Mn) were quantified in single iron-containing particles and were compared to iron to provide unique insight on mineralogy. Figure 5.2A shows the aluminum, silicon, and iron content in single source emission particles separated by high and low iron solubility groups. In this figure, the aluminum, silicon, and iron content in each iron-containing particle was normalized to the sum of all three components, providing the percent composition of each component. This particular approach can be used to distinguish between

iron oxides and aluminosilicate minerals. For instance, pure iron oxide particles are comprised of only Fe and O, containing 100% iron and 0% aluminum and silicate, thus, would be located in the lower left corner of the diagram. Alternatively, iron aluminosilicates contain relatively greater amounts of silicon and aluminum than iron oxides, and are located in the middle to the right hand side of the diagram. With the exception of a few particles that appear to be iron oxides in biomass burning particles, iron-containing particles in the high solubility group (e.g. red open symbols in Figure 5.2A) are abundant in iron aluminosilicates, consistent with the idea that iron aluminosilicates are generally more soluble than iron oxides. On the other hand, the low iron solubility group (e.g. closed blue symbols in Figure 5.2A) contains both iron oxides and aluminosilicates. While dust is exclusively associated with highly insoluble iron oxides, coal fly ash appears to have significant amount of iron aluminosilicates. Though coal fly ash is predominately comprised of iron aluminosilicates that are presumably more water-soluble than iron oxides, there is practically no water-soluble iron in this sample. Absence of a trend between iron solubility and the presence of iron silicates is further supported by the mean single particle Fe/Si ratios observed in source emissions (Table 5.1), which shows no clear correspondence to iron solubility. These results suggest the relative abundance of major iron-containing phases (e.g. iron silicates and oxides) do not primarily control iron solubility, which is in agreement with data presented in Chapter 4 regarding ambient aerosols.

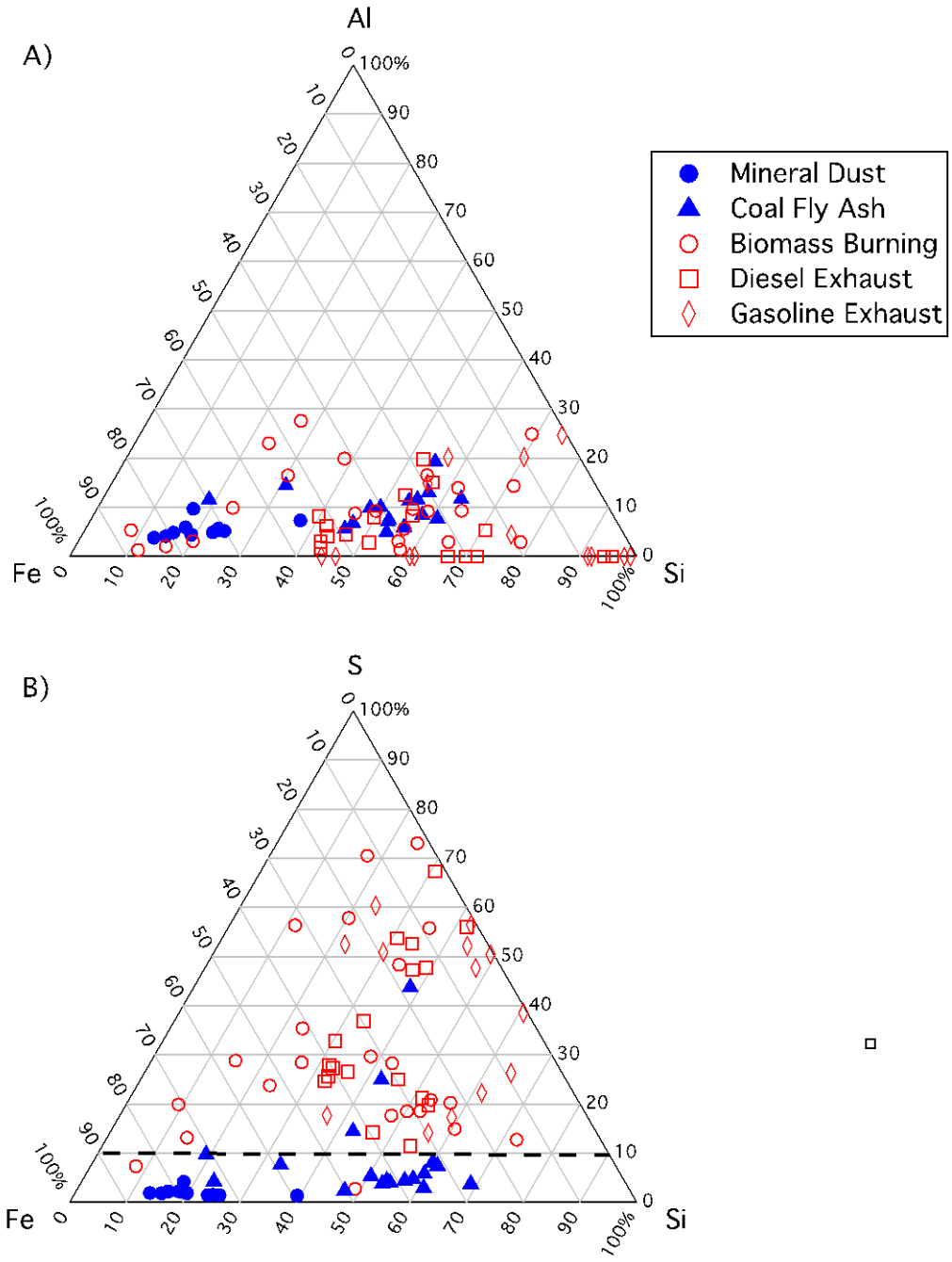

Figure 5.2. Single particle elemental data in source emission samples. A) Fe, Si, Al ratio B) Fe, Si, S ratio in source emssions are shown. The closed blue and opened red symbols represent samples with low and high iron solubility, respectively. The black dashed line represents 10% sulfur component. Particles below this line contain less than 10% sulfur content with respect to iron and silicate.

5.2.3. Single Particle Sulfur and Bulk Iron Solubility in Source Emission and Ambient PM2.5

Although no strong trend emerged with iron solubility and speciation, single particle sulfur content showed a unique trend with bulk iron solubility. The sulfur, silicon and iron content of single iron-containing particles in source emission PM2.5 are shown in figure 5.2B. Using this plot, the sulfur content of iron-containing particles, comprised of two major iron phases (iron oxides and silicates), was quantified. These results show that sources in the low solubility group (e.g. blue closed symbols) have relatively low amounts of sulfur with respect to iron and silicate, (e.g. <10% S content: Figure 5.2B, below the black dashed line) compared to sources in the high solubility group (red open symbols, >10% S content). Furthermore, mean single particle Fe/S ratios of each source emission sample show a clear decreasing trend with iron solubility (Table 5.1), supporting the trend between single particle sulfur content and bulk iron solubility.

Single particle elemental data analysis was also performed on 24-hour Teflon filters loaded with PM2.5 from an urban site in Atlanta (South Dekalb) during two seasons (winter and summer) to evaluate particle sulfur content as a primary factor controlling iron solubility in ambient urban aerosol particles. Iron solubility observed at the South Dekalb site is presented in Table 5.1, showing moderate differences between iron solubility in summer and winter samples 22% and 9% for summer and winter samples, respectively. An iron, silicate, and sulfur ternary plot for ambient data shows that the sulfur content of the high iron solubility summer samples is much higher than the sulfur content of lower iron solubility winter

particles (Figure 5.3). Similar to the source emissions, ambient iron-containing particles appear to be comprised of iron oxides and silicates (data not shown). These results are in agreement with the source emission data, suggesting that iron solubility is strongly driven by single particle sulfur content.

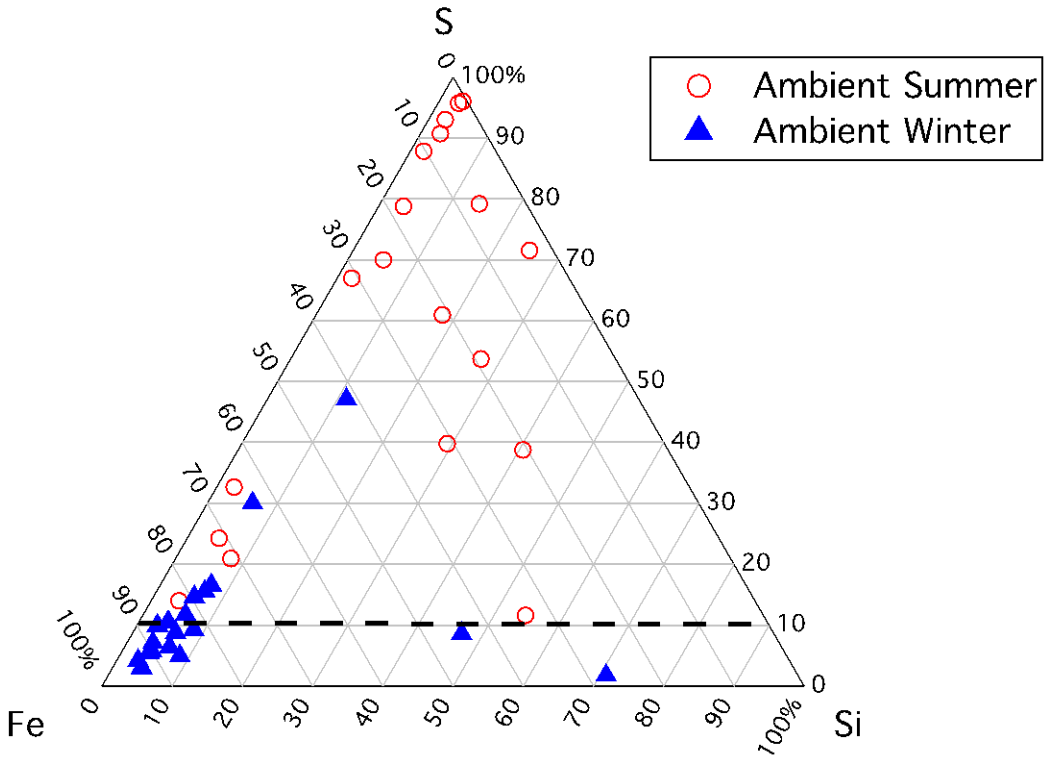

Figure 5.3. Single particle elemental data Fe, Si, S ratio. The black dashed line represents 10% sulfur component. Particles below this line contain less than 10% sulfur content with respect to iron and silicate.

5.2.4 Ambient PM2.5 Bulk Iron Solubility and Bulk Sulfate Concentration

Elemental data of single iron-containing particles has, thus far, demonstrated that bulk iron solubility is related to single particle sulfur content in a variety of urban source emission and ambient PM2.5 data. Though highly detailed single particle composition data provides unique insight into atmospheric fine particulate chemical properties, such data is often not readily available. Bulk elemental and ionic concentrations measured from 24hr-integrated filters, however, are widely available at a number of network monitoring sites and can be used to do bulk chemical analysis. Mechanisms driving iron solubility determined from synchrotron-based analyses should be consistent with trends inferred from these bulk chemical analyses.

Bulk iron solubility and bulk sulfate data from a network monitoring site in Atlanta, GA (Jefferson Street site supported by the Southeastern Aerosol Research and Characterization Study (SEARCH) [*Hansen et al.*, 2006] were compared. In this case, ICP-OES and ion chromatography techniques were used to measure bulk iron solubility (soluble iron/total iron) and sulfate from 24-hr filter samples, respectively. Sulfate was compared to bulk iron solubility since a majority of sulfur in Atlanta aerosol (as well as other regions) exists as sulfate (sulfate/S >98% based on Jefferson Street SEARCH data). Figure 5.4 shows a comparison between Fe/SO_4^{2-} and bulk iron solubility at Jefferson Street during 2004 (358 filters analyzed). A clear decreasing Fe/SO_4^{2-} trend with iron solubility is observed, which agrees well with the trend observed in source emission and ambient samples measured in Atlanta, GA.

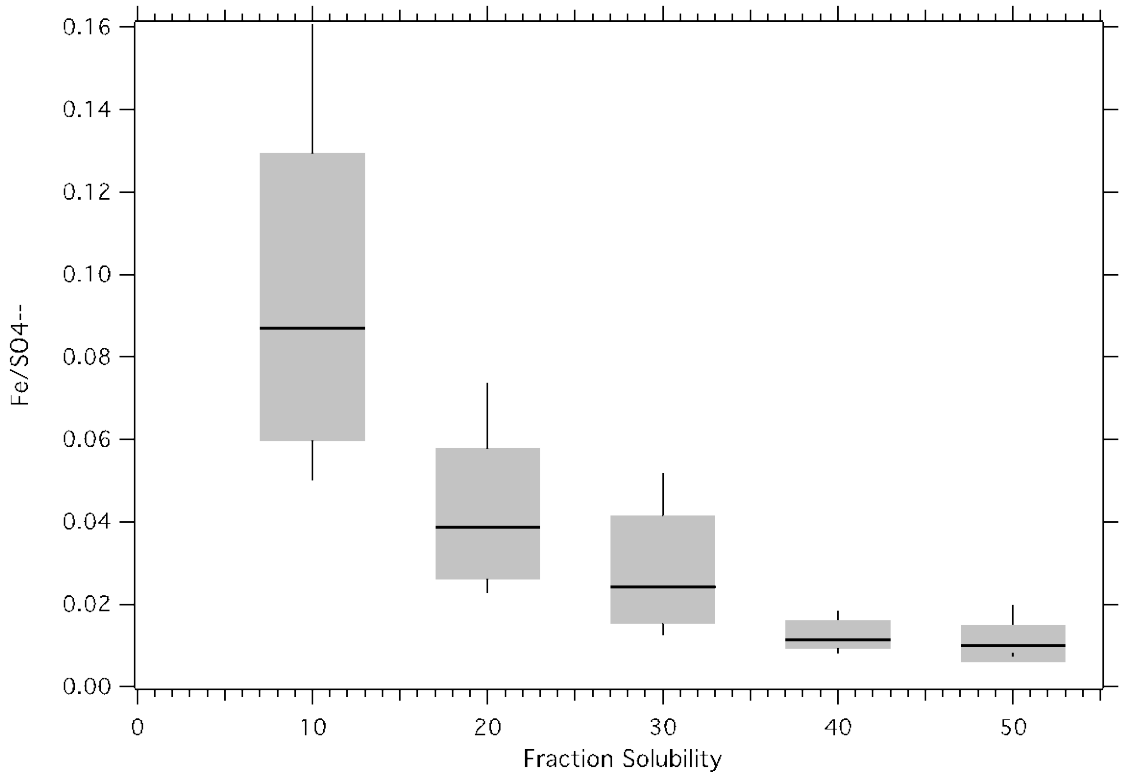

Figure 5.4. Box plot of Fe/SO_4^{2-} vs. fractional iron solubility (soluble iron/(soluble + insoluble iron) for ambient Atlanta data (SEARCH data: Jefferson Street) using 24-hour integrated Teflon filters in 2004. Bin-width for each box is 10% (e.g. box at 10% shows Fe/SO_4^{2-} data for 0-10% fractional solubility. Each box represents the 25th (bottom), 50th (middle line inside box), 75th (top) of Fe/SO_4^{2-} data for a given fractionl solubility range. The line above and below each box represent the 90th and 10th percentile of the data.

Acid-processing mechanisms can explain the correlation between single particle sulfur, as sulfate, and bulk iron solubility observed in this study. For instance, sulfate, formed by SO_2 oxidation, can ultimately form an acidic deliquescent layer on an iron-containing particle in the absence of sufficient neutralizing cations, such as ammonium. In an acidic aerosol solution, mobilization of Fe(II) and Fe(III) is thermodynamically favored compared to circum-neutral pH environments. This particular mechanism is hypothesized to be more important in urban regions where SO_2 emissions are abundant. In this study, aerosol pH is

expected to vary from highly acidic (pH~0) to circum-neutral (pH~7.5), based on thermodynamic model predictions (ISORROPIA-II, [*Fountoukis and Nenes*, 2007]) using typical concentrations of two major inorganic aerosol components observed in Atlanta (NH_4^+, SO_4^{2-}). In this pH range, large variations in iron solubility are expected indicating that atmospheric acid-processing by H_2SO_4 is a viable option for the dissolution of iron in this study.

These acid-processing mechanisms may be linked to the presence of highly soluble iron sulfates in PM2.5, which have been shown to control iron solubility in oil fly ash [*Schroth et al.*, 2009]. For example, changes in iron mineralogy that increase solubility can occur as a result of significant pH variations [*Shi et al.*, 2009], which may be the case here. It is possible that iron sulfates formed in a wet aerosol rich in soluble iron and sulfate ions as a consequence of acid-processing mechanisms by H_2SO_4. This idea is consistent with linear combination fits of sample XANES spectra with standard Fe minerals (data not shown), showing iron sulfates were present in some ambient iron-containing particles. Similar mechanisms (e.g. acid-processing and formation of iron sulfates) may occur in source emissions on a more rapid timescale. Though the synergistic effort of acid-processing mechanisms and the presence of iron sulfates can explain iron solubility in this study, additional studies are necessary to confirm the exact relationship between these two factors. Overall, our results demonstrate, the importance of acid processing mechanism by H_2SO_4 (aerosol pH) on bulk iron solubility in ambient urban particles.

5.3 Conclusions

Analysis of single iron-containing particles combined with bulk iron solubility measurements in a variety of source emission material and ambient air provided unique insight to factors controlling iron solubility. Although iron speciation (e.g. oxidation state and mineralogy) has been shown to greatly influence solubility in earlier studies [*Cweirtny et. al.*, 2008; *Journet et al.*, 2008; *Schroth et al.*, 2009], no clear association between iron solubility and the relative abundance of reduced iron and major iron phases (e.g. iron oxides and silicates) was observed in either the sources tested or ambient particles, consistent with results presented in Chapter 4. Instead, elemental data of single iron-containing particles revealed a unique correspondence between single particle sulfur content and bulk iron solubility on filter samples. A similar correspondence was observed in ambient iron-containing particles collected from urban aerosols in Atlanta, suggesting the same mechanisms control fractional iron solubility in both source and ambient particles. An analysis based on bulk filter data for ambient Atlanta aerosols show that decreasing Fe/SO_4^{2-} corresponds to increasing iron solubility. These results clearly support the idea that single particle sulfate content, most likely associated with acid-processing mechanisms, is the primary control factor of iron solubility in urban source material and ambient PM2.5. These acid-processing mechanisms may play an important role in the health impacts associated with the water-soluble fraction of iron in aerosols.

CHAPTER 6

FUTURE WORK

Overall, the results of this thesis have improved our understanding of iron solubility in atmospheric aerosols; however, they have revealed additional research needs. As part of this thesis, a semi-continuous measurement technique (PILS-LWCC) was developed that proved to be resourceful in characterizing sources, atmospheric processes, and temporal variability of WS_Fe(II). However, comparison between merged PILS-LWCC and filter-based WS_Fe(II) data demonstrated the presence of sampling artifacts in both techniques due to particle collection, sample treatment and storage. It is necessary to determine the source of these artifacts and develop a plan to minimize them in order to provide more reliable measurements of WS_Fe(II). A detailed side-by-side comparison of PILS and filter-based measurements for an extended period of time is recommended. This particular experiment should be designed such that potential sources of artifacts can be tested, including: 1) sample collection technique (PILS vs. filter-based collection techniques), 2) storage methods (immediate sample extraction vs. month to weeklong sample storage), and 3) analytical mixing (automated vs. manual mixing). Initial experiments have already been undertaken and are outlined in Appendix A.1. These experiments will be extremely useful in assessing the reliability of these techniques.

Although the PILS-LWCC marks large strides in development of instrumentation capable of iron speciation in high time resolution, there are several

improvements that could be made to have a low maintenance system capable of field-deployment with minimal supervision. A few of these modifications have already been undertaken and are discussed in detail in Appendix A. These improvements include adapting to continuous flow system and 2) measuring both total soluble (WS_Fe(II) + WS_Fe(III)) and ferrous iron (WS_Fe(II)). Continued instrument development of this continuous-flow prototype (CF-PILS-LWCC) with special attention to integrating a routine cleaning cycle is recommended. During the development, an extended intercomparison of filter and PILS data is also required. If the CF-PILS-LWCC cannot provide relatively good comparisons with filter-based measurements over an extended period of time (as is the case in the initial experiments), the semi-continuous system (PILS-LWCC) should be used.

Once a fully-functional low maintenance instrument is developed and appropriately validated, it should be deployed in the field alongside a host of online instrumentation. Several sources and processes leading to transient events remained unidentified in this thesis due to a lack of adequate ancillary data. Deployment of the PILS-LWCC or CF-PILS-LWCC alongside other additional online instruments, such as the EC/OC instrument, meteorological instruments, SO_2 analyzer, PILS-IC, PILS-TOC, is suggested. These experiments may provide the critical data necessary to identify these unknown sources and formation mechanisms associated with iron solubility. Another experiment that may be interesting is simultaneous measurements of WS_Fe (WS_Fe(II) + WS_Fe(III), WS_Fe(II), and ROS in areas iron-rich high areas such as Birmingham, AL. A comprehensive dataset elucidating the controls of iron aerosol solubility at this site

would also be interesting. These combined measurements would yield valuable information on formation processes of particle-bound ROS and also provide critical information to assess redox cycling and iron solubility in aerosols.

Finally, acid-processing has been identified as an important mechanism promoting iron solubility in atmospheric aerosols. Previous studies have indicated that various iron phases (oxides vs. silicates) respond differently to specific secondary acidic species (H_2SO_4 vs. HNO_3) [*Cwiertny et al.*, 2008]. In this dissertation, iron solubility was only explored in SO_4^{2-} dominated regions, where sulfuric acid is expected to comprise the majority of secondary acidic aerosol mass. Evaluating the importance of acid-processing mechanisms in a NO_3^- or Cl^- dominated regions, where HNO_3 and HCl are the dominant acidic species, respectively, would help to further understand the importance of these acid-processing mechanisms. In particular, a similar single particle and bulk iron solubility analysis in these areas may provide critical field evidence to support laboratory findings on iron solubility controls.

CHAPTER 7

CONCLUSIONS

Water-soluble iron is an important component in atmospheric aerosols, influencing human health and global climate change. The soluble portion of iron (iron solubility: soluble iron/total iron) in aerosols, however, is significantly variable (0.01-80%) and difficult to estimate based on our limited understanding of it's sources and atmospheric formation processes. Detailed field and laboratory measurements that provide information on soluble iron temporal variability, sources, and formation processes are essential to evaluating it's impact on public health and the environment. The work in this thesis addresses this critical research need by using a synergistic measurement approach to characterize iron solubility in urban and rural regions as well as source emissions.

The first part of this thesis describes the development and validation of instrumentation capable of measuring WS_Fe(II) in 12 minute integrals, referred to as the PILS-LWCC. The LOD determined for the PILS-LWCC was 4.6 +/- ng m^{-3}, with a 12% measurement uncertainty, making it well-suited for WS_Fe(II) measurements in urban regions. In general, the PILS-LWCC measurements compared well to WS_Fe(II) determined from conventional filter-based methods (r2=0.71, slope=0.84±0.1). Moderate deviation between PILS and filter-based WS_Fe(II) measurements indicated the presence of artifacts potentially associated with particle collection, sampling technique, storage conditions, and details associated with the analytical method. Overall, the PILS-LWCC is the first prototype of semi-continuous instrumentation with the ability to quantify WS_Fe(II) in aerosols. This

instrument greatly improved measurement time-resolution from techniques traditionally used to characterize WS_Fe(II) aerosols (e.g. filter-based), allowing for a more comprehensive picture of WS_Fe(II) temporal variability, sources and atmospheric formation processes.

The PILS-LWCC was deployed at two urban sites (Atlanta, GA and Dearborn, MI) and a prescribed biomass burning event in South Georgia, USA to characterize WS_Fe(II) aerosols. Significant temporal variability was observed at both urban sites, with concentrations ranging from the LOD to 400 ng m^{-3}. Although WS_Fe(II) showed substantial temporal variability during a 24-hour period at all urban sites, no significant increase in WS_Fe(II) was observed during daytime hours when there is maximum solar radiation. These results suggested that photo-reductive processes likely do not contribute to a measurable increases in WS_Fe(II). In addition to diurnal variability, seasonal variability observed in Atlanta, GA showed unique findings. For instance, semi-continuous WS_Fe(II) measurements in Atlanta, GA typically were the lowest in the summer, which is in contrast to the increasing seasonal trend in total soluble iron (WS_Fe(II) + WS_Fe(III)) observed in archived filter measurements from a similar location in Atlanta. These results suggest that WS_Fe(II) may largely be oxidized to WS_Fe(III) during the summers, which has potential implications on the environmental fate of iron, since WS_Fe(II) is generally considered more important than WS_Fe(III) for ROS formation.

During several field measurements, transient WS_Fe(II) events lasting 1-2 hours were observed, where WS_Fe(II) concentrations drastically increased between 50 to 100s of ng m^{-3} above the observed regional background (~10 ng m^{-3}).

WS_Fe(II) transient events at the Fire Station 8 site in Atlanta, GA generally occurred late in the evening (20:00 and 22:00) during times of low wind speed, suggesting a local influence. They generally tracked well with an increase in ultrafine particles, but not overall PM2.5 mass. Due to the clockwork nature of these events and observed increases in ultrafine particle fraction, they appeared be associated with a unique iron-rich, combustion-related activity, but the specific source was not identified. Several additional WS_Fe(II) transient events were observed in Atlanta, GA (Jefferson Street) during the summer (August 2008). These events were associated with mid-afternoon (12:00 to 3:00pm) increases in SO_4^{2-} (r2=0.76, N=17) and apparent particle acidity ($SO_4^{2-}+NO_3^-/NH_4^+$) (r2=0.78, N=17), presumably associated with coal-fired power plants [*Weber and al.*, 2003]. However, the lack of correlation between SO_2 and WS_Fe(II) (r2=0.23, N=17) during these events indicated that WS_Fe(II) was likely not directly emitted from coal-fired power plants. The association between WS_Fe(II) transient events, SO_4^{2-}, and particle acidity point to acid-processing by sulfuric acid as a source for WS_Fe(II) aerosols.

In addition to these findings, no strong relationship was observed between WS_Fe(II) and EC in urban areas, where biomass burning has minimal impact on air quality (Dearborn, MI and Atlanta, GA). These results suggest that typical urban combustion sources (e.g. mobile sources) may not directly emit soluble iron. Finally, a strong correlation (r2= 0.88, N=17) between online measurements of WS_Fe(II) and WS_K+ during a prescribed burn demonstrated that biomass burning is a source of WS_Fe(II). Overall, PILS-LWCC measurements results revealed several

sources for WS_Fe(II) in urban atmospheric aerosols: 1) industrial activity, 2) acid-processing mechanisms involving secondary acidic species (e.g. H_2SO_4) and 2) biomass burning emissions.

To understand the role of other factors (chemical speciation) influencing iron solubility that could not be directly tested using online measurements, advanced synchrotron-based techniques were used, specifically XANES and micro X-ray fluorescence. Employing these techniques, speciation (oxidation state and chemical composition) of single iron-containing particles deposited on 24-hour Teflon filters in urban (Atlanta, GA) and rural (near Atlanta, GA) regions were characterized. These results were compared to bulk iron solubility measurements to determine the importance of chemical speciation on iron solubility. A wide range of Fe(II) oxidation state (0-100%) was observed in single iron-containing particles from urban and rural samples, showing a median Fe(II) content around 25%. These results indicated that these particle were a complex mixture of Fe(II) and Fe(III), with a majority of the particle as Fe(III). Combined XANES spectra and micro X-ray fluorescence measurements of ambient particles showed the presence of two major iron phases (Al-substituted Fe oxides or Fe-aluminosilicates) that were significantly modified from pure iron oxides or aluminosilicates minerals. Bulk iron solubility did not correspond to changes in iron major iron phases or oxidation state, suggesting that other aerosol properties or atmospheric processes (e.g. acidic processing) are more important than bulk speciation for iron solubility in ambient aerosols.

Additional synchrotron-based studies were performed on source emission and ambient urban aerosols (Atlanta, GA) to further understand the aerosol properties and atmospheric processes driving iron solubility. Source emission samples included a variety of anthropogenic (mobile exhaust: gas and diesel, coal fly ash) and natural (mineral dust and biomass burning emission) sources. Large differences in bulk iron solubility in source emission were observed, ranging from sources with practically no soluble content (<1%, coal fly ash and mineral dust) to those with very high soluble content (75%, mobile exhaust and biomass burning). The abundance of major iron phases and solid-phase Fe(II) content in source emissions could not describe the variability in iron solubility alone, consistent with the results previously determined. Single particle sulfur content, however, showed a unique increasing trend with bulk iron solubility. This trend was further supported by a decreasing trend between single particle Fe/S content and iron solubility. Ambient fine particles on Teflon filters collected in Atlanta, GA showed a similar trend between bulk iron solubility and single particles sulfur content, indicating the similar aerosol properties or processes in these samples primarily control iron solubility. In addition to single particle analysis, a decreasing trend between bulk iron solubility and bulk Fe/SO_4^{2-} from archived filter samples collected in Atlanta, GA supported this trend. These results suggest that iron solubility in source emission and urban fine particles is linked to single particle sulfur content, as sulfate aerosols.

Combining the results of this thesis reveal that iron solubility in urban and source emission aerosols is closely related to the abundance of sulfate aerosol. This

relationship is likely due to the importance of acid-processing mechanisms involving H_2SO_4 on iron solubility, which is supported by the semi-continuous, archived filter, and single particle measurement data presented in this thesis. This finding is consistent with a growing body of laboratory and modeling studies showing the importance of acid processing mechanism on iron solubility in atmospheric aerosols. Acid processing may also be linked to the formation of highly soluble iron sulfates through a series of pH cycling. A few recent studies have already demonstrated the formation of more soluble iron nanoparticles as ferrihydrite in Asian dust due to similar acid-processing mechanisms [Shi et. al., 2009; *Takahashi et al.*, 2011]. Though the exact mechanism involving SO_4^{2-} cannot be determined, the interactions between sulfate and iron is undoubtedly important for iron solubility in urban atmospheric aerosols and source emissions. The presence of sulfate aerosol may ultimately play an important role in predicting toxicity and bioavailability of urban iron aerosols.

In addition, these thesis results call into question the importance of other underlying factors contributing to aerosol iron solubility. While previous studies have demonstrated various aerosol properties (e.g. major iron phases and oxidation state) and atmospheric processes (e.g. photo-reductive processes) promote iron solubility, the results presented here suggest their influence is negligible.

Another confounding finding is the lack of correlation observed between EC and WS_Fe(II) in our urban semi-continuous measurements, suggesting that diesel combustion sources likely do not contribute to WS_Fe(II). Although this initially seems to contradict with our single particle measurements (showing iron solubility

is high in mobile exhaust sources), it seems as though sulfur emissions from mobile exhaust control solubility instead of the emission itself. Though there is still much more to learn on factors that control iron solubility, the results have significantly contributed to the current state of knowledge on iron solubility.

APPENDIX A

MODIFICATIONS TO THE PILS-LWCC: DEVELOPMENT OF THE CONTINUOUS FLOW PILS-LWCC (CF-PILS-LWCC)

During the course of instrument development and validation of the PILS-LWCC, a number of problems were identified. In many cases, these problems contributed to significant measurement interferences and challenges to operating the instrument autonomously. These problems motivated the optimization of the original PILS-LWCC, leading to a series of changes improving autonomous operation. The design and performance of the latest version of PILS-LWCC, referred to as the continuous flow-PILS-LWCC (CF-PILS-LWCC) are described in this appendix chapter. In addition, several recommendations for further optimization of CF-PILS-LWCC are outlined in the conclusion of this appendix.

A.1 Motivation for the Development of CF-PILS-LWCC

A.1.1 Need for Continuous Flow System

The original PILS-LWCC was designed as a collection vial, batch-analytical system. Unlike other PILS integrated continuous measurement methods (e.g. PILS-IC or PILS-TOC), the PILS-LWCC required a relatively high sample flow rate of 1 ml min^{-1} through the LWCC to maintain a stable baseline, thus, a reliable measurement. In order to operate at this sample flow rate without significantly diluting the sample, a batch-analytical system was required. In this system, approximately 1.0 ml of aerosol sample from the PILS was collected into a vial over a period of 10 minutes. This batch sample was then removed from the collection vial and directed to the

LWCC for WS_Fe(II) analysis. One major drawback to this system was sample accumulation in the vial over time. This drawback resulted from inefficient sample removal from the collection vial due to the inability to accurately control flows into and out of the collection vial, highlighting the challenges in using a collection-vial based system for measurements.

Another major drawback to the batch-analytical system was significant baseline noise caused by air bubbles clinging to the LWCC walls. A large air bubble was introduced before and after each batch sample to separate it from the de-ionized rinse cycles and remove small bubbles from the LWCC. In general, this method successfully kept air bubbles from entering the LWCC for short periods of operation (1-2 days maximum). However, after extended periods, these air bubbles caused significant measurement inaccuracies associated with baseline noise. Substantial sample accumulation and baseline variability made it difficult to operate the PILS-LWCC autonomously, indicating the need for an improved prototype.

To avoid drawbacks associated with the batch-analytical system (e.g. sample accumulation and baseline variability), a second version of the PILS-LWCC was developed, utilizing a non-gas-segmented continuous sample flow. Like the original prototype (PILS-LWCC), the liquid sample flow rate from the PILS in continuous flow-PILS-LWCC (CF-PILS-LWCC) was 0.12 ml min^{-1}, a flow rate much lower than what is typically employed in the LWCC (1 ml min^{-1}) to avoid measurement interference from air bubbles. In order to produce a bubble-free sample while maintaining a relatively low flow rate in the LWCC, a glass debubbler (internal volume < 0.5 mL) and a Teflon degasser inside a Sievers 900 Inorganic Carbon

Remover (Sievers, Boulder, Colorado: internal volume < 1 mL) was placed downstream of the PILS and upstream of the LWCC, respectively to remove air bubbles resulting from the gas-segmented PILS sample flow. The chemical trap upstream of the degasser was removed and stainless steel fittings were replaced with Teflon fittings to adapt the degasser for soluble iron measurements,. The addition of the debubbler and degasser resulted in the removal of the majority of air bubbles, while causing minimal measurement interferences, and requiring little sample volume. Thus, they were easy to integrate into the CF-PILS-LWCC.

A.1.2 Need for WS_Fe measurements

Although reduced iron (e.g. WS_Fe(II)) is more soluble in the pH range expected in the atmosphere, a significant fraction of soluble iron (40-50%) in aerosols (filtered 0.2 um pore size) exist as Fe(III) (e.g. WS_Fe(III); soluble Fe(III)) [*Majestic et. al.*, 2006]. Aerosol WS_Fe(III) is a precursor to toxic species, forming ROS over extended periods of time. Furthermore, understanding the redox cycling of iron in the atmosphere can help identify dominant sources and processes contributing to iron solubility. In order to improve our understanding of soluble iron in aerosols, the CF-PILS-LWCC was designed to measure both WS_Fe(II) and WS_Fe (WS_Fe(II) + WS_Fe(III)). The WS_Fe measurement was achieved by adding a reducing agent along with ferrozine to the sample. In particular, the WS_Fe(III) fraction in the sample is reduced to WS_Fe(II) in order to analyze it using the ferrozine technique, which is specific for WS_Fe(II) detection.

A.2 Methods

A.2.1 Reagents and Standards

Reagents and standards used for CF-PILS-LWCC calibration and operation were prepared in acid-cleaned amber or clear polyethylene bottles. An acidified (pH 1 by HCl) 1000 mg Fe(II) L^{-1} stock solution was prepared by adding 0.702g ammonium iron(II) sulfate hexahydrate (Sigma-Aldrich, St. Louis, MO) to 10g of ultra-pure water (>18MΩ) gravimetrically. Working Fe(II) standards ranging from 1 to 20 μg L^{-1} for CF-PILS-LWCC calibration were prepared in a similar fashion as for the PILS-LWCC. A 5mM ferrozine solution was prepared every other day by adding 0.255 g of ferrozine (3-(2-pyridyl)-5,6-diphenyl-1,2,4-triazine-4-4'-disufonic acid, Sigma-Aldrich, St. Louis, MO) to 100ml of ultra-pure water. Although Brij-35 surfactant was used extensively in the PILS-LWCC to minimize large backpressures caused by air bubbles entering the system, it was determined to have no effects on sample flow, thus, was not used in the ferrozine solution. A reductant was the only new reagent required to reduce WS_Fe(III) to WS_Fe(II) for WS_Fe analysis. This solution was prepared every other day by dissolving 40 mg of hydroxylamine hydrochloride (HA) into 50 mg of deionized water, measured gravimetrically. All stock solutions and reagents were stored in a dark refrigerator (4°C).

A.2.2 Overview of the CF-PILS-LWCC

Figure A.1 shows a schematic of the modified PILS-LWCC, the CF-PILS-LWCC. The integrated system includes: a PM2.5 cyclone, a PILS, 2-multi-channel peristaltic pumps, 2 mutli-port valves, gas-removal devices, mixing coils, a LWCC, and a USB-400 spectrophotometer. For the most part, the PILS collection system in the CF-PILS-LWCC is similar to that used in the original PILS-LWCC. For instance, a PM2.5 cyclone was used as an inlet, selecting for particles with aerodynamic diameters less

than 2.5μm, and an 8-channel peristaltic pump was used to control the PILS liquid flows (e.g. steam, waste, and impaction plate flows). Extra channel lines, however, were added to the PILS operation peristaltic pump for analytical reagents (e.g. ferrozine and HA.

The most significant difference between the two versions of system lie in the liquid handling system, outlined in blue in figure A.1. In the original PILS-LWCC prototype, a second peristaltic pump (separate from PILS operation peristaltic pump) controlled liquid handling system flows. In contrast, the PILS operation peristaltic pump controls the majority of flows for the CF-PILS-LWCC liquid handling system. However, a second peristaltic pump was still required for the DI rinse cycle in between samples in the CF-PILS-LWCC. In addition to minor modifications to the liquid pumping in the CF-PILS-LWCC, an additional valve was employed to direct HA to the liquid handling system (for WS_Fe measurements) or to waste (for WS_Fe(II) measurements). Other additions to the CF-PILS-LWCC liquid handling include the debubbler and degasser (Sievers, IC) to remove large and micro bubbles from entering the LWCC.

A.2.3. Overview of the CF-PILS-LWCC Liquid Handling System

The liquid handling system of the CF-PILS-LWCC is highlighted in blue in Figure A.1. This portion of the CF-PILS-LWCC controlled the analytical mixing of sample with reagents, and ultimately directed the sample to the LWCC for detection by the spectrophotometer. In the CF-PILS-LWCC liquid handling system, the PILS provided a gas-segmented continuous sample flow to the liquid handling system at a flow rate of 0.12 ml min^{-1}, similar to the flow used in the original PILS-LWCC. The

gas-segmented sample was subsequently passed through a debubbler, removing large air bubbles from the flow, then transported to a tee, combining sample with ferrozine reagent. This mixed sample (e.g. aerosol sample + ferrozine) was then directed to a serpentine reactor (Global FIA, Washington) for further mixing of WS_Fe(II) in aerosols with ferrozine. After 12 minutes of continuous sample flow, a computer-controlled valve connected to the PILS outflow line and a de-ionized (DI) water supply was switched, effectively directing the sample flow to waste and DI flow to the sample line. During this time, the deionized water was purged through the system (2 ml min^{-1}) using the second peristaltic pump in order to push the mixed sample and subsequent rinse cycle rapidly through the sample line. As the mixed sample entered the LWCC, the flow was paused, and an absorbance measurement at 562 nm (maximum absorbance of WS_Fe(II)-ferrozine complex) and 700 nm (baseline absorbance) was collected. The difference between 562 nm and 700 nm was used to determine the WS_Fe(II) in the sample. After one minute of WS_Fe(II) measurement, the computer-controlled valve was switched back to the PILS sample flow. In addition, a second valve connected to the HA supply was simultaneously switched, directing HA to the sample line. The addition of HA to the sample allowed for the reduction of WS_Fe(III) in the sample, thus, providing a method to measure total WS_Fe (WS_Fe(II) + WS_Fe(III)) by the ferrozine technique. The same liquid pumping/mixing procedure used to analyze WS_Fe(II) in the CF-PILS-LWCC was used to analyze WS_Fe. Therefore, the CF-PILS-LWCC yielded a 12-minute continuous measurement of WS_Fe(II), followed by a DI cleaning cycle then

a 12-minute continuous measurement of WS_Fe, allowing for the speciation of soluble iron in PM2.5.

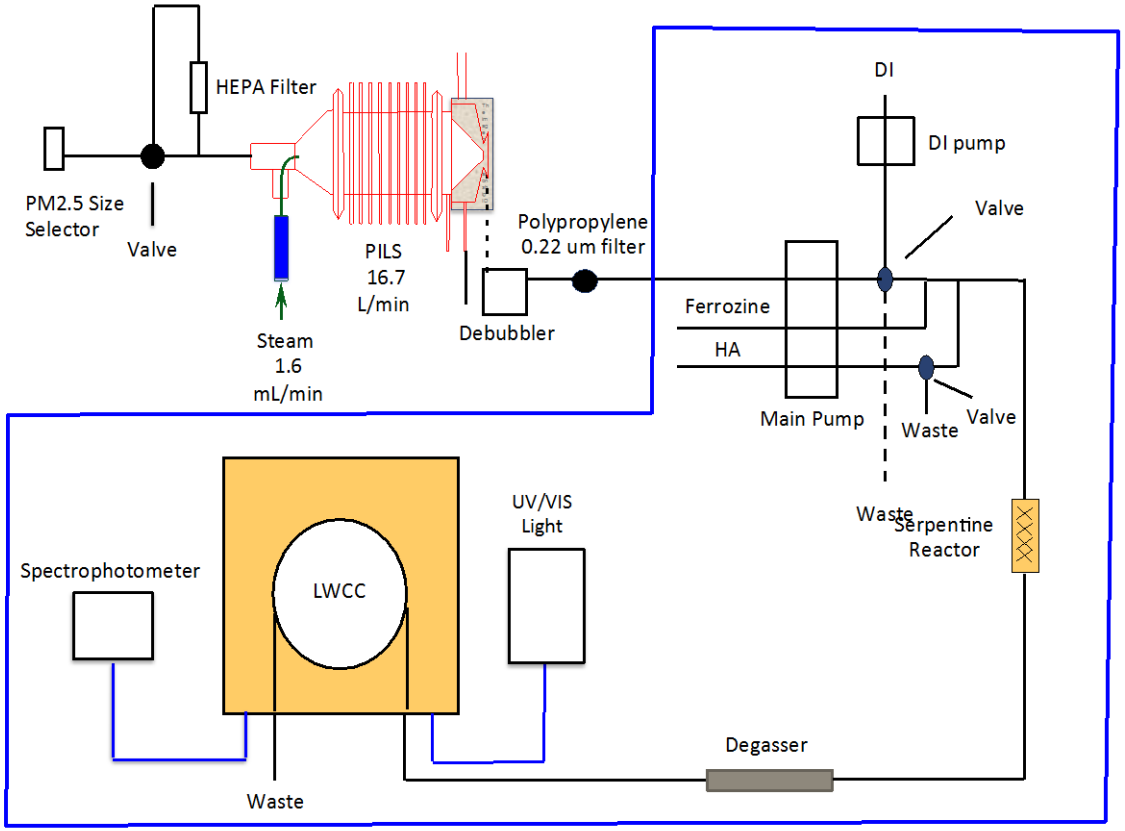

Figure A.1 Schematic of the CF-PILS-LWCC system. The liquid handling system is outlined in blue

A.3. Results and Discussion

A.3.1 Instrument Calibration

The liquid handling system of the CF-PILS-LWCC was calibrated in the same fashion as the original PILS-LWCC discussed in Chapter 2. Briefly, WS_Fe(II) and WS_Fe iron standards were pumped through the liquid handling system for instrument calibration. WS_Fe(II) and WS_Fe standards ranging from 0 to 20 ug L^{-1} were used for calibration to reflect the typical concentrations of soluble iron in atmospheric aerosols. Figure A.2 presents a typical calibration curve of the liquid handling system of the CF-PILS-LWCC. Regression results show strong linearity ($r^2 > 0.999$ for WS_Fe(II) and $r^2 > 0.99$ for WS_Fe) between light absorbance and iron standards. The difference between the calibration curve slopes of WS_Fe(II) (0.041) and WS_Fe (0.034) is a result of sample dilution by the HA reagent for WS_Fe measurements. Besides these small differences, the comparison between the two calibration curve show that HA addition does not cause measurement interferences.

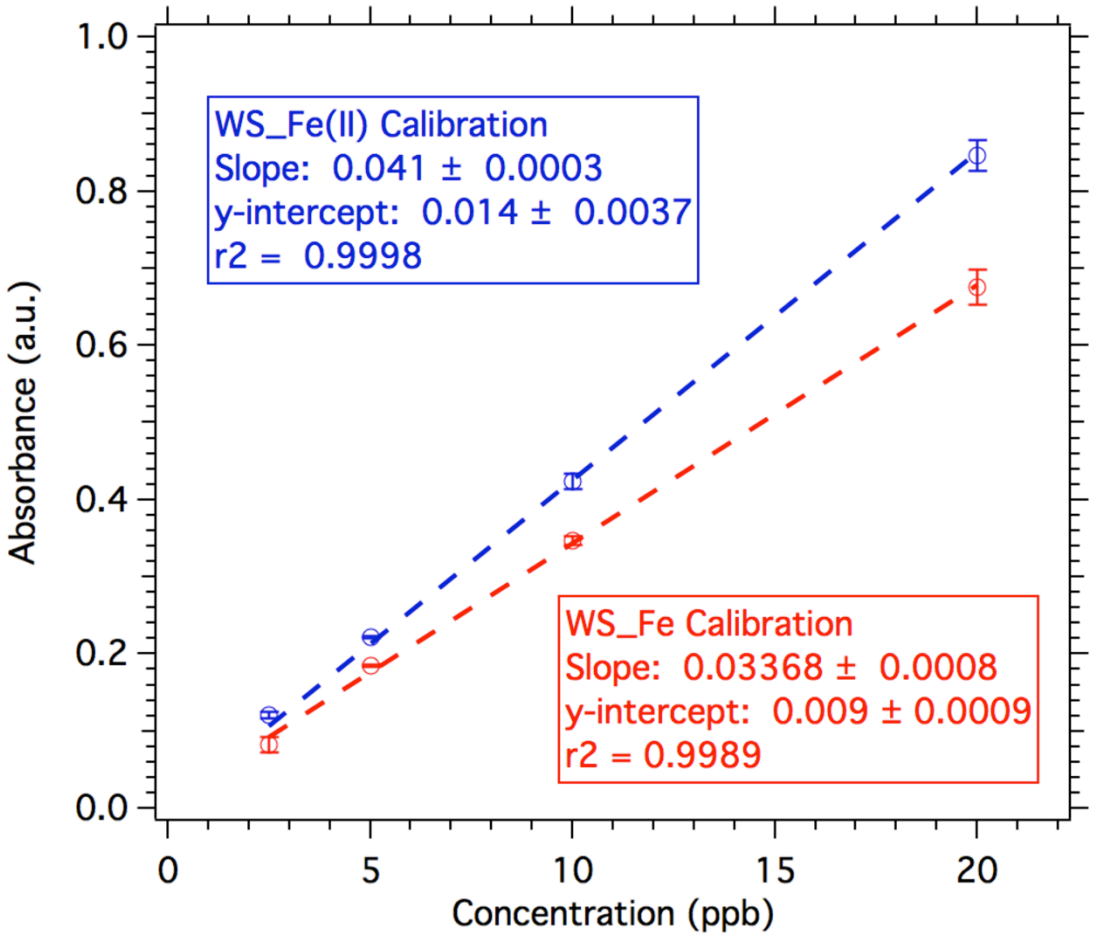

Figure A.2 Calibration curve of the CF-PILS-LWCC liquid handling for WS_Fe(II) (blue) and WS_Fe (red). Linear regression results are presented in the figure. Vertical bars represent the variability in absorbance for multiple standard analyses.

A.3.2 Field Maintenance and Dynamic Blanks

The CF-PILS-LWCC was deployed at the Fire Station 8 field site in metropolitan Atlanta from January to March 2010 to monitor the system performance as well as evaluate the method. Fire Station 8 is a mixed industrial/residential site located northwest of downtown Atlanta. Air quality at this site is heavily influenced by a nearby rail yard, fire station and a roadway with heavy diesel truck traffic. WS_Fe(II) and WS_Fe calibration curves were collected

before and after the field mission. After long periods of operation, the baseline increased due to light absorbing particles sticking to the LWCC. To maintain a stable baseline, the CF-PILS-LWCC liquid handling system was purged with 1 ml of methanol, 1 ml of 2N HCl and DI water every 2 to 4 days. After the cleaning cycle, the baseline was reset to 0.0 a.u.

Dynamic backgrounds were performed daily for 1.5 hours to account for any instrument measurement interferences from CF-PILS-LWCC operation, similar to the protocol used in the original PILS-LWCC. Ambient air was forced through a HEPA filter for 1.5 hours using an automated valve. The resulting aerosol-free sample was analyzed using the liquid handling system. A line was interpolated through the ambient concentration of consecutive dynamic backgrounds runs, and was subtracted from the WS_Fe(II) and WS_Fe measurement to yield ambient concentration. An example of the WS_Fe(II) air concentration of ambient aerosol and dynamic blanks measured during a multi-day period in March is shown in figure A.3 A. Though the background data (figure A.3 A: blank interpolation as a blue line, single blank as green ciricles) and is generally below the corresponding data, considerable blank variability is evident. Background data ranges from WS_Fe(II) air concentration of 0 to 38.95 ng m^{-3}, with an mean of 11.06 ± 8.92 ng m^{-3}. A continually increasing trend in background concentration is observed until the system is cleaned with the 2 N HCl and methanol, and returns to an ideal baseline WS_Fe(II) signal of 0.0 ug m^{-3}. While this background variability may seem to greatly compromise the data, subtracting the interpolated background from the WS_Fe(II) and WS_Fe measurements yields reasonable data (shown if Figure A.3 B).

However, the method limit of detection (26.75 ng m^{-3}, based on 3X standard deviation of blank variability) is greater than the majority of the data, indicating significant uncertainty associated with this data. These problems suggest a considerable carry-over effect within the system and indicate the need for a regular (hourly), automated cleaning cycle into the CF-PILS-LWCC field operation. For example, pumping 1 ml of 2N HCl followed by a thorough rinse of DI water would be an ideal cleaning cycle.

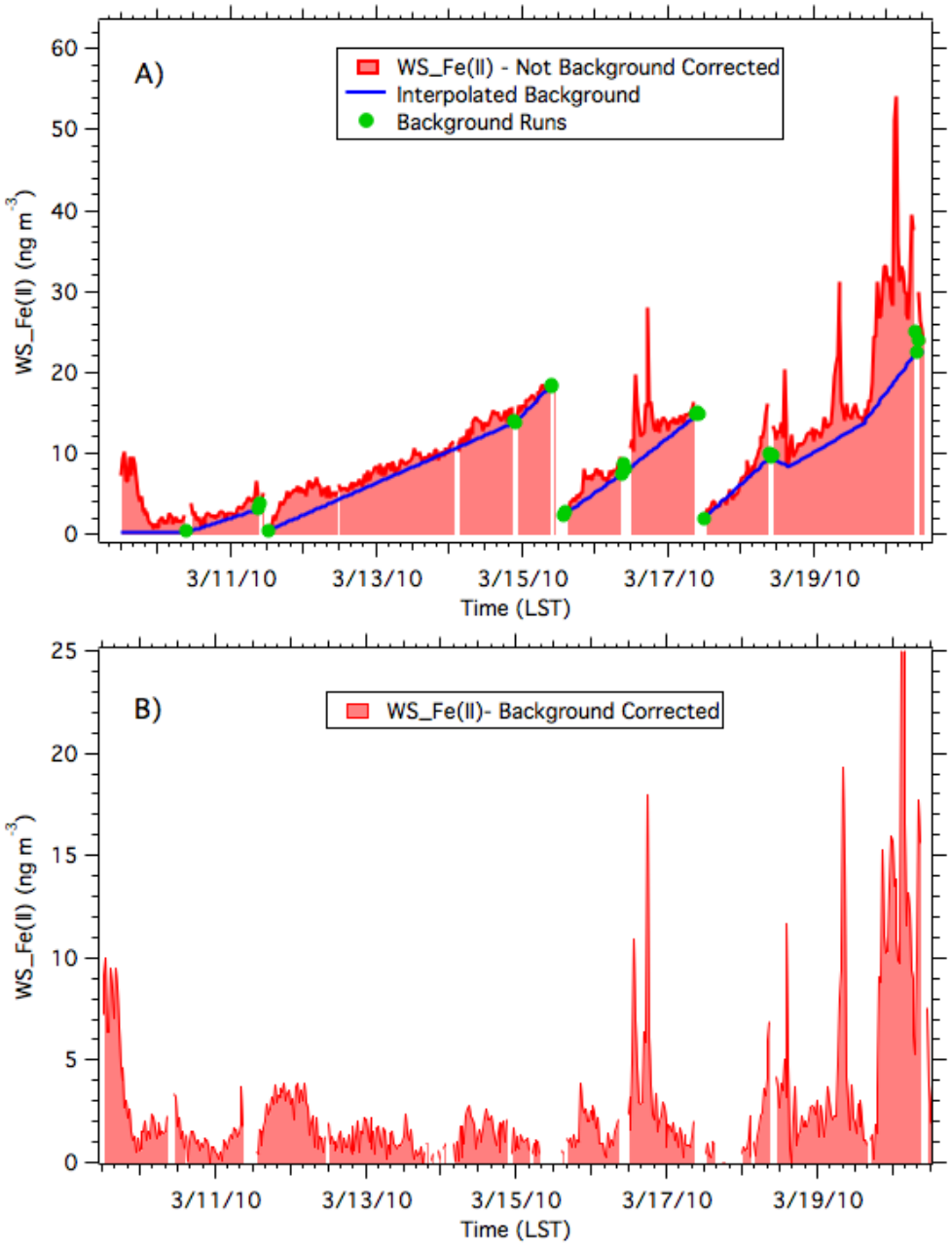

Figure A.3. Time series of WS_Fe(II) during a multi-day time sampling period in March 2010. A) WS_Fe(II) concentrations are plotted for ambient aerosols (red shading), individual dynamic backgrounds (green circle) and the linear interpolation through consecutive dynamic backgrounds (blue line). B) WS_Fe(II) background corrected data.

A.3.3 Field Deployment of the CF-PILS-LWCC: Temporal Variability

Figure A.4 A shows a time series of WS_Fe(II) and WS_Fe measured during field deployment at Fire Station 8 from January to March 2010. Significant temporal variability in WS_Fe(II) and WS_Fe are observed, with data ranging from the LOD to hundreds of ng m^{-3}. Since the LOD determined for CF-PILS-LWCC is high and unreliable, the original PILS-LWCC LOD (e.g. 4.6 ng m^{-3}) was used. The concentration range observed at Fire Station 8 during this sampling period is within the expected range (discussed in Chapter 3).

Figure A.4. B and C show multi-day periods of WS_Fe(II) and WS_Fe ambient concentrations. Transient events that were typically observed at Fire Station 8 using the original PILS-LWCC prototype (Chapter 3), were also observed during field deployment at Fire Station 8 in January 2010 (Figure A.4 B). Like the transient events observed in earlier field studies, these iron-rich events occurred during the evening hours (20:00 and 22:00), lasting for several hours. During these periods, WS_Fe(II) and WS_Fe concentration rapidly increased to 100s of ng m^{-3} in concentration then slowly decreased to background levels. Speciation of soluble iron data show these peaks are dominated by WS_Fe(II) rather than WS_Fe. Figure A.4 C shows another multi-day period during field deployment. Here, WS_Fe(II) and WS_Fe ambient concentrations are around background levels, yet are highly variable. During this periods, WS_Fe(III) concentrations are much greater than the WS_Fe(II) concentrations observed, indicating unique sources and/or atmospheric processes.

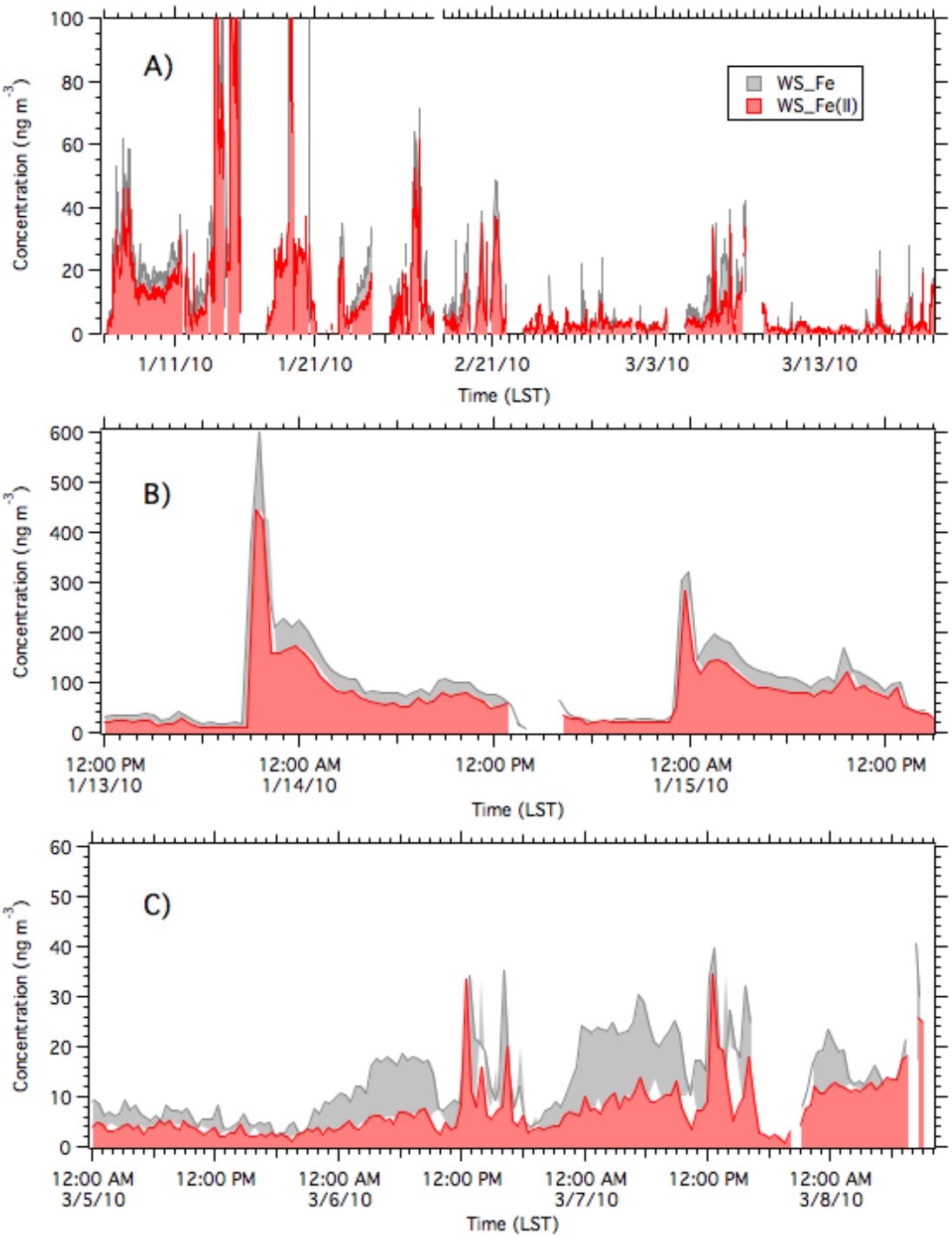

Figure A.4 Time series of WS_Fe(II) (red shading) and WS_Fe (gray shading) during field deployment in January through March 2010. Measurements in this figure represent A) the entire study, B) WS_Fe(II)/WS_Fe transient events observed in January 2010, and C) a multi-day period in March 2010.

A.3.4 CF-PILS-LWCC vs Filter Comparison

As previously discussed in chapter 2 (method development of the PILS-LWCC), particle collection, sample storage and analytical methods can result in positive or negative artifacts. To investigate these interferences, WS_Fe(II) and WS_Fe measurements from online (CF-PILS-LWCC) and offline (filter-based) techniques were compared. For this investigation, ambient PM2.5 was collected onto Teflon filters for 24-hours during CF-PILS-LWCC operation, allowing for direct comparison of WS_Fe(II) and WS_Fe measurements from both techniques. In this analysis, PILS measurements were averaged over the filter integration time for a point of comparison. Filters were cut in half to do two separate analyses. One portion of these filters were immediately extracted and analyzed using the CF-PILS-LWCC liquid handling system. Since these filter portions were immediately analyzed and analytically using similar methods (e.g. automated mixing), measurement artifacts can only arise from differences in particle collection (filter vs. PILS), not sample storage and analytical techniques. The second portion of these filters was immediately stored in a dark freezer (-20°C) for up to 2 months after collection, then manually extracted and analyzed in the laboratory. Laboratory analysis is similar to the protocol discussed in Chapter 2, Section 2.6. In this particular comparison, artifacts can arise from particle collection, sample storage, analytical techniques (manual vs. automated). Combining these comparisons provides insight on artifacts from particle collection (PILS vs. filter-based collection), sample storage (immediate analysis vs. analysis after arbitrary storage period), and analytical mixing (automated vs. manual mixing).

Deming regressions for all comparisons between CF-PILS-LWCC to filter-based WS_Fe(II) and WS_Fe measurements are shown in figure A.5. Filter measurements of WS_Fe(II) and WS_Fe analyzed using the CF-PILS-LWCC liquid handling system are shown in figure A.5 A and B. Here, relatively good agreement is observed between the PILS and filter measurements (WS_Fe(II): slope = 0.88 ± 0.13, y-intercept = 0.91 ±0.13, r2 = 0.74/ WS_Fe: slope = 0.75 ± 0.20, y-intercept = 0.46 ± 1.99, r2=0.56); however, the regression slopes indicate that filter-based measurements are consistently higher than PILS measurements (e.g. ~12% for WS_Fe(II) and ~25% for WS_Fe). Since filter samples were immediately analyzed and mixed using the CF-PILS-LWCC analytical system, these observed differences are likely due to particle collection. As discussed in Chapter 2, sampling artifacts can stem from particle collection/extraction using the PILS or filter-based techniques. In the PILS, particles are exposed to steam (100°C) for a short period of time (less than 1-second), before rapid cooling occurs. The exposure to heat during particle collection can drive oxidation of WS_Fe(II) to WS_Fe(III). While loss of WS_Fe(II) by heating in the PILS can explain low WS_Fe(II) concentrations relative to filter-based measurements, it does not explain the relatively low WS_Fe PILS concentration. In particular, the net WS_Fe (WS_Fe(II) + WS_Fe(III)) content should not change as a result of WS_Fe(II) oxidation. Loss in net WS_Fe can be explained by the precipitation of WS_Fe(III) out of solution upon formation of WS_Fe(III). In addition, conversion of WS_Fe(II) to WS_Fe(III), vice versa, can occur during filter extraction into de-ionized water or bulk condensation of water onto the particle in the PILS. These processes may alter original aerosol acidity, resulting in an aqueous

extract at circumneutral pH. In this pH range, oxidation of WS_Fe(II) is more likely to occur than reduction of WS_Fe(III). Overall, the good comparison between the PILS and these filter-based measurements (analyzed using the CF-PILS-LWCC liquid handling system) indicate PILS collection efficiency of WS_Fe(II) and WS_Fe (WS_Fe(II) + WS_Fe(III)) is within 12-25% of traditional techniques used to measure these trace atmospheric components (e.g. filter-based measurements).

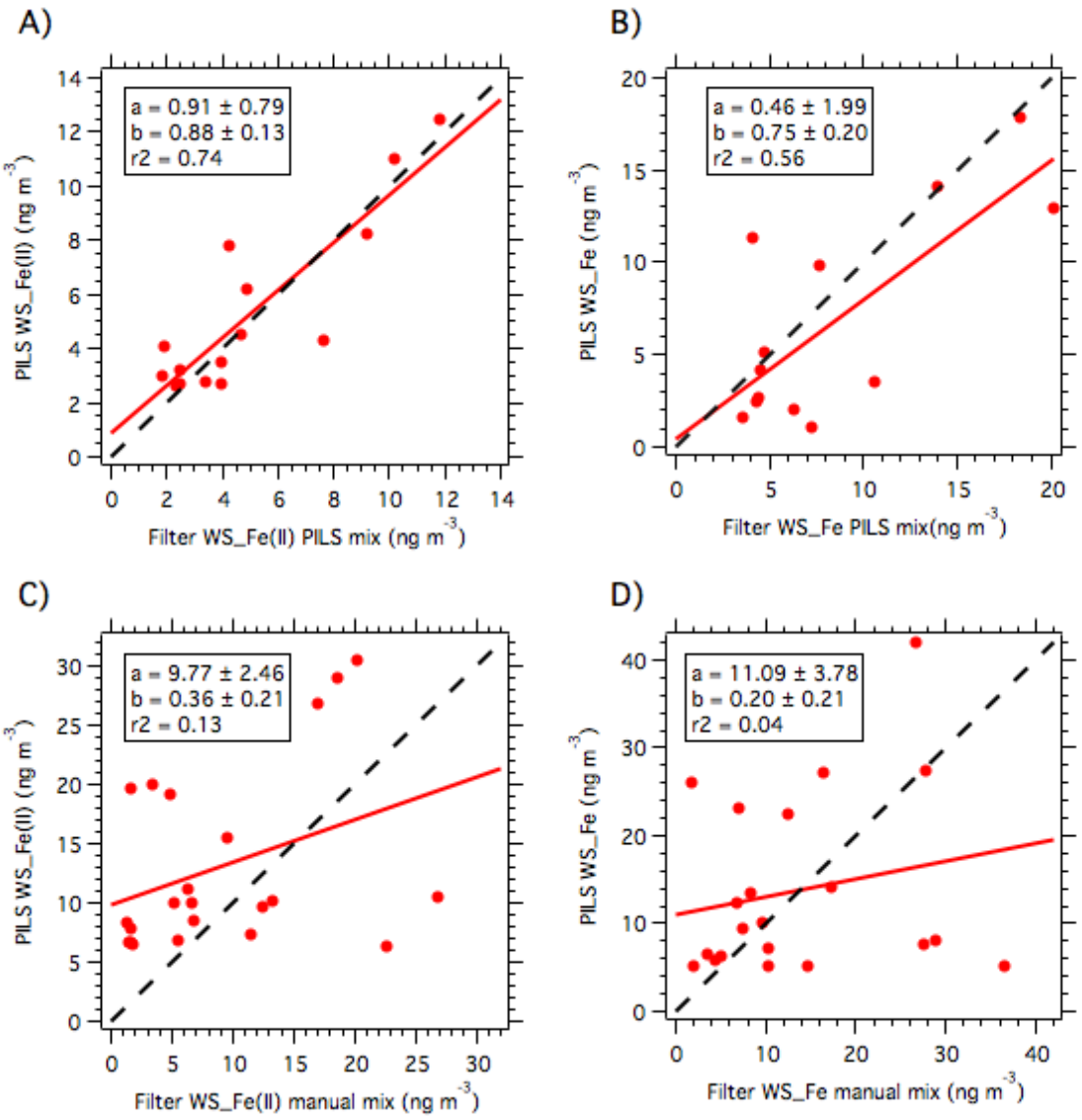

Figure A.5 Comparison between CF-PILS-LWCC and filter-based WS_Fe(II) and WS_Fe measurements. The y-intercept (a), slope (b), and r2 values from Deming regression analysis are presented in each graph. The Deming regressions (solid red line) and 1:1 ratio line (black dashed line) are presented in each graph. CF-PILS-LWCC WS_Fe(II) measurements are compared to filter measurements analyzed using A) the CF-PILS-LWCC liquid handling system and C) manual offline analysis in the laboratory. CF-PILS-LWCC WS_Fe is compared with filter measurements analyzed using B) the CF-PILS-LWCC liquid handling system and D) manual offline analysis in the laboratory.

Figure A.5 c and D show a similar comparison between offline and online techniques, except the filters represented here were stored for up to 2 months after collection, then extracted and analyzed manually in the laboratory. This comparison was used to provide insight on sampling artifacts from analytical methods (e.g.CF-PILS-LWCC or manually mixing) and sample storage. Poor correlation between CF-PILS-LWCC and manually mixed filter-based WS_Fe(II) and WS_Fe measurements was observed, showing significant scatter in the dataset (WS_Fe(II): slope = 0.36±0.12, y-intercept = 9.77 ± 2.46, r2 =0.13/ WS_Fe: slope = 0.20±0.21, y-intercept = 11.09 ± 3.78, r2 =0.04). Although sampling artifacts from different particle collection methods (PILS vs. filter) likely contribute to the scatter, PILS collection efficiency appeared to have minimal effect (e.g. 12-25% lower than filter-based measurements) on sample scatter based on the comparison in figure A.5. A and B. Thus, the scatter in is likely dominated by differences in analytical methods (e.g. mixing) in the PILS and filter-based measurements or filter sample storage. For instance, ferrozine can interact with and reduce WS_Fe(III). This mechanism can cause an increase in both filter and PILS WS_Fe(II). To minimize this effect between offline and online measurements, a uniform 12-minute delay between ferrozine addition and sample analysis was applied to both filter and PILS samples. In addition, conversion of WS_Fe(II) to WS_Fe(III) during filter sample storage can result in a decrease of WS_Fe(II). Although WS_Fe(II) loss likely occurred during storage, significant loss is not expected within the specific storage conditions and time period used in this study (Majestic et. al., 2006). It is also possible that the CF-PILS-LWCC analytical mixing causes variability in measurements. For instance,

reagent and sample liquid flow rates used in the CF-PILS-LWCC (controlled by the peristaltic pump) are near the lower limit of flow rates that can be accurately controlled by the peristaltic pump, thus, these flows may be highly uncertain. Small deviations in reagent and sample flow rates could result in significant uncertainties in soluble iron measurements. Several calibration curves (N=3) were performed periodically during field operation to account for such liquid flow rate deviations; however, this dataset is not large enough to infer robust conclusions on this hypothesis. Overall, the poor correlation indicates the challenges in comparing filter and PILS measurements using different analytical mixing techniques, and emphasizes that measurements of this type are clearly operationally-defined. The combined results of online and offline (e.g. manually mixed and CF-PILS-LWCC mixed) measurements indicate the importance of using similar analytical techniques (e.g. mixing kinetics) for method comparison.

A.4 Summary and Future Work

In conclusion, significant modifications were made to the original PILS-LWCC prototype, leading to a modified continuous flow prototype (CF-PILS-LWCC). The CF-PILS-LWCC is a fully-automated, field-deployable method that provides highly time-resolved measurements (1 measurement/30 minutes sampling) of WS_Fe(II) and WS_Fe(III) in aerosols. Significant improvements made to the original prototype have drastically improved measurement interferences caused by air bubbles, resulting in easier, automated operation of the instrument. The addition of WS_Fe measurements have also made it possible to investigate WS_Fe(III) in aerosols and provide key information on sources and processes of soluble iron.

Though there have been several modifications that have refined the performance of the CF-PILS-LWCC, additional work on method development and validation is recommended. For instance, increasing background signals observed during field deployment, indicate the need for a routine cleaning cycle. Integrating an hourly cleaning cycle (of methanol and 2N HCl) would help to decrease and stabilize dynamic background signals, likely improving the sensitivity of the measurement. Furthermore, continued filter analysis would provide more insight to the artifacts causing deviations between PILS and filter measurements. Overall, the CF-PILS-LWCC has been greatly improved automated operation from it's original prototype, but significant challenges remain in order to have a reliable system that can be deployed in the field for extended periods of time with minimal supervision.

APPENDIX B

STANDARD OPERATION PROCEDURE FOR THE CF-PILS-LWCC

This appendix presents the standard operating procedure (SOP) for maintenance and operation of the CF-PILS-LWCC for soluble iron measurements in ambient PM2.5. The following SOP is presented in an outline format.

B.1 Standard and Reagent preparation

1. Cleaning procedure
    a. Acid Clean bottles
        i. Soak in 2.5 N hydrochloric acid overnight
        ii. Rinse 3X with ultrapure Milli-Q water (>18MΩ)

2. 1000 ppm (mg L^{-1}) Fe(II) stock solution
    a. Weigh 0.702 g of ammonium iron(II) sulfate hexahydrate (Sigma-Aldrich, St. Louis, MO) using a Teflon-coated spatula
        i. Add up to 10g of ultra-pure water (>18MΩ) gravimetrically
        ii. Add 200 uL of 6N hydrochloric acid

3. 1 ppm (mg L^{-1}) Fe(II) stock solution
    a. Prepare in acid-cleaned (see above) 40 ml centrifuge tubes
    b. Add 40 ul of 1000ppm Fe(II) stock solution
    c. Dilute to 40 ml of de-ionized water

4. Working Fe(II) Standards (1-20 ug L^{-1})
    a. Prepare all standards in acid-cleaned (see above) 40 ml centrifuge tubes
    b. Dilute standards to the concentrations following the procedures

Table B.1 Serial Dilutions for Working Fe(II) Standards

Concentration (ug L^{-1})	1ppm Fe(II) (uL)	Ferrozine (uL)	2N HCl (uL)	DI (ml)
1	40	400	40	Fill to 40ml
2.5	100	400	40	Fill to 40ml
5	200	400	40	Fill to 40ml
10	400	400	40	Fill to 40ml
20	800	400	40	Fill to 40 ml

*Order of addition is from the left to right column.

5. 5 mM Ferrozine Reagent
    a. Add 0.255 g of ferrozine (3-(2-pyridyl)-5,6-diphenyl-1,2,4-triazine-4-4'-disufonic acid, Sigma-Aldrich, St. Louis, MO) using a Teflon-coated spatula to 20 ml amber polyethylene bottle
    b. Dilute to 100 ml of ultra-pure water

6. HA Solution
    a. Add 40 mg of Hydroxylamine hydrocloride to acid-cleaned amber bottle using a Teflon-coated spatula
    b. Add 50 mg of deionized water, measured gravimetrically

B.2 CF-PILS-LWCC Operation

1. Fundamentals of CF-PILS-LWCC Operation
    a. Use standard PILS operation set-up based on Orsini et. al. (2001)
    b. Liquid flows are controlled by a Cole-Parmer 8-channel peristaltic pump
    c. Color-coded Tygon tubing are use to control flow-rate (Table A.2.)
    d. Flows should be calibrated gravimetrically for 1-2 minute time intervals.
    e. Air flow is controlled by the vacuum pump (16.7 L min^{-1})

Table B.2 Liquid flows for peristaltic pump

Flow	*Tubing Color Code*	*Flow Rate (ml min^{-1})*
Impaction Plate In	Blue/Yellow	0.1
Impaction Plate Out	*Green/Yellow	0.11
Waste 1	Purple/Black	
Waste 2	Purple/Black	
Steam	Purple/Black	1.4-1.6
Debubbler	Green/Yellow	
Hydroxylamine HCl	Red/Orange	0.01
Ferrozine	Red/Orange	0.01

*May have to adjust

2. Liquid Handling Set-up
    a. Schematic of the set-up is seen in Figure A.1 in Appendix Chapter A.1
    b. Connect all working parts via PEEK or Teflon fittings.
    c. A 4-channel computer-controlled peristaltic pump should be used to control liquid flows. The computer program is shown in Figure A.2.1.
    d. To set up peristaltic pump and computer communication, connect the peristaltic pump to a LabJack that is connected to the laptop computer.

i. This is done by using a 10-pin connector wired to +5VDC, Remote, and GND positions in the ANALOG connection on the back of the peristaltic pump
ii. Wire these to the AO1 and GND positions on the lab jack.

e. Should be adjusted so that DI liquid flow is roughly 3 ml min^{-1}**.**

3. System Calibration

a. The CF-PILS-LWCC should always be calibrated before, during and field deployment.
i. Before and after field deployment, it should be fully calibrated using several standards
ii. During field deployment, a 1 or 2 point calibration curve should be performed twice/week to understand the system stability

b. Standards are pumped through the liquid handling system for system calibration

c. Start a water (blank) sample flow through the liquid handling system.

d. Connect the portable spectrophotometer via USB cable to laptop computer with Ocean Optics Spectra suite installed
i. Start Spectra Suite
ii. Select Absorbance Measurement
iii. Set Light and Dark Absorption Spectra
iv. Record data at 562 nm and 700 nm using the Strip Chart option in Spectra Suite

e. Allow blank sample to run for 1-2 hours before calibration to gain system stability.

f. Prepare working Fe(II) standards (1-20 ug L^{-1}) while waiting for system to stabilize.

g. Once stability is reached, switch water inflow to standard inflow and start running standards one at a time using the computer program listed in Figure 3.

h. Repeat each standard measurement 3X to ensure measurement accuracy/precision.

i. Prepare calibration curve for procedure (Absorbance vs. Concentration)

```
time 0
DI_valve = 0 //sample is inline
HA_valve = 0 // HA is offline going back to reservoir
pp_DI = 0 //Peristlatic pump for DI is off

time 660
pp_DI= 1.2 //Peristaltic pump for DI is on at speed 23

time 720
DI_valve = 1 // DI inline

time 770
pp_DI = 0//Peristaltic pump for DI is off

time 830
pp_DI = 1.2 //turn on DI
HA_valve = 1 //HA online

time 900
DI_valve = 0 // Switch to sample inline
pp_DI = 0 //Peristaltic pump for DI is off

time 1560
pp_DI = 1.2 //Peristaltic pump is on at speed 23

time 1620
DI_valve = 1 // DI inline

time 1680
pp_DI = 0 //Peristaltic pump for DI is turned off

time 1740
HA_valve = 0 //HA is offline going back to reservoir
pp_DI = 1.2 //Peristaltic pump for DI is on at speed 23

time 1800
goto 0
```

Figure B.1 Daq Factory computer program to run CF-PILS-LWCC

4. Field Operation
    a. Before field operation, cyclones should be cleaned by sonication and dried.
    b. New black silicone tubing should be used for field measurements.
    c. Liquid and air flow rates should be checked gravimetrically and by the air flow meter before sampling begins
        i. If flow rates deviate more than 10%, troubleshoot these issues
    d. Similar to calibration, run pure water sample through the system (e.g. system running with a HEPA filter inline) to establish a steady background for measurements.
        i. Set this background in Spectra Suite using the same procedure for calibration (e.g. set light and dark spectra, then record data using the Strip Chart)
    e. Start measurements
    f. Soluble iron liquid and air concentrations should be calculated using the following equations

$$\text{Liquid Concentration} = \frac{\text{Absorbance} \pm \text{y-intercept}}{\text{Slope}}$$

$$\text{Air Concentration} = \frac{\text{Liquid Concentration} * \text{Liquid Flow Rate} * 1000}{\text{Air Flow Rate}}$$

5. Daily Blanks
    a. Dynamic blanks are run for 1.5 hours per day to account for artifacts stemming from the system operation. Ambient air is pushed through a HEPA filter to remove particles.
    b. Valve with HEPA filter is placed upstream of the PILS
    c. Connect the valve to a timer with blank times programmed in
        i. The timer should be tested before field operation
    d. A line should be interpolated through the data and subtracted from field data to obtain blank-corrected sample.

6. Field Maintenance
    a. Clean the LWCC and sample lines every other day by pumping 3 ml of 2N HCl followed by a rigorous rinse with ultra-pure de-ionized water (18MΩ) until the baseline returns to 0.
    b. Reset baseline using the same procedure for calibration.

APPENDIX C

STANDARD OPERATING PROCEDURE FOR FILTER

MEASUREMENTS AND ANALYSIS

This appendix presents the standard operating procedure (SOP) for filter measurements and analysis of water-soluble iron in ambient PM2.5. The following SOP is presented in an outline format.

C.1 Sample Preparation

1. Cleaning Procedures
    - a. Acid-clean the Teflon filter sampler
        - i. Soak in 2.5 N hydrochloric acid overnight
        - ii. Rinse 3X with ultrapure Milli-Q water (>18MΩ) (e.g place sampler in beaker filled with water, then sonicate for 10 minutes 3X)
        - iii. Dry filter sampler under HEPA-filtered hood
    - b. Clean 30 ml, wide-mouth amber bottles and 15 ml centrifuge tubes
        - i. Acid-clean the Teflon filter sampler
            1. Soak in 2.5 N hydrochloric acid overnight
            2. Rinse 3X with ultrapure Milli-Q water (>18MΩ)
        - ii. Dry bottles under HEPA-filtered hood
2. Equipment Preparation
    - a. Fit vacuum pump with a critical orifice that is calibrated for 16.7 L min^{-1}
    - b. Standard preparation (follow procedures outlined in Appendix II).

C.2 Filter Sampling and Storage

1. Filter Sampler Set-up and Operation
    - a. Connect top of the filter sampler to clean black silicone tubing that is connected to a cyclone
    - b. Connect bottom of the filter sampler to vaccuum pump using clear Tygon tubing
    - c. Load 47-mm, 1um pore size Zeflour or Teflon filter into filter sampler using clean Teflon-coated tweezers
    - d. Start vacuum pump
    - e. Measure flow rate (needs to be within 10% of desired flow rate)
    - f. Run sample for 24 hours (use a timer with the vacuum pump if integration time will go far over 24 hours)
    - g. After sample collection, remove filter from sampler and store in an acid-cleaned 30-ml amber bottle

2. Filter Storage
    a. To avoid any artifacts caused by sample storage, store in the freezer (-20°C) immediately after collection in a sealed polyethelene bag
    b. Solubility measurements should be taken within a month.

C.3 Filter Analysis

1. Instrument Set-up
    a. Couple the portable spectrophotometer to LWCC and laptop computer
    b. Connect Teflon tubing connected to a 3-10ml syringe to the "Sample Outflow" using PEEK fittings
    c. Connect Teflon tubing to the "Sample Inflow" using PEEK fittings

2. Instrument Calibration
    a. Preparation of Standards (see Appendix II, Standard and Reagent Preparation)
    b. Manually pull all the standards through the LWCC and record the data via Strip Chart in Spectra Suite (see Appendix II, Section 4 System Calibration)
    c. Create a calibration curve

3. Filter extraction
    a. Add 15-20 ml of de-ionized water (>18MΩ) to the filter samples
    b. Seal bottles with parafilm.
    c. Sonicate sealed samples for 30 minutes, with heat setting off
    d. After 30 minutes of sonication, let samples cool for 5 to 10 minutes
    e. Transfer the 4 ml extract of the filter to 15 ml acid-cleaned centrifuge tubes using a syringe equipped with a 0.45 um liquid filter
    f. Analyze by adding 40 uL of ferrozine solution and analyze 12minutes after ferrozine addition. This results in a 12-minute operationally-defined measurement.
    g. Following ferrozine addition, add 40 uL of HA solution and measure 12-minutes after HA addition. This results in a 12-minute operationally-defined measurement.

REFERENCES

Andreae, M. O. (1983), Soot carbon and excess fine potassium: Long-range transport of combustion-derived aerosols, *Science*, *220*, 1148-1151.

Auffan, M., W. Achouak, J. Rose, M. Roncato, C. Chaneac, D. T. Waite, A. Masion, J. C. Woicik, M. R. Wiesner, and J. Bottero (2008), Relation between redox state of iron-based nanoparticles and their cytotoxicity toward Escherichia coli, *Environ. Sci. Technol.*, *42*(2), 6730-6735.

Ayres, J. G., P. Borm, F. R. Cassee, V. Castranova, K. Donaldson, A. Ghio, R. M. Harrison, R. Hider, F. Kelly, and I. M. Kooter (2008), Evaluating the toxicity of airborne particulate matter and nanoparticles by measuring oxidative stress potential: A workshop report and consensus statement, *Inhalation Toxiciology*, *20*, 75-99.

Bajt, S., Sutton, S. R., Delaney, J. S. (1994), X-ray microprobe analysis of iron oxidation states in silicates and oxides using X-ray absorption near edge structure (XANES), *Geochemica et Cosmochimica Acta*, *58*(23), 5209-5214.

Baker, A. R., and T. D. Jickells (2006), Mineral particle size as a control on aerosol iron solubility, *Geophys. Res. Lett.*, *33*(L17608), doi: 10.1029/2006GL026557.

Baker, A. R., and P. L. Croot (2010), Atmospheric and marine controls on aerosol iron solubility in seawater, *Marine Chemistry*, *120*(1-4), 4-13.

Baker, A. R., T. D. Jickells, M. Witt, and K. L. Linge (2006), Trends in the solubility of iron, aluminium, manganese and phosphorus in aerosol collected over the Atlantic Ocean, *Marine Chemistry*, *98*, 43-58.

Birch, M. E. (1998), Analysis of carbaceous aerosols: interlaboratory comparison, *Analyst*, *123*, 851-857.

Breytenbach, L., W. Van Pareen, and J. J. Pienaar (1994), The influence of organic acids and metal ions on the kinetics of the oxidation of sulfur(IV) by hydrogen peroxide, *Atmos. Environ.*, *28*(15), 2451-2459.

Butler, A. J., M. S. Andrew, and A. G. Russell (2003), Daily sampling of PM2.5 in Atlanta: Results of the first year of the Assessment of Spatial Aerosol Composition in Atlanta study, *Journal of Geophysical Research-Atmopsheres*, *108*(D7), doi:10.1029/2002JD002234.

Change, I. P. o. C. (2007), Climate Change 2007: The Physical Science Basis. Contribution of Working Group I to the Fourth Assessment of the Intergovernmental Panel on Climate Change*Rep.*, Cambridge University Press, Cambridge, United Kingdom and New York, NY USA.

Charlson, R. J., S. E. Schwartz, J. M. Hales, R. D. Cess, A. J. Coakley, J. E. Hansen, and D. J. Hofmann (1992), Climate Forcing by Anthropogenic Aerosols, *Science*, *255*(5043), 423-430.

Chen, L.-W. A., H. Moosmller, W. P. Arnott, J. C. Chow, J. G. Watson, R. A. Susott, R. E. Babbitt, C. E. Wold, E. N. Lincoln, and W. M. Hao (2007), Emmisions from laboratory combustion of wildland fuels: emission factors and source profiles, *Environmental Science and Technology*, *41*(12), 4317-4325.

Chen, Y., and R. L. Siefert (2004), Seasonal and spatial distributions and dry deposition fluxes of atmospheric total and labile iron over the tropical and subtropical North Atlantic Ocean, *J. Geophys. Res.-Atmos.*, *109*(D9), 15.

Choel, M., K. Deboudt, and P. Flament (2010), Development of time-resolved description of aerosol properties at the particle scale during an episode of industrial pollution plume, *Water Air and Soil Pollution*, *209*(1-4), 93-107.

Choel, M., Deboudt, K., Flament, P., Almoz, L., Meriaux, X. (2007), Single-particle analysis of atmospheric aerososl at Cape Gris-Nez, English Channel: Influence of steel works on iron apportionment, *Atmos. Environ.*, *41*
(13), 2820-2830.

Chuang, P. Y., R. M. Duvall, M. M. Shafer, and J. J. Schauer (2005), The origin of water soluble particulate iron in the Asian atmospheric outflow, *Geophys. Res. Lett.*, *32*(7), 4.

Claquin, T., M. Schulz, and Y. J. Balkanski (1999), Modeling the mineralogy of atmospheric dust sources, *J. Geophys. Res.-Atmos.*, *104*(D18), 22243-22256.

Costa, D. L., and K. L. Dreher (1997), Bioavailable Transition Metals in Particulate Matter Mediate Cardiopulmonary Injury in Healthy and Compromised Animal Models, *Environmental Health Persepectives*, *105*, 1053-1060.

Cwiertny, D. M., J. Baltrusaitis, G. J. Hunter, A. Laskin, M. M. Scherer, and V. H. Grassian (2008), Characterization and acid-mobilization study of iron-containing mineral dust source materials, *J. Geophys. Res.-Atmos.*, *113*(D5), 18.

Deer, W. A., R. A. Howie, and J. Zussman (1978), *An Introduction to the Rock Forming Minerals*, 528 pp., Longman Group Limited, London, U.K.

Dockery, D. W., C. A. I. Pope, X. Xu, J. D. Spengler, J. H. Ware, M. E. Fay, B. G. J. Ferris, and F. E. Speizer (1993), An association between air pollution and mortality in six U.S. citites, *The New England Journal of Medicine*, *329*(24), 1753-1759.

Dreher, K. L., R. H. Jaskot, J. R. Lehmann, J. H. Richards, J. K. McGee, A. J. Ghio, and D. L. Costa (1997), Soluble transition metals mediate residual oil fly ash acute lung injury, *Journal of Toxicology and Environmental Health*, *50*(3), 285-303.

Duce, R. A., and N. W. Tindale (1991), Atmospheric transport of iron and its deposition in the ocean, *Limnol. Oceanogr.*, *36*(8), 1715-1726.

Environment, P. o. t. (2001), CFR, Parts 80 and 86, Title 40, edited.

Erel, Y., S. O. Pehkonen, and M. R. Hoffmann (1993), Redox chemistry of iron in fog and stratus clouds, *J. Geophys. Res.-Atmos.*, *98*(D10), 18423-18434.

Faust, B. C., and R. G. Zepp (1993), Photochemistry of aqueous iron(III) polycarboxylate complexes - roles in the chemistry of atmospheric and surface waters, *Environ. Sci. Technol.*, *27*(12), 2517-2522.

Fountoukis, C., and A. Nenes (2007), ISORROPIA II: A computationally efficient thermodynamic equilibrium model for K+, Ca 2+, Mg2+, NH4+, Na+ So42-, NO3-, Cl-, H2O aerosols, *Atmos. Chem. Phys.*, *7*(17), 4639-3659.

Gao, Y., F. S., and J. L. Sarmento (2003), Aeolian iron input to the ocean through precipitation scavenging: A modeling perspective and its implication for natural iron fertilization in the ocean, *Journal of Geophysical Research-Atmopsheres*, *108*(D7), 13.

Guieu, C., S. Bonnet, T. Wagener, and M. D. Loye-Pilot (2005), Biomass burning as a source of dissolved iron to the open ocean?, *Geophys. Res. Lett.*, *32*(19), 5.

Hammond, D. M., J. T. Dvonch, G. J. Keeler, E. A. Parker, A. S. Kamal, J. A. Barres, F. Y. Yip, and W. Brakefield-Caldwell (2008), Sources of ambient fine particulate matter at two community sites in Detroit, Michigan, *Atmos. Environ.*, *42*(4), 720-732.

Hand, J. L., N. M. Mahowald, Y. Chen, R. L. Siefert, C. Luo, A. Subramaniam, and I. Fung (2004), Estimates of atmospheric-processed soluble iron from observations and a global mineral aerosol model: Biogeochemical implications, *J. Geophys. Res.-Atmos.*, *109*(D17), doi:10.1029/2004JD004574.

Hansen, D. A., E. S. Edgerton, B. Hartsell, and J. Jansen (2006), Air quality measurements for the aerosol research and inhalation epidemiology study, *Journal of the Air and Waste Management Association*, *56*(10), 1445-1458.

Hoffmann, P., A. N. Dedik, J. Ensling, S. Weinbruch, S. Weber, T. Sinner, P. Gutlich, and H. M. Ortner (1996), Speciation of iron in atmospheric aerosol samples, *Journal of Aerosol Science*, *27*(2), 325-327.

Hong, H., and D. R. Kester (1986), Redox state of Fe in the offshore waters if Peru, *Limnol. Oceanogr.*, *31*, 512-524.

Ingall, E. D., Brandes, J. A., Diaz, J. M., de Jonge, M. D., Paterson, D., McNulty, I., Elliot, W. C., Northrup, P. (2011), Phosphorus K-edge XANES spectroscopy of mineral standards, *Journal of Synchrotron Radiation*, *18*(18), doi:10.1107/S0909049510045322.

Jickells, T. D., et al. (2005), Global iron connections between desert dust, ocean biogeochemistry, and climate, *Science*, *308*(5718), 67-71.

Johansen, A. M., R. Siefert, and M. R. Hoffmann (2000), Chemical composition of aerosols collected over the tropical North Atlantic Ocean, *J. Geophys. Res.-Atmos.*, *105*(D12), 15277-15312.

Journet, E., K. V. Desboeufs, S. Caquineau, and J. L. Colin (2008), Mineralogy as a critical factor of dust iron solubility, *Geophys. Res. Lett.*, *35*(7), doi:10.1029/2007GL031589.

Keenan, C. R., R. Goth-Goldstein, D. Lucas, and D. L. Sedlak (2009), Oxidative stress induced by zero-valent iron nanoparticles and Fe(II) in human bronchial epithelial cells, *Environ. Sci. Technol.*, *43*(12), 4555-4560.

Kelly, F. J. (2003), Oxidative stress: Its role in air pollution and adverse health effects, *Occup. Environ. Med.*, *60*(8), 612-616.

Kidwell, C. B., and J. M. Ondov (2004), Elemental analysis of sub-hourly ambient aerosol collections, *Aerosol Science and Technology*, *38*(3), 205-218.

Kumar, P., I. N. Sokolik, and A. Nenes (2011), Measurements of cloud condensation nuclei activity and droplet activation kinetics of fresh unprocessed regional dust samples and minerals, *Atmos. Chem. Phys.*, *11*, 3527-3541.

Lam, P. J., and J. K. Bishop (2008), The continental margin is a key source of iron to the HNLC North Pacific Ocean, *Geophys. Res. Lett.*, *35*, 5.

Lee, S., K. Baumann, J. J. Schauer, R. J. Sheesley, L. P. Naeher, S. Meinardi, D. R. Blake, E. S. Edgerton, A. G. Russell, and M. Clements (2005), Gaseous and particulate emissions from prescribed burning in Georgia, *Environ. Sci. Technol.*, *39*(23), 9049-9056.

Liu, W., Y. H. Wang, A. Russell, and E. S. Edgerton (2005), Atmospheric aerosol over two urban-rural pairs in the southeastern United States: Chemical composition and possible sources, *Atmos. Environ.*, *39*(25), 4453-4470.

Liu, Z. G., D. R. Berg, and J. J. Schauer (2008), Effects of a Zeolite-Selective Catalytic Reduction System on Comprehensive Emissions from a Heavy-Duty Diesel Engine, *J. Air & Waste Manag. Assoc.*, *58*, 1258-1265.

Luo, C., N. Mahowald, T. Bond, P. Y. Chuang, P. Artaxo, R. Siefert, Y. Chen, and J. Schauer (2008), Combustion iron distribution and deposition, *Glob. Biogeochem. Cycle*, *22*(1), 17.

Mackie, D. S., P. W. Boyd, K. A. Hunter, and G. H. McTanish (2005), Simulating the cloud processing of iron in Austrailian dust: pH and dust concentration, *Geophys. Res. Lett.*, *32*(L06809).

Mahowald, N., A. R. Baker, G. Bergametti, N. Brooks, R. A. Duce, T. D. Jickells, N. Kubilay, J. M. Prospero, and I. Tegen (2005), Atmospheric global dust cycle and iron inputs to the ocean, *Glob. Biogeochem. Cycle*, *19*(4), GB4025.

Majestic, B. J., J. J. Schauer, and M. M. Shafer (2007), Application of synchrotron radiation for measurement of iron red-ox speciation in atmospherically processed aerosols, *Atmos. Chem. Phys.*, *7*(10), 2475-2487.

Majestic, B. J., A. D. Anbar, and P. Herckes (2009), Elemental and iron isotopic composition of aerosols collected in a parking structure, *Science of the Total Environment*, *407*, 5104-5109.

Majestic, B. J., J. J. Schauer, M. M. Shafer, J. R. Turner, P. M. Fine, M. Singh, and C. Sioutas (2006), Development of a wet-chemical method for the speciation of iron in atmospheric aerosols, *Environ. Sci. Technol.*, *40*(7), 2346-2351.

Marcus, M. A., A. J. Westphal, and S. C. Fakra (2008), Classification of Fe-bearing species from K-edge XANES data using two parameter correlation plots, *Journal of Synchrotron Radiation*, *15*(Part 5), 463-468.

Martin, J. H., et al. (1994), Testing the iron hypothesis in ecosystems of the equatorial pacific-ocean, *Nature*, *371*(6493), 123-129.

Meskhidze, N., W. L. Chameides, A. Nenes, and G. Chen (2003), Iron mobilization in mineral dust: Can anthropogenic SO2 emissions affect ocean productivity?, *Geophys. Res. Lett.*, *30*(21), 5.

Murray, J. W., and G. Gill (1978), The geochemistry of iron in the Puget Sound, *Geochimica Cosmochimica Acta*, *42*, 9-19.

NIOSH (1996), Elemental carbon (diesel particulate): method 5040, in *NIOSH Manual of Analytical Methods,* , edited by P. M. Eller and M. W. Cassinelli, Cincinatti.

Ooki, A., J. Nishioka, T. Ono, and S. Noriki (2009), Size dependence of iron solubility of Asian mineral dust particles, *J. Geophys. Res.*, *114*(D03202).

Orsini, D. A., Y. L. Ma, A. Sullivan, B. Sierau, K. Baumann, and R. J. Weber (2003), Refinements to the particle-into-liquid sampler (PILS) for ground and airborne

measurements of water soluble aerosol composition, *Atmos. Environ.*, *37*(9-10), 1243-1259.

Parazols, M., A. Marinoni, P. Amato, O. Abida, P. Laj, and G. Mailhot (2006), Speciation and role of iron in cloud droplets at the puy de Dome station, *Journal of Atmospheric Chemistry*, *54*(3), 267-281.

Pehkonen, S. O., R. Siefert, Y. Erel, S. Webb, and M. R. Hoffmann (1993), Photoreduction of Iron Oxyhydroxides in the Presence of Important Atmospheric Organic Compounds, *Environ. Sci. Technol.*, *27*, 2056-2062.

Pope, C. A. I. (2000), Epidemiology of fine particulate air pollution and human health: Biologic Mechanisms and Who's at Risk?, *Environmental Health Persepectives*, *108*(Supplement 4), 713-723.

Pope, C. A. I., R. T. Burnett, M. J. Thun, E. E. Calle, D. Krewski, K. Ito, and G. D. Thurston (2002), Lung cancer, cardiopulmonary mortaility, and long-term exposure to fine particulate air pollution, *JAMA-Journal of The American Medical Association*, *287*(9), 1132-1141.

Prahalad, A. K., J. Inmon, L. A. Dailey, M. C. Madden, A. J. Ghio, and J. E. Gallagher (2001), Air pollution particles mediated oxidative DNA base damage in a cell free system and in human airway epithelial cells in relation to particulate metal content and bioreactivity, *Chemical Research in Toxicology*, *14*(7), 879-887.

Prietzel, J., J. Thieme, K. Eusterhues, and D. Eichert (2007), Iron speciation in soils and soil aggregates by synchrotron-based X-ray microspectroscopy (XANES, mu-XANES), *European Journal of Soil Science*, *58*(5), 1027-1041.

Reddy, M. S., S. B. Basha, H. V. Joshi, and B. Jha (2005), Evaluation of the emission characteristics of trace metals from coal and fuel oil fired power plants and their fate during combustion, *J. Hazard. Mater.*, *123*(1-3), 242-249.

Samet, J., F. Dominici, F. C. Curriero, I. Coursac, and S. L. Zeger (2000), Fine particulate air pollution and mortality in 20 U.S. cities, 1987-1994, *The New England Journal of Medicine*, *343*(24), 9.

Schauer, J. (2003), Evaluation of elemental carbon as a marker for diesel particulate matter, *Journal of Exposure Analysis and Environmental Epidemiology*, *13*, 443-453.

Schroth, A. W., J. Crusius, E. R. Sholkovitz, and B. C. Bostick (2009), Iron solubility driven by speciation in dust sources to the ocean, *Nature Geoscience*, *2*(5), 337-340.

Sedlak, D. L., J. Hoigne, M. M. David, R. N. Colvile, E. Seyffer, K. Acker, W. Wiepercht, J. A. Lind, and S. Fuzzi (1997), The cloudwater chemistry of iron and copper at Great Dun Fell, UK, *Atmos. Environ.*, *31*(16), 2515-2526.

Sedwick, P. N., E. R. Sholkovitz, and T. M. Church (2007), Impact of anthropogenic combustion emission on the fractional solubility of aerosol iron: Evidence from the Sargasso Sea, *Geochemistry Geophysics Geosystems*, *8*(10), 21.

See, S. W., Y. H. Wang, and R. Balasubramanian (2007), Contrasting reactive oxygen species and transition metal concentrations in combustion aerosols, *Environmental Research*, *103*(3), 317-324.

Shafer, M. M., D. A. Perkins, D. S. Antkiewicz, E. A. Stone, T. A. Quiraishi, and J. J. Schauer (2010), Reactive oxygen species acitivity and chemical speciation of size-fractionated atmospheric particlate matter from Lahore, Pakistan: an important role for transition metals, *Journal of Environmental Monitoring*, *12*(3), 704-415.

Shi, Z., M. D. Krom, and S. Bonneville (2009), Formation of iron nanoparticles and increase in iron reactivity in mineral dust during simulated cloud processing, *Environ. Sci. Technol.*, *43*(17), 6592-6596.

Shi, Z., S. Bonneville, M. D. Krom, K. S. Carslaw, T. D. Jickells, A. R. Baker, and L. G. Benning (2011), Iron dissolution kinetics of mineral dust at low pH during simulated atmospheric processing, *Atmos. Chem. Phys.*, *11*, 995-1007.

Shi, Z. B., et al. (2011), Minor effect of physical size sorting on iron solubility of transported mineral dust *Atmos. Chem. Phys.*, *11*, 8459-8469.

Sholkovitz, E. R., P. N. Sedwick, and T. M. Church (2009), Influence of anthropogenic combustion emission on the deposition of soluble aerosol iron to the ocean: Empirical estimates for island sites in the North Atlantic, *Geochemica et Cosmochimica Acta*, *73*, 3981-4003.

Siefert, R. L., A. M. Johansen, and M. R. Hoffmann (1999), Chemical characterization of ambient aerosol collected during the southwest monsoon and intermonsoon

seasons over the Arabian Sea: Labile-Fe(II) and other trace metals, *J. Geophys. Res.-Atmos.*, *104*(D3), 3511-3526.

Siefert, R. L., S. O. Pehkonen, Y. Erel, and M. R. Hoffmann (1994), Iron photochemistry of aqueous suspensions of ambient aerosol with added organic acids Pergamon-Elsevier Science Ltd.

Smith, K. R., and A. E. Aust (1997), Mobilization of Iron from Urban Particulates Leads to Generation of Reactive Oxygen Species in Vitro and Induction of Ferritin Synthesis in Human Lung Epithlial Cells, *Chemical Research in Toxicology*, *10*, 828-834.

Smith, R. D. (1980), The trace element chemistry of coal during combustion and the emissions from coal-fired plants, *Prog. Energy Combustion Science*, *6*, 53-119.

Solmon, F., P. Y. Chuang, N. Meskhidze, and Y. Chen (2009), Acidic processing of mineral dust iron by anthropogenic compounds over the north Pacific Ocean, *J. Geophys. Res.-Atmos.*, *114*.

Solomon, P. A., et al. (2003), Overview of the 1999 Atlanta Supersite Project, *Journal of Geophysical Research-Atmopsheres*, *108*(D7), 24.

Stookey, L. L. (1970), Ferrozine - a new spectrophotometric reagent for iron, *Anal. Chem.*, *42*(7), 779-&.

Streets, D. G., S. Gupta, T. Waldhoff, M. Q. Wang, T. C. Bond, and B. Yiyun (2001), Black carbon emissions in China, *Atmos. Environ.*, *35*, 4281-4296.

Stumm, W. and J. Morgan (1996), *Aquatic Chemistry,* John Wiley & Sons, New York, NY.

Sullivan, A. P., R. J. Weber, A. L. Clements, J. R. Turner, M. S. Bae, and J. J. Schauer (2004), A method for on-line measurement of water-soluble organic carbon in ambient aerosol particles: Results from an urban site., *Geophys. Res. Lett.*, *31*(L13105. Doi:10.1029/2004GL019681.

Takahama, S., S. Gilardoni, and L. M. Russell (2008), Single-particle oxidation state and morphology of atmospheric iron, *J. Geophys. Res.-Atmos.*, *113*(D22202), 16.

Takahashi, Y., M. Higashi, T. Furukawa, and S. Mitsunobu (2011), Change of iron species and iron solubility in Asian dust during the long-range transport from western China to Japan, *Atmospheric Chemistry and Physics Discussion*, *11*, 19545-19580.

Tao, F., B. Gonzalez-Flecha, and L. Kobzik (2003), Reactive oxygen species in pulmonary inflammation by ambient particulates, *Free Radic. Biol. Med.*, *35*(4), 327-340.

Valavanidas, A., K. Fiotakis, and T. Viachogianni (2008), Airborne Particulate Matter and Human Health: Toxicological Assessment and Importance of Size and Composition of Particle for Oxidative Damage and Carcinogenic Mechanisms, *Journal of Environmental Science and Health, Part C.*, *26*, 339-362.

Vidrio, E., H. Jung, and C. Anastasio (2008), Generation of hydroxyl radicals from dissolved transition metals in surrogate lung fluid solutions, *Atmos. Environ.*, *42*(18), 4369-4379.

Weber, R. J., and e. al. (2003), Short-term Temporal Variation in PM2.5 Mass and Chemical Composition during the Atlanta Supersite Experiment, 1999, *Journal of Air and Waste Management Association*, *53*, 84-91.

Wells, M. L., N. M. Price, and K. W. Bruland (1995), Iron chemistry in seawater and its relationship to phytoplankton: a workshop report, *Marine Chemistry*, *48*, 157-182.

Werner, M. L., Nico, P. S., Marcus, M. A. Anastasio, C. (2007), Use of micro-XANES to speciate chromium in airborne fine particles in the Sacramento Valley, *Environ. Sci. Technol.*, *41*(14), 4919-4924.

Wilke, M., F. Farges, P. Petit, G. E. Brown Jr, and F. Martin (2001), Oxidation state and coordination of Fe in minerals: An Fe K-XANES spectroscopic study, *American Mineralogist*, *86*, 714-730.

Willey, J. D., R. F. Whitehead, R. J. Kieber, and D. R. Hardison (2005), Oxidation of Fe(II) in rainwater, *Environ. Sci. Technol.*, *39*(8), 2579-2585.

Willey, J. D., R. J. Kieber, K. H. Williams, J. S. Crozier, S. A. Skrabal, and G. B. Avery (2000), Temporal variability of iron speciation in coastal rainwater, *Journal of Atmospheric Chemistry*, *37*(2), 185-205.

Yamasoe, M., P. Arataxo, A. Miguel, and A. Allen (2000), Chemical composition of aerosol particles from direct emissions of vegetation fires in the Amazon Basin: water-soluble species and trace elements, *Atmos. Environ.*, *34*, 13.

Zhang, J., C. Kelble, and F. J. Millero (2001), Gas-segmented continuous flow analysis of iron in water with a long liquid waveguide capillary flow cell, *Analytica Chimica Acta*, *438*, 49-57.

Zhang, Y. X., J. J. Schauer, M. M. Shafer, M. P. Hannigan, and S. J. Dutton (2008), Source apportionment of in vitro reactive oxygen species bioassay activity from atmospheric particulate matter, *Environ. Sci. Technol.*, *42*(19), 7502-7509.

Zhu, X., J. M. Prospero, D. L. Savoie, F. J. Millero, R. G. Zika, and E. S. Saltzman (1993), Photoreduction of iron(III) in marine mineral aerosol solutions, *J. Geophys. Res.-Atmos.*, *98*(D5), 9039-9046.

Zhuang, G., Z. Yi, R. A. Duce, and P. R. Brown (1992), Link between iron and sulphur cycles suggested by detection of Fe(II) in remote marine aerosols, *Nature*, *355*.